TECHNISCHE UNIVERSITÄT MÜNCHEN

PHYSIK DEPARTMENT E18

Tests of prototype magnets and study on a MCP based proton detector for the neutron lifetime experiment PENeLOPE

Dissertation

von

S. Materne

Technische Universität München

Physik Department E18

Tests of prototype magnets and study on a MCP based proton detector for the neutron lifetime experiment PENeLOPE

Stefan Materne

Vollständiger Abdruck der von der Fakultät für Physik der Technischen Universität München zur Erlangung des akademischen Grades eines

Doktors der Naturwissenschaften (Dr. rer. nat.)

genehmigten Dissertation.

Vorsitzende: Univ.-Prof. Dr. N. Brambilla

Prüfer der Dissertation:

1. Univ.-Prof. Dr. St. Paul
2. Univ.-Prof. Dr. L. Oberauer

Die Dissertation wurde am 10.04.2013 bei der Technischen Universität München eingereicht und durch die Fakultät für Physik am 25.06.2013 angenommen.

Abstract

The neutron, one of the basic building blocks of matter, is, when unbound, not stable and decays via weak interaction. Its lifetime τ_n is a fundamental observable, on the one hand giving insight into particle physic principles and on the other hand being an important parameter of models for nucleosynthesis in cosmology (chapter 1).
Lately, the measured value of the neutron lifetime has been under heavy discussion due to two contradicting experiments. Recent measurements and re-analysis of older ones slowly resolve the discrepancies; the official world average published by the Particle Data Group (PDG) is currently (880.1 ± 1.1) s.
Still, there is the need for more precise experiments using new experimental techniques to fully clarify the situation. One of these experiments is PENeLOPE, which aims to measure the neutron lifetime with a relative precision of 10^{-4} (chapter 3). The experiment is based on magnetic and gravitational confinement of ultra-cold neutrons, i.e. neutrons with kinetic energies $E_{kin} \leq 300\,\mathrm{neV}$ (chapter 2). Besides the traditional method of counting the surviving neutrons after a defined storage time, the time-resolved detection of the particles emerging from neutron decay will be used to extract the neutron lifetime. Thus, key parts of the instrument are the technically challenging superconducting magnet and the detector for the decay particles.
In the design phase of the magnet, prototype testing is mandatory for a successful realization of the highly complex and non-standard system. Parameters such as maximum current, ramping speed and stability at nominal current have to be confirmed. To this end, a complete test facility including a liquid-helium cryostat was set up (sections 4.2 and 6.2). This is supported by studies on safety aspects (section 4.2.1) and cryogenic design (section 6.2.2). Two prototypes of different companies were trained and their operational limits explored. The tests gave important input for the magnet concept: They revealed the failure of the first prototype at 70% of its nominal current (section 4.4) due to a faulty design of its housing. The design approach from another company was proved to work succesfully with the second prototype magnet (section 6.3.2). In the course of the tests, the performance of peripheral components like cryogenic protection diodes (section 6.3.2) and quench heaters (section 6.3.6) was checked.
Moreover, in the experiment PENeLOPE, magnetic field measurements are needed to make sure that the field map of the setup agrees with the planned field configuration. With the prototype test setup, a field mapping device was commissioned (section 5.1). It features a single mechanical vacuum feed-through to transfer the movement of a linear translation stage for all three directions at once from outside the cryostat over a long level arm into its center. The mechanical precision and reproducibility of the setup was extensively examined (section 5.2): Tiny tolerances in the actuator get multiplied by the long lever arm, so that the precision of the field sensor position is limited to a few mm. Algorithms for the analysis of the measured data were developed, especially to reconstruct the magnetic field from projections measured by hall sensors in a skew coordinate system (section 5.4). Exemplary, the position of the first prototype in the cryostat has been extracted with a precision of $< 0.5\,\mathrm{mm}$ by localizing the field minimum in its center (section 5.5.3). To this end, different minimum-finding algorithms were benchmarked. From the experience gathered in the measurements, conceptual and mechanical improvements follow for the design of the mapper in PENeLOPE.
The choice of the decay particle detector is especially delicate, as it has to operate in the harsh environment of the liquid-helium cryostat and to meet the requirements for a precise lifetime measurement (chapter 7). This comprises especially single proton detection, low noise and high time stability. Different detection principles have been contemplated; feasibility has to be proven, and the concept with the best performance has to be found. In this thesis, studies on the realization of a detector based on microchannel plates (MCPs) have been performed. The characteristics of a detector with a self-developed housing (section 7.3.3) is compared to a purchased complete

detector. The studies concentrated on measurements with α particles and protons (sections 7.3.6 and 7.3.7). Protons in the energy range expected in the later experiment ($10 - 30\,\mathrm{keV}$) could be clearly measured, however only a poor signal-to-noise ratio was achieved: the spectra have a peak-to-valley ratio of at most 2.5, implying an amount of misidentified proton events of more than 12%. This and a bad coverage with active material ($\approx 50\%$) disfavors the use of MCPs as a detector in PENeLOPE.

Zusammenfassung

Das Neutron, Hauptbestandteil der Materie, ist im ungebundenen Zustand instabil und zerfällt durch die schwache Wechselwirkung. Seine Lebensdauer τ_n ist eine wichtige Observable, zum Beispiel für das Standardmodell der Teilchenphysik oder auch für Modelle zur Nukleosynthese in der Kosmologie (Kapitel 1). Der genaue Wert der Neutronenlebensdauer war in den letzten Jahren auf Grund zweier widersprüchlicher Experimente umstritten. Jüngste Messungen sowie die Neu-Analyse alter Experimente haben die Situation nur leicht entschärft. Der von der Particle Data Group ermittelte Wert für die Neutronenlebensdauer liegt derzeit bei $(880,1 \pm 1,1)$ s. Weitere präzise Messungen mit neuen, experimentellen Techniken sind nötig, um die Diskrepanz vollends aufzuklären. Eines dieser Experimente ist PENeLOPE, das die Lebensdauer mit einer relativen Genauigkeit von 10^{-4} vermessen soll (Kapitel 3). In dem Experiment werden ultra-kalte Neutronen - Neutronen mit kinetischen Energien $E_{kin} \leq 300$neV - in einer Falle mit magnetischen und gravitativen Kräften eingesperrt werden (Kapitel 2). Neben der traditionellen Methode die nach einer bestimmten Wartezeit noch verbleibenden Neutronen zu zählen, soll die Lebensdauer auch aus dem zeitaufgelösten Nachweis der Zerfallsprodukte des Neutrons, insbesondere des Protons, extrahiert werden. Schlüsselkomponenten des Instruments sind daher der technisch herausfordernde supraleitende Magnet, sowie der Detektor für die Zerfallsteilchen.
Vor dem Bau des Experiments sind Tests mit einem Prototypen in der Entwicklungsphase des komplexen Magneten unerlässlich. Getestet werden müssen vor allem der höchstmögliche Magnetstrom, ein stabiler Betrieb bei Nominalstrom, sowie die Geschwindigkeit, mit der der Magnet hochgefahren werden kann. Der Aufbau einer kompletten Testumgebung mit einem Flüssig-Helium-Kryostaten war dafür notwendig (Kapitel 4.2 und 6.2). Berechnungen zu Sicherheitsaspekten (Kapitel 4.2.1) sowie kryogenem Design wurden durchgeführt (Kapitel 6.2.2). Zwei Prototypen verschiedener Magnethersteller wurden eintrainiert und ihre Betriebsgrenzen ausgelotet. Aus den Tests haben sich wichtige Erkenntnisse für die Konzipierung des Magneten ergeben: sie enthüllten das fehlerhafte Konzept der Rahmenstruktur und damit das Versagen des ersten Prototypen bei lediglich 70% des Nominal-Stromes (Kapitel 4.4). Der Konstruktions-Ansatz einer anderen Firma wurde durch den erfolgreichen zweiten Prototypen bestätigt (Kapitel 6.3.2). Während der Tests wurden wichtige Komponenten wie kryogene Überspannungs-Schutzdioden (Kapitel 6.3.2) und Quench-Heizer (Kapitel 6.3.6) überprüft.
Im Experiment PENeLOPE ist eine Vermessung des Magnetfeldes notwendig, um sicher zu gehen, dass der Feldverlauf der geplannten Feldkonfiguration entspricht. Das Testsystem wurde daher um eine Magnetfeld-Messeinrichtung erweitert (Kapitel 5.1). Der Aufbau zeichnet sich aus durch eine einzige Vakuumdurchführung für die gleichzeitige Überführung der Bewegung eines Linearverschiebetisches für alle drei Raumrichtungen von ausserhalb des Kyostaten über einen langen Hebelarm in sein Inneres. Die Präzision und Wiederholgenauigkeit wurde ausführlich untersucht (Kapitel 5.2): auch nur geringes mechanisches Spiel im Aktuator wird durch den langen Hebelarm verstärkt, so dass die Genauigkeit in der Positionierung des Magnetfeldsensors auf einige wenige mm beschränkt ist. Algorithmen zur Analyse der Messdaten wurden entwickelt. Diese umfassen insbesondere die Rekonstruktion des Magnetfeldes aus Projektionen, gemessen in einem schiefen Koordinatensystem (Kapitel 5.4). Exemplarisch wurde die Lage des ersten Prototypen im Kryostaten durch die Lokalisierung des Feldminimums in seinem Zentrum mit einer Genauigkeit von besser als 0,5 mm bestimmt (Kapitel 5.5.3). Dafür wurden verschiedene Minimum-Such-Algorithmum verglichen. Aus der bei den Messungen gewonnenen Erfahrung ergeben sich konzeptionelle Verbesserungen für die Messeinrichtung in PENeLOPE.
Die Auswahl des Detektors für die Zerfallsteilchen ist besonders wichtig, da er in der harschen Umgebung eines Flüssighelium-Kryostaten die Anforderungen für eine präzise Vermessung der Neutronenlebensdauer erfüllen muss (Kapitel 7). Dies umfasst im speziellen die Möglichkeit des Einzelprotonen-Nachweises, ein sehr geringes Rauschen und eine gute Zeitstabilität der Signal-

charakteristik. Bei der Wahl des Detektorkonzeptes, ist dessen Machbarkeit zu beweisen, sowie aus verschiedenen Alternativen der Detektor mit den besten Eigenschaften zu finden. In dieser Arbeit werden Studien zur möglichen Realisierung des Detektors auf Basis von Mikrokanalplatten (MCPs) vorgestellt. Ein Detektor mit einem selbst-entwickelten Gehäuse (Kapitel 7.3.3) wurde mit einem gekauften kompletten Detektor verglichen. Die Studien konzentrieren sich auf erste Messungen mit α-Teilchen und Protonen (Kapitel 7.3.6 und 7.3.7). Protonen im interessanten Energiebereich ($10 - 30\,\mathrm{keV}$) konnten eindeutig nachgewiesen werden, wenn auch ein dürftiges Signal-Rausch Verhältnis vorhanden war. Die Spektren weisen ein peak-to-valley Verhältnis von maximal 2.5 auf; das impliziert einen Anteil von 12% misinterpretierter Protonen-Ereignisse. Dieser Umstand und eine geringe aktive Flächenabdeckung ($\approx 50\%$) stellen die Verwendung eines MCP-Detektors in PENeLOPE stark in Frage.

Contents

1. The neutron lifetime

The free neutron is subjected to the decay into a proton, electron and anti-electron neutrino

$$n \longrightarrow p + e^- + \overline{\nu_e} + 0.783\,\mathrm{MeV}$$

with a characteristic lifetime of approximately 15 minutes. Since 1950 the neutron lifetime τ_n has been measured many times using different techniques. [DS11] These days it is still known only with a precision of 10^{-3}, the absolute value being under strong discussion. [N+10]

1.1. Previous measurements and current status

There are mainly two complementary techniques used to measure the neutron lifetime τ_n: In beam-experiments a well-defined section of a beam of neutrons is observed, τ_n measured by the extraction and time-resolved counting of the charged neutron decay products. The main challenge is the precise knowledge of the sample size, thus the neutron flux in the experimental volume, which entails an absolute calibration of the neutron flux monitor. [N+05]
The second possibility, storing low-energetic neutrons in traps - material, gravitational or magnetic ones (see section 2) - is in general the superior technique, having produced the most precise measurements so far. Here, the experiments are limited by trap losses leading to storage times τ_st smaller than the neutron lifetime; extrapolation to zero losses ($\tau_\mathrm{loss} \to \infty$) is necessary to determine τ_n:

$$\frac{1}{\tau_\mathrm{st}} = \frac{1}{\tau_\mathrm{n}} + \frac{1}{\tau_\mathrm{loss}}$$

Especially problematic are unknown trap losses at the collision of the neutrons with the material walls. [S+04] [BP05]
A detailed review of the various lifetime experiments and the applied techniques is given in [Pau09]. In figure 1.1 the measurements contributing to the world average published by the Particle Data Group (PDG) are depicted. The neutron lifetime was mainly determined by two contradicting experiments, both material storage experiments: the measurement by Arzumanov et al. from the year 2000 ($\tau_n = 885.4 \pm 0.9_\mathrm{stat} \pm 0.4_\mathrm{sys}$) [A+00] and by Serebrov et al. in 2005 ($\tau_n = 878.5 \pm 0.7_\mathrm{stat} \pm 0.3_\mathrm{sys}$) [S+05]. Their values differed by more than seven standard deviations, so that the PDG refrained from including the value measured by Serebrov et al. in the official world average for the time being. Recently, the Arzumanov group has re-analysed their experiment, reducing their resulting lifetime to $\tau_n = 881.6 \pm 0.8_\mathrm{stat} \pm 1.9_\mathrm{sys}$. [A+12] The PDG has accounted for that with a new official lifetime of 880.1 ± 1.1s. Although the recent results mitigate the situation, a new, precise experiment could contribute to clarification especially since the neutron lifetime is an important input parameter for models in particle physics and cosmology. Moreover, the correction by re-analyses of the measurement shows how delicate a precise neutron lifetime measurement is.

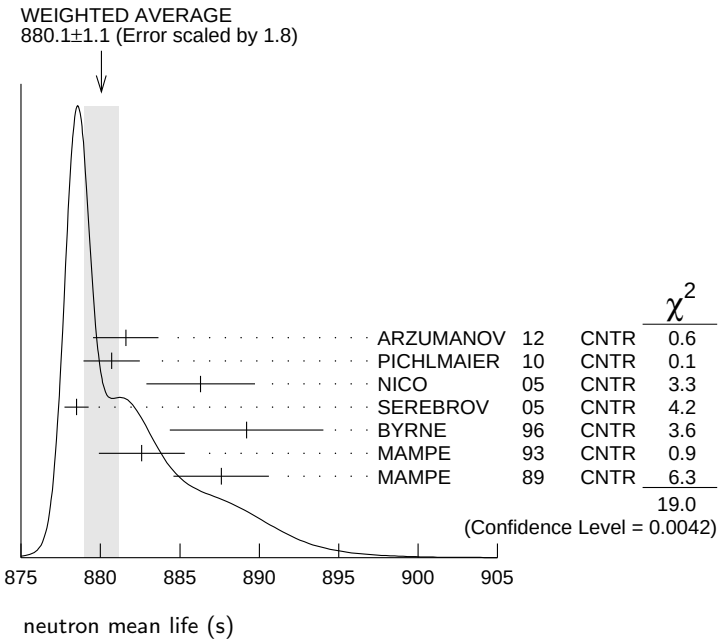

Figure 1.1.: The current status of the neutron lifetime. [B+12] The shaded band shows the position of the weighted average, including its error, which is scaled by a factor $S = (\chi^2/N-1)^{1/2}$. This accounts for the large spread of the results of the N measurements. The column on the right gives the contribution of each of the experiments to $\chi^2 = \sum_i w_i(\bar{x} - x_i)^2$ with $\bar{x}$ being the weighted average, x_i the value of the ith experiment with the weight $w_i = 1/\delta x_i^2$ according to the experimental error δx_i. The black curve in the ideogram is the sum of all the measurements each represented by a Gaussian with a central value x_i, error δx_i and an area proportional to $1/\delta x_i$, respectively.

1.2. Neutron decay - observables and their connection to parameters of theoretical models

The nuclear beta decay is a semi-leptonic process, which is governed by the weak interaction and involves the lightest leptons (e, $\bar{\nu_e}$) and quarks (u, d) interacting via the exchange of the charged vector bosons $W^{\pm}$. The neutron not only offers a clean environment to study the β-decay, since nuclear structure effects are absent, but the process is by far overdetermined having much more observables than fundamental parameters to describe it. The neutron lifetime can be calculated from

$$\tau_n^{-1} = V_{ud}^2 G_F^2 (1 + 3\lambda^2) \frac{f^R m_e^5 c^4}{2\pi^3 \hbar^7}$$

with the phase space factor f^R, the electron mass m_e and the universal Fermi coupling constant of the weak decay G_F. V_{ud} and λ are two important parameters of the standard model of particle physics:

V_{ud} and quark mixing According to the quark-picture, the neutron consist of three quarks, two d-quarks and one u-quark. In the beta decay, one of the constituent d-quarks transforms into a u-quark under the emission of a W^--boson, which in turn decays to an electron and an electron anti-neutrino (see figure 1.2). Comparing this semi-leptonic process to the μ-decay, a pure

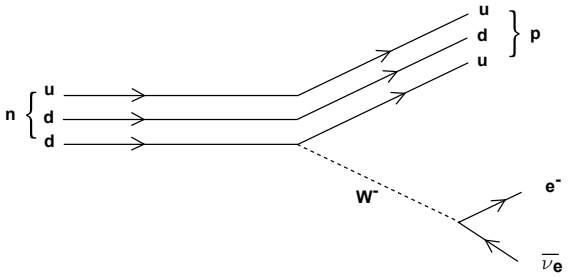

Figure 1.2.: The neutron decay in the quark picture.

leptonic weak decay, it turns out that the weak coupling strength is not identical for these two processes. This is explained by introducing the quark-mixing: It is assumed that the eigenstates of the quarks in the weak interaction are a linear superposition of the mass eigenstates, which are taking part in the electro-magnetic and strong interactions. E.g. not the d-quark is weakly interacting but $d' = d \cdot \cos\theta + s \cdot \sin\theta$, where $\theta = 0.22$ is the Cabibbo angle. Incorporating all three quark families, the mixing is described by the Cabibbo-Kobayashi-Maskawa (CKM) matrix. By convention only the negatively charged quarks are subjected to this mixing.

$$\begin{pmatrix} d' \\ s' \\ b' \end{pmatrix} = \begin{pmatrix} V_{ud} & V_{us} & V_{ub} \\ V_{cd} & V_{cs} & V_{cb} \\ V_{td} & V_{ts} & V_{tb} \end{pmatrix} \begin{pmatrix} d \\ s \\ b \end{pmatrix}$$

According to the standard model, the CKM-matrix has to be unitary, implying

$$|V_{ud}|^2 + |V_{us}|^2 + |V_{ub}|^2 \stackrel{!}{=} 1$$

λ and weak interaction couplings The experimental finding of (maximum) parity violation in weak processes lead to the so-called V-A theory for the weak interaction. Experiments showed that particles come in two versions, as left-handed and as right-handed, and only left-handed particles and right-handed anti-particles take part in weak interactions. The handiness is expressed theoretically with the chirality: left-handed particles have an Eigenvalue of the chirality operator γ^5 of -1 and their wave function ψ is odd under parity transformations, whereas the wave function of right-handed particles, with an Eigenvalue of +1, is even. Thus, to incorporate the parity violation of the weak interaction into the theoretical description, the representation of the weak interaction, i.e. its Lagrangian $\mathcal{L}$, needs to have two components, which behave differently under parity transformation, and are combined in a way that only the left-handed part of the particles wave function is taking part in the interaction. This is realized via the difference of a vector (V) operator γ_μ and the axial-vector (A) operator $\gamma_\mu\gamma_5$: $\gamma_\mu(1-\gamma_5)$.
In neutron decay not the free quarks and leptons interact, but the quarks are bound in a system. The internal nucleon structure affects the actual coupling strengths to the vector and axial vector parts; this is taken into account by introducing energy dependent form factors, mainly $g_1(q^2)$ for the vector and $f_1(q^2)$ for the axial-vector component; q^2 being the momentum transfer. The transition energies in neutron decay are so low compared to the nucleon mass that the form

factors only need to be calculated at zero momentum transfer $q^2 = 0$. The ratio of these two zero-momentum form factors is conventionally named

$$\lambda = \frac{g_1(0)}{f_1(0)} \equiv \frac{g_A}{g_V}.$$

In the end, this is the only parameter needed to account for the complicated internal structure of the neutron. For more details see [DS11] and [Abe08].

Experimental access Besides the lifetime τ_n, the neutron decay comprises several other observables. Namely, these are the correlations between the orientation of the neutron spin $\vec{\sigma_n}$ and the momenta $\vec{p_e}$, $\vec{p_\bar{\nu}}$ and $\vec{p_p}$ as well as the spins $\vec{\sigma_e}$, $\vec{\sigma_\nu}$ and $\vec{\sigma_p}$ of the decay products, respectively. The β-decay transition probability can also be expressed in terms of these observables:

$$W dE_e d\Omega_e d\Omega_\nu \propto F(E_e) d\Omega_e d\Omega_\nu \left[1 + a\frac{\vec{p_e}\vec{p_\bar{\nu}}}{E_e E_\bar{\nu}} + b\frac{m_e}{E_e} + \langle\vec{\sigma_n}\rangle\left(A\frac{\vec{p_e}}{E_e} + B\frac{\vec{p_\bar{\nu}}}{E_\bar{\nu}} + D\frac{\vec{p_e}\times\vec{p_\bar{\nu}}}{E_e E_\bar{\nu}} + ...\right)\right].$$

Here, $F(E_e) = p_e E_e (E_0 - E_e)^2$ denotes the electron energy spectrum with E_e, $E_\bar{\nu}$ the kinetic energies of the electron and the anti-neutrino, respectively. a, A, B and D are the correlation coefficients and b is the so-called Fierz term. The correlation coefficients are only dependent on λ; e.g it is:

$$a = \frac{1 - |\lambda|^2}{1 + 3|\lambda|^2}, \quad B = 2\frac{|\lambda|^2 - \Re(\lambda)}{1 + 3|\lambda|^2}$$

Thus, these observables give access to λ and together with τ_n a determination of the uppermost left matrix element V_{ud} is possible. Hence, precision measurements of the n-decay can contribute to a test of the unitarity and therewith the validity of the standard model of particle physics. All important semi-leptonic cross sections used in cosmology, astrophysics and particle physics include V_{ud} and λ and thus are based upon neutron decay data.

1.3. Current status of $|V_{ud}|$ and λ

The unitarity of the CKM matrix implies the sum of the squared elements of one row of the matrix to be equal to one. The elements of the first row have been determined with the highest precision so far, so that $|V_{ud}|^2 + |V_{us}|^2 + |V_{ub}|^2$ has an uncertainty which is more than one order of magnitude lower than the corresponding sums using the second or third row. [DS11]
With 95% $|V_{ud}|^2$ has the largest contribution. The best determination of $|V_{ud}|$ comes from the study of super-allowed nuclear beta decays between states of the same quantum number configuration $J^\pi = 0+$ and isospin $T = 1$. Currently, the most precise result is $V_{ud} = 0.97425(22)$, by Hardy and Towner from 2005, updated 2008. [HT05] [HT09] [IST10] The official PDG value averages over 20 measurements and yields

$$|V_{ud}^{\mathrm{PDG}}| = 0.9747(15). \text{ [N}^+\text{10]}$$

With $|V_{us}| = 0.2252(9)$, extracted from Kaon decays, and $|V_{ub}| = (3.89 \pm 0.44) \cdot 10^{-3}$, determined in B-decays, the unitarity check sum yields 0.9999(6). [N$^+$10] [IST10]
Vice versa, calculating V_{ud} assuming unitarity gives $V_{ud}^{\mathrm{CKM}} = 0.97430(21)$, which agrees with the Hardy and Towner value.

Using purely neutron beta decay data, V_{ud} can be expressed as a function of λ with τ_n being a parameter [DS11]:

$$V_{ud}^2 = \frac{4908.7(1.9)}{\tau_n(1+3\lambda^2)}$$

The error of the constant is mainly due to theoretical uncertainties in the calculation of radiative corrections.
The ratio of the effective coupling constants is currently stated to be

$$\lambda^{\mathrm{PDG}} = -1.2694 \pm 0.0028$$

by the PDG; latest results of measurements of the asymmetry coefficient A by the UCNA experiment suggest a lower value of $\lambda = -1.2759^{+0.00409}_{-0.00445}$ but agrees within the error bars. [L+10b] The most precise value of λ has been deduced from measurements of A with PERKEOII by Abele et al.'08. [Abe08]
The data is summarized in figure 1.3. The large discrepancy in measurements of τ_n affects, of

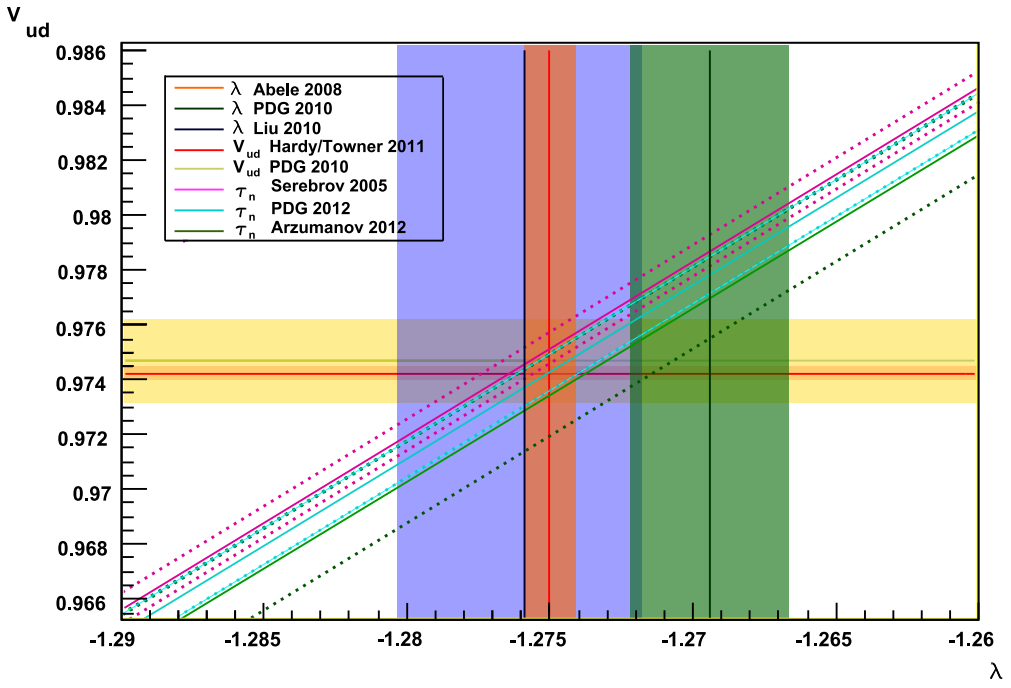

Figure 1.3.: Current status of $|V_{ud}|$ and λ. The shaded areas denote the errors of the given V_{ud} and λ values, respectively. The dotted lines mark the uncertainties of V_{ud} as a function of the various neutron lifetime results.

course, also the overall picture. Whereas, the lifetime value of Serebrov et al. [S+05] nicely agrees with λ by Abele et al. [Abe08], which is also supported by the Liu et al. [L+10b] measurement, the τ_n value by Arzumanov et al. [A+12] favours a much higher λ. Both combinations agree with the limits given by the measurement of V_{ud} performed by Hardy et al.'08. In order to resolve the tangled situation, a new, clear measurement of the neutron lifetime with high precision is mandatory.

1.4. Neutron lifetime in cosmology

According to the standard model of cosmology, the Big Bang theory, the history of the universe started with a singularity: from an extremely dense and hot state, the universe expanded and cooled down, along the way undergoing several phase transitions and condensations of particles and structures. The neutron lifetime plays a big role in the creation of the first light elements, especially ^{4}He: After the formation of the nucleons in the baryogenesis, up to $\approx 1\,\mathrm{s}$ after the big bang, the universe was in thermal equilibrium and neutrons and protons were transformed into each other by the weak reactions:

$$\begin{aligned} n + e^+ &\rightleftharpoons p + \bar{\nu_e}, \\ n + \nu_e &\rightleftharpoons p + e^-. \end{aligned}$$

The abundances of the nucleons, N and P, were dictated by the temperature of the universe T at that time and the difference of their masses $\Delta mc^2 = 1.293\,\mathrm{MeV}$ and followed the Boltzmann distribution

$$N/P = e^{-\Delta m/kT}.$$

At $t \approx 2s$, when the temperature of the universe in terms of energy dropped below about $kT = 0.7\,\mathrm{MeV}$, the so-called freeze-out of the weak interaction took place: because of the tiny cross-section of the weak nucleon-neutrino processes, in the expanding universe with ever decreasing number densities, the nucleons and neutrinos could not interact anymore and the neutrinos decoupled from thermal equilibrium. The precise time of the decoupling is dependent on the weak-interaction cross-sections, thus on λ. Consequently, the reactions, mutually transforming neutrons and protons, died out and the neutron was left to its free decay. Approximately 150 s later the universe had cooled down so much that the fusion of protons and neutrons into the first light elements could effectively set in. Besides the temperature, this moment is given by the photon density and the nuclear binding energies as the effective onset of the so-called nucleosynthesis is delayed due to photo dissociation. At that time, the neutron-proton number ratio - now only dictated by the neutron lifetime - had reduced to $N/P \approx 1/6$; in turn, the amount of neutrons present dictates the abundance of the light elements that could be formed in the primordial nucleosynthesis: ^{2}H, ^{3}He, ^{4}He and ^{7}Li. Due to its large binding energy, ^{4}He is by far the biggest fraction, the abundance being six orders of magnitude larger than for the other elements.
With extensive model calculations of the nucleosynthesis, the abundance of ^{4}He can be predicted as a function of the baryon-to-photon density ratio $\eta_{10} = n_b/n_\gamma$ and the neutron lifetime [Ste07]:

$$Y_p = 0.2483 \pm 0.0005 + 0.0016(\eta_{10} - 6) + 2 \cdot 10^{-4}(\tau_n - 885.7).$$

The data is depicted in figure 1.4. Experimentally, the ^{4}He mass fraction $Y_p = {}^{\text{He-4 mass}}/_{\text{total mass}}$ after the primordial nucleosynthesis can be extracted from extrapolating measurements of helium and hydrogen emission lines in very old parts of the universe. [I$^+$09] From extragalactic HII regions with low metallicity (elements beyond mass number $A = 4$) it is extrapolated to zero metallicity. [1] The baryon-to-photon ratio in the early universe follows from measurements of the microwave background: $\eta_{10} = (6.185 \pm 0.153) \cdot 10^{-10}$. [L$^+$10a] The data is consistent with both neutron lifetimes, the Serebrov and the Arzumanov value, due to the fact that observations of the

[1] HII regions are huge, low-density clouds of partially ionized gas, mainly atomic hydrogen gas ($\approx 90\%$). Most of the rest is helium. The lack of isotopes with higher masses indicates low star formation activity and therefore conditions like in the early universe are assumed.

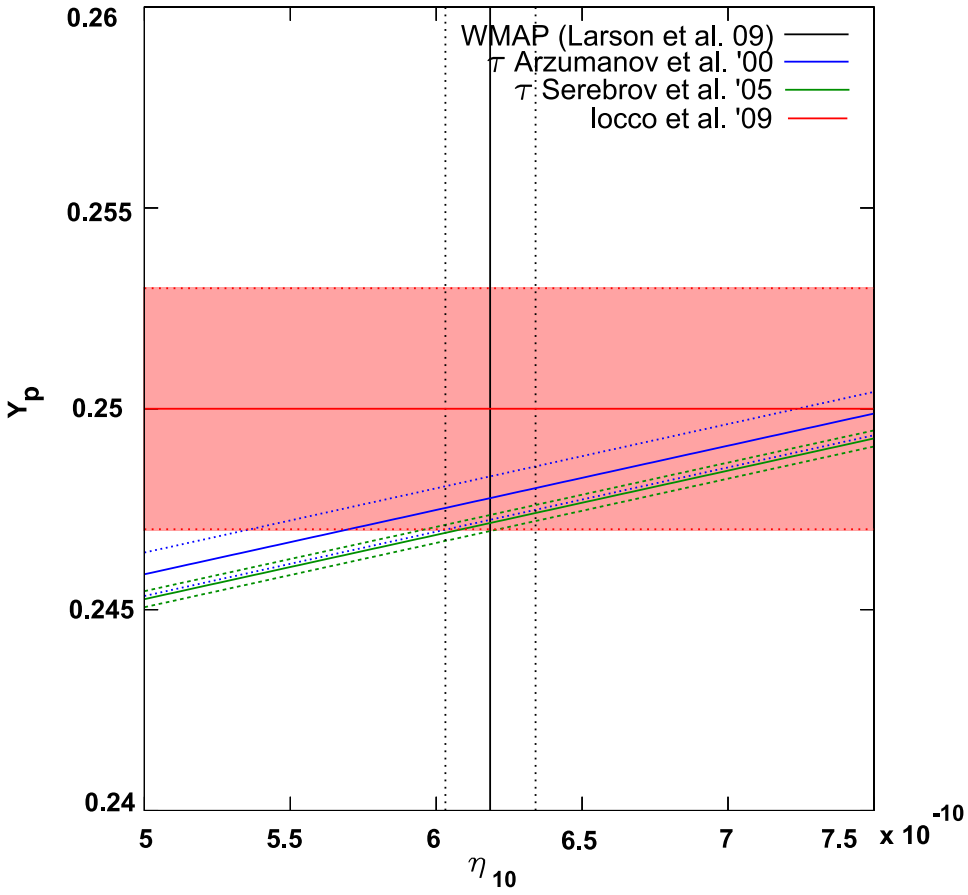

Figure 1.4.: Helium abundance Y_p as a function of baryon-to-photon ratio η_{10}, a measure for the mass content of the universe. For more details see the text.

helium abundance and the photon density are still afflicted with large uncertainties. Despite, the neutron lifetime is one of the main parameters in Big Bang nucleosynthesis models and reducing its error completes the overall picture.

2. Ultra-cold neutrons

Neutrons are usually classified according to their energies and labeled with the corresponding temperature of an ideal neutron gas. Ultra-cold neutrons (UCN) are at the lowest end of this classification and have energies up to a few hundred neV. At these low energies, neutrons can be manipulated and thus trapped for longer observation times by three means: via their interaction with matter, via their potential energy in the earth gravitational field and via magnetic fields acting on the neutron magnetic moment. Details can be found in [Gol91].

Gravitational potential The mass of the neutron m_n implies a potential energy in the earth gravitational field of $U_\mathrm{g} = m_n g = 102\,\mathrm{neV/m}$. Thus, a neutron with a kinetic energy of 250 neV can ascend only 2.44 m. This allows to shift the energies of the probed neutrons by just guiding them to different heights. In laboratory sized traps, the top can be left open - the low-energetic neutrons still being confined gravitationally - to install further experimental equipment without taking care of their neutron-specific material properties.

Magnetic interaction potential The neutron has a spin and thus a magnetic moment $|\vec{\mu_n}| = 60.3\,\mathrm{neV/T}$. In an inhomogeneous magnetic field $\vec{B}$ a force is acting on the magnetic moment: $\vec{F} = -\nabla(\vec{\mu_n}\vec{B})$. Depending on the orientation of the neutrons magnetic moment to the magnetic field lines, the neutrons are repelled or attracted by higher field regions. Hence, they are classified into high-field seekers and low-field seekers. The latter can be trapped in a low-field region surrounded by a large magnetic field. As the energy of the neutrons that can be stored is limited by the field strength reachable with laboratory magnets (across a reasonable trap volume), only ultra-cold neutrons can be stored magnetically: for a neutron energy of 250 neV already a flux density of $\approx 4\,\mathrm{T}$ is needed.

Fermi potential The interaction of neutrons with matter is quantum-mechanically described by the neutron represented via a wave function scattering at the nuclear potential. Using an ansatz from perturbation theory, this can be described by the interaction of the neutron with a pseudo-potential, the so-called Fermi potential V_F. As the neutron - having a wavelength much larger than the inter nuclei distance in condensed matter [2] - scans many nuclei at once, the sum over all the single scattering amplitudes on the individual nuclei has to be taken. For a homogeneous material the Fermi potential simplifies to

$$V_\mathrm{F} = \frac{2\pi\hbar^2}{m_n} n b,$$

where n is the number density of the material and b the bound neutron scattering length.
Neutrons hitting the material with a kinetic energy smaller than this material-specific Fermi potential are totally reflected under all incident angles.
Still, the neutron penetrates into the material in the order of its wavelength, and the Fermi potential is extended with an imaginary part describing the possible absorption or scattering of the neutron to higher energies in the material:

[2] For $E_\mathrm{kin} = 250\,\mathrm{neV}$ the wavelength is $\lambda_n = 570\text{Å}$.

$$U_{\text{F}} = V_{\text{F}} + iW_{\text{F}},$$

with

$$W_{\text{F}} = \frac{\hbar}{2} n \sigma_l v,$$

where σ_l is the loss cross section and v the neutron velocity.
In table 2.1 the Fermi potentials of various materials commonly used in neutron experiments are listed. Exploiting this feature, neutrons can be guided in material tubes and stored in material

material	$\mathbf{V}_{\text{F}}$ (neV)	$\mathbf{W}_{\text{F}}$ (neV)	**usage**
stainless steel	183.04	0.085	reflector
aluminum	54.2	0.0076	reflector
diamond-like carbon (DLC)	256	0.032	reflector
nickel	244.4	0.15	reflector
polyethylene	-8.56	0.492	absorber
titanium	-50.8	0.043	absorber

Table 2.1.: Fermi potential - real V_{F} and imaginary part W_{F} - of various materials. [Sea92]

vessels if their energies are low enough. Again, only ultra-cold neutrons have energies smaller than typical Fermi potentials.[3]

[3] In fact, the energy range of the neutrons being classified as ultra-cold is defined by total reflection at material walls under all incident angles.

3. PENeLOPE - Precision Experiment on Neutron Lifetime Operating with Proton Extraction

PENeLOPE, built up at E18, Physik-Department of TU München, is a new neutron storage experiment to measure the neutron lifetime with a precision of 0.1 s. A detailed description of the experimental concept can be found in [Pic08] and [MP+09]. As briefly mentioned in chapter 1, material storage experiments suffer from systematic errors correlated to the interactions of the UCN with the trap walls. These interactions lead to UCN losses beside the neutron decay and thus impose a false effect as they artificially reduce the measured neutron lifetime. To avoid this difficulty in PENeLOPE, the neutrons will be stored magnetically (cf. section 2). Furthermore, in former storage experiments, the neutron lifetime has been extracted by measuring the number of surviving neutrons after various storage times. This way, only few different storage times are realizable, due to the limited density of stored neutrons and the need for repetitions of measurements to reduce the statistical error. Thus, the decay curve is only probed at a few selected points. However, in PENeLOPE the top of the trap can be left open as the UCN are kept by gravitation. This allows to extract the charged decay particles onto a detector above the trap volume. Time-resolved counting of the decay particles during a single storage phase continuously probes the neutron decay curve. This gives a second measuring principle besides neutron counting. A large trap potential combined with a big trap volume and the larger neutron flux expected at the next generation UCN sources provides good statistics; hence, extensive studies on systematic effects can be performed. A schematic view of the experiment is given in figure 3.1; details will be discussed in the following sections.

3.1. Magneto-gravitational storage

For magnetic neutron storage a magnetic field gradient is needed. The neutrons are stored in a low-field region surrounded by higher magnetic fields. In PENeLOPE, this configuration is realized by a stack of 13 solenoids, which are powered with alternating current direction. The bottom of the trap is built up out of four concentric superconducting coils. The trapping potential U for the neutrons sums up from the magnetic and the gravitational potential:

$$U(h) = -\mu_n B + m_n g h$$

The larger the trap depth, the more neutrons can be stored, especially since the differential UCN flux increases with the square root of the energy.[4] Only superconducting magnets can deliver the strong fields needed to satisfy statistical demands. Ultra-cold neutrons with energies of up to 115 neV with respect to the cryostat bottom shall be stored; this results in a peak magnetic field of 5.5 T in the planned magnet configuration. [5] About $8 \cdot 10^6$ stored UCN per filling are

[4] The typical spectrum of a super-thermal UCN source is $\frac{d\phi}{dE} \propto \sqrt{E}$. [GP75]

[5] The maximal field generated by the coil assembly is much higher than the maximal field seen by the neutrons and thus used to store the neutrons.

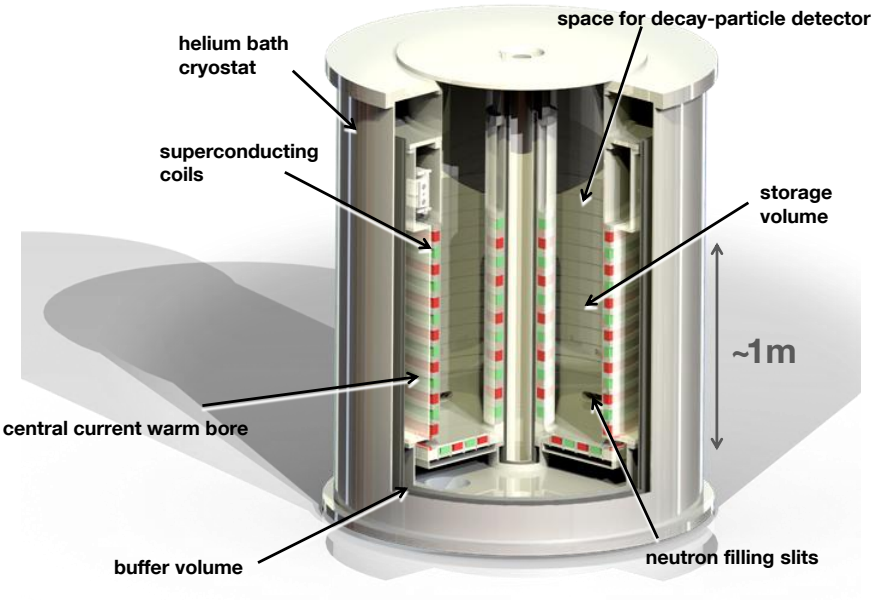

Figure 3.1.: Layout of the PENeLOPE setup.

expected in PENeLOPE, assuming a production rate in the UCN source of 10^7 UCN s^{-1} (details are given in [Sch11b]).

The adiabatic condition of magnetic storage A complication is introduced by the fact that only neutrons of the correct spin orientation can be stored (cf. section 2). Therefore, polarized neutrons will be filled into the PENeLOPE trap. In order to keep the alignment of the neutron spin with respect to the magnetic field, the adiabatic condition has to be satisfied: the ratio of the change of the magnetic flux density seen by the moving neutron to the absolute value of the flux density has to be much smaller than the Larmor precession frequency of the neutron spin around the field lines:

$$\dot{\mathbf{B}}/|\mathbf{B}| \ll \omega_{\mathrm{Larmor}}.$$

If this relation is not met, low-field seeking neutrons might turn via spin flip into high-field seekers and would be lost. Thus, zero-field regions or low-field regions with strong gradients have to be avoided: a vertical, central current generates an azimuthal component that fills up zero-field regions generated by the cylindrically symmetric multi-pole configuration of the storage coils and guarantees a minimum field of 5 mT. To keep neutrons from hitting the central conductor, another 11 storage coils are installed around the center leading to the trap geometry of doubly nested cylinders as depicted in figure 3.1.

Realization of the coil system The magnet of PENeLOPE is a technically challenging, highly-specialized development and the co-operation with an industry partner, expert in superconducting magnets, is mandatory. A feasibility study was started with Scientific Magnetics in 2005.

After a positive outcome, this was followed by the construction of a prototype coil pair and a detailed design phase. During this phase, Scientific Magnetics started questioning the principle feasibility of the magnet. Moreover, essential experiment features like the storage potential of 110 neV originally aimed for should have been discarded in favor of the support of the magnet.[6] Finally, the first prototype revealed bad performance during testing (see chapter 4). All this lead to the decision to change the coil manufacturer. With Babcock Noell a new feasibility study was started in 2010, once more with a positive outcome. A thorough revision of the whole design lead to the setup briefly described above: the number of coils could be reduced from 44 to 28 and more space for the support structure was attained. At the same time, the peak magnetic field reduced from 6.1 to 5.5 T while increasing the trap depth from 110 neV to 115 neV. In the detailed design phase of the setup, again a prototype magnet was constructed. Tests with this prototype - described in chapter 6 - succeeded fully, confirming the approach taken by Babcock Noell.

3.2. Detection of decay particles

In neutron decay, the protons and electrons will be emitted into full $4\,\pi$ solid angle. Thus, they have to be guided to the detector by electrical and magnetic fields. The energy distribution of the electrons reaches up to ≈ 750 keV, for protons only up to ≈ 750 eV. The strength of an electrical field needed to efficiently manipulate the electrons would be far beyond technical feasibility, whereas for the protons - at first glance - a potential of only a few kV would suffice. However, the charged particles will follow the dominant, strong magnetic field and spiral around the field lines. A z-directed magnetic field can be used to guide them to the top of the trap. Hence, every second outer storage coil will bear a slightly larger total current.[7] The magnetic mirror effect assures the extraction of the protons even if they are emitted into the lower hemisphere.[8] In figure 3.2 the field configuration is depicted. Unfortunately, this coil configuration results in an increase of the field strength also at the top of the trap and creates another magnetic mirror in front of the detector. Hence, an electrical field is needed to lift the protons over the barrier. This is implemented by setting the detector itself on large negative voltage. The installation of extraction electrodes over the whole length of the trap volume is an additional option, but is complicated by the limited space available between the inner cryostat wall and the trap boundary. Any installation must have good neutron optical properties not to affect neutron storage negatively.
In figure 3.3 simulation results of the extraction efficiency as a function of the detector voltage are depicted. At 0 V the efficiency for electrons and protons is around 40%. The value is given by the solid angle covered by the detector, folded with the magnetic field line geometry. For the protons, the efficiency saturates above 20 kV at around 70%. In contrast, as expected, the electrons are only slightly affected by the voltage and their extraction efficiency stays at $\approx 40\%$. The possible detection principles to count the decay particles are discussed in detail in chapter 7.

[6] The thickness of the magnets support structure should have been increased from 10 to 15 mm. In turn, this would have reduced the storage potential by 30%, as the trap boundary would have had to move further away from the magnet into lower field regions. This would imply a factor of three less neutrons in the trap.

[7] Keeping the packing factor (see section 6.3.1 for a definition) and current constant for all coils, this is achieved by adjusting the number of winding layers of the coils: coils with 'positive polarity' have two layers less than the coils with 'negative polarity' and thus the total current is reduced by 6%.

[8] This effect occurs when the field strength increases while a charged particle is spiraling along a magnetic field line. It leads to the tendency for the particle to be repelled from the high field region.

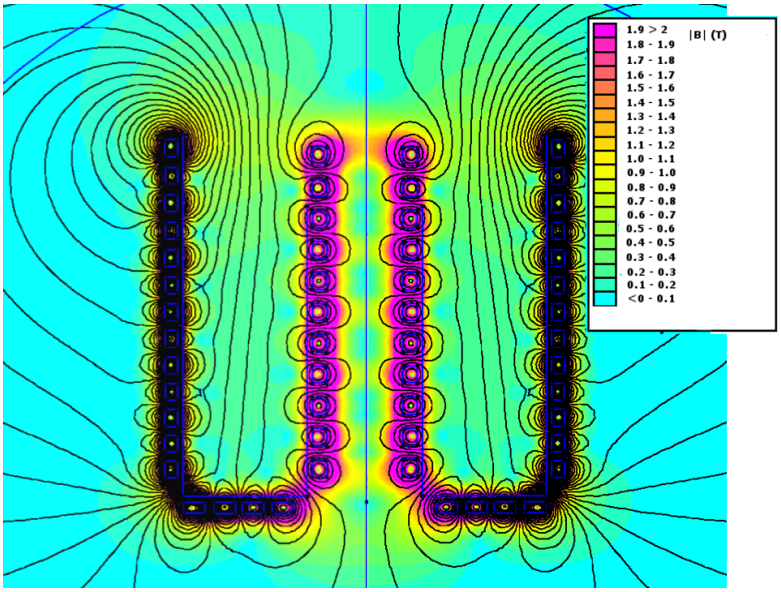

Figure 3.2.: Cross sectional view of the magnetic field in the PENeLOPE setup calculated with a FEMM program. The blue lines suggest the coils and the cryostat. The absolute magnetic field is given color-coded, whereas the field lines are drawn in black lines. The squeezing of the field lines at the top of the trap leads to the magnetic mirror effect for charged particles.

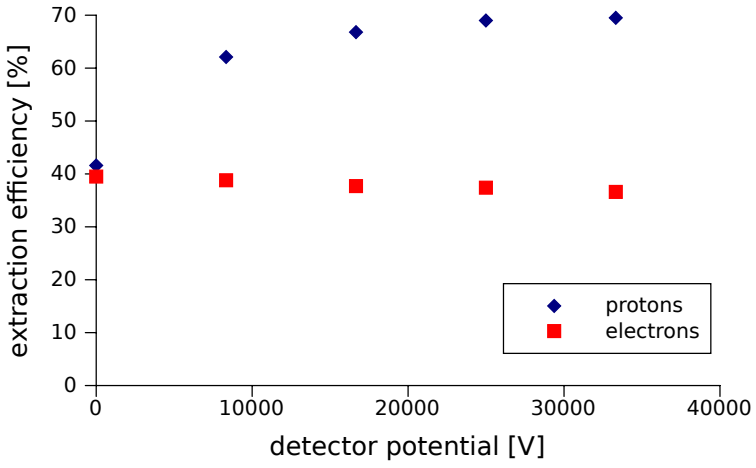

Figure 3.3.: Extraction efficiencies of electrons and protons depending on the electrical potential of the detector plane. [Sch11b]

4. CoTEx - Coil Test Experiment

To trap UCNs magnetically and measure their lifetime, a special multi-pole arrangement of the field coils is needed that has to fulfill several requirements. These make the PENeLOPE magnet a highly complex system:

- First of all, the envisaged potential depth of 115 neV demands for large magnetic fields and thus a high current density of $\approx 300\,\mathrm{A/mm^2}$. To retain superconductivity of the coils, the combination of magnetic field strength and current density must stay within certain limits depending on the chosen superconductor. In case of the NbTi used for the PENeLOPE magnet the field strength must not exceed e.g. 5.5 T at a current of 370 A.[9]

- Furthermore, due to the multi-pole arrangement of the solenoids, which have alternating current directions, the large magnetic field leads to repelling forces as large as 1.15 MN. These must be taken by the support structure.

- A crucial design parameter of thick and short solenoids is the ratio of the outer radius to the inner radius $\alpha = r_o/r_i$. According to [Wil83], α should be kept below 1.85 to avoid large intra-coil stresses. These could lead to cracking of the resin impregnation of the wires and consequently to an unreliable operation of the magnet. Regarding this parameter, the innermost base coil of the PENeLOPE magnet is the most critical one. For this coil it is $\alpha = 1.29$.

- In PENeLOPE the neutrons will be filled into the trap while the magnetic field is switched off. To minimize the time in which the UCN interact with the material walls, the current in the superconducting coils has to be ramped up as fast as possible. A ramping time from zero to maximal current of less than 100 s is aimed for. Hysteresis losses in the diamagnetic, superconducting filaments as well as eddy currents induced in the coil formers result in considerable heat generation while ramping. [BS11] This heat needs to be transferred efficiently to the liquid helium bath to guarantee a stable operation of the magnet. The design must foresee a temperature margin large enough between the maximal magnet temperature and the transition temperature of the superconductor. In the current design, at a maximum field of 5.5 T the margin is 0.55 K at its lowest.[BS11]

Due to all these requirements, the magnet is a technically challenging custom-made product. In the context of the design study performed by Scientific Magnetics [RGM05], a prototype coil pair has been built to verify the functionality and performance of the coil design. A liquid helium bath cryostat was set up at Maier-Leibnitz-Laboratorium, Garching (MLL). As described in the following chapter, the superconducting magnet has been trained and the operational limits for ramping speed and coil current have been checked.

[9] This limit is also temperature dependent. The given value holds for a temperature of the conductor of $T = 4.9\,\mathrm{K}$. For lower temperatures the limit increases e.g. to 5.5 T / 410 A at 4.7 K. [BS11] Compare also figure 6.14.

4.1. Prototype coils

The prototype magnet, built by Scientific Magnetics, is composed of two solenoids operated in opposite current direction (see figure 4.1). Due to the repelling magnetic forces this configuration simulates the largest stresses expected in the later PENeLOPE magnet for the outermost coils. All other solenoids have more than one neighboring coil and experience lower stresses due to cancellation effects between the coils with the same current direction. The specifications of the prototype are summarized in table 4.1, a technical drawing is given in appendix A.

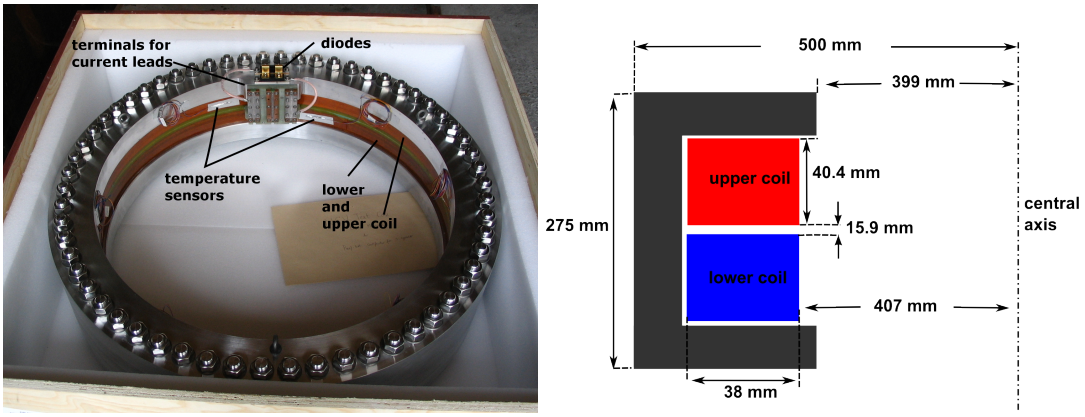

Figure 4.1.: The prototype coil pair. Left: a photography. Right: a schematic cross-sectional side view.

geometry		**operating conditions**	
outer radius of support	500 mm	maximum operating current	248.5 A
inner radius of support	399 mm	current density (w.r.t. complete wire)	317 A/mm^2
weight	300 kg		
height of support	275 mm	stored energy	140 kJ
outer radius of coil r_o	445 mm	maximum field	6.8 T
inner radius of coil r_i	407 mm	nominal ramp rate	2.6 A/s
radial width of coil	38 mm	resistance R at room temp.	414 Ω
height of single coil	40.4 mm	inductance L, theoretical	4.6 H
axial distance of the coils	15.9 mm	inductance L, meas. at 50Hz	3.3 H
windings per coil	1958		
$\alpha = r_o/r_i$	1.09		

Table 4.1.: Specifications of the test magnet from Scientific Magnetics [Sci08]. See also figure 4.1.

The radial dimension of the coils is by 20% smaller than the outer coils in the later PENeLOPE setup as this allowed to use an existing vacuum tank for the cryostat setup.
The superconducting wire used for the magnet is from ALSTOM, has a diameter of 0.825 mm and is made of a NbTi-Cu-compound with a varnish insulation. The copper to superconductor ratio is 1.9 to 1. NbTi has a transition temperature of 10 K. The critical current of the wire at 6.8 T and 4.2 K is about 300 A.

4.2. Cryostat setup

The cryostat for the prototype tests follows the typical onion-like structure of a helium bath cryostat (see figure 4.2). The innermost part is a ring shaped vessel made of aluminum. It contains the magnet and the liquid helium. The ring shaped geometry reduces the volume to be filled with liquid helium. The magnet itself is suspended from the top of the vessel. The helium tank is surrounded by a copper radiation shield cooled down to liquid nitrogen temperature. To further reduce the heat input, the radiation shield as well as the helium tank are wrapped in 15 layers of super-insulation foil. The outermost part of the cryostat is a stainless steel vacuum tank. All parts are suspended from the vacuum tank top which itself is mounted to a support frame. This allows easy access to the inner parts when opening the cryostat from the bottom, whereas all infrastructure installations at the top can remain fixed. The vacuum tank is equipped with a rubber sealing; for the helium tank being at cryogenic temperatures indium seals are necessary. When the cryostat is closed, four supply tubes provide access from the outside to the helium space. To compensate thermal shrinkage of the support and reduce heat input through these connections, they are realized by membrane bellows. Liquid helium is transferred via a 3.5 m long transfer line from a helium liquefier into the aluminum vessel. The liquefier system consists of a helium reservoir ($10\mathrm{m}^3$ at 100 bar), the liquefying unit itself, a receiver balloon of $10\,\mathrm{m}^3$ for the helium gas returning from the cryostat and compressors to pump the gas from this buffer back into the storage containers. The cooling power of the system is $\gtrsim$ 100W at liquid helium temperature.
During operation, important parameters (vacuum, helium pressure, liquid-helium level, system temperatures) are monitored and logged. The current in the coils and the voltage applied are logged; the magnetic field is measured by cryogenic hall sensors. A slow-control including a graphical user interface has been realized with the commercial LabVIEW programming environment.

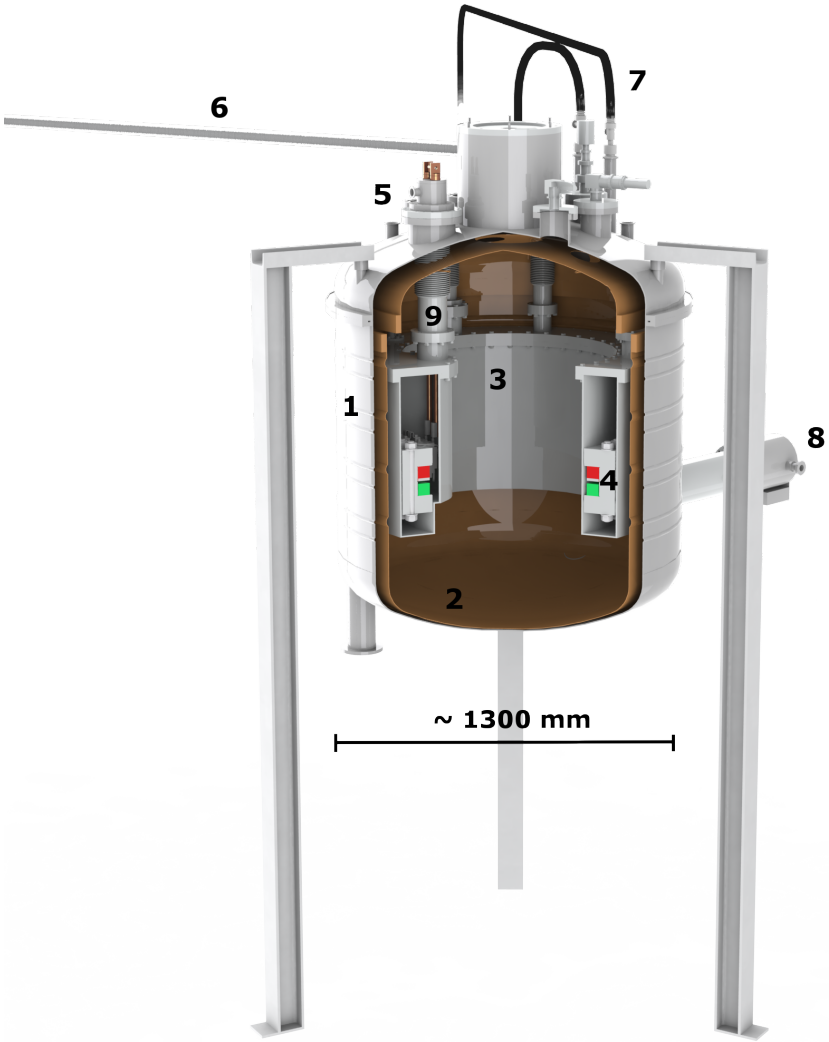

Figure 4.2.: Sectional view of the CoTEx cryostat: 1) vacuum tank, 2) radiation shield, 3) liquid-helium vessel, 4) coils, 5) current feed, 6) liquid-helium transfer line, 7) liquid-nitrogen supply, 8) turbomolecular pump, 9) bellows to access helium space.

4.2.1. Cryostat operation and safety aspects

During normal operation, cooling the radiation shield needs a supply of 1.9 l/h of liquid nitrogen while having an insulation vacuum of 10^{-7} mbar. The cryostat is filled with at least 60 l of liquid helium to cover the coils. The helium boil-off rate is about 9.4 l/h corresponding to a heat input of 7 W to the liquid helium. Part of the helium off-gas is guided through the transfer line to pre-cool this as well as the final stages of the liquefier. The rest is used to cool the current feeds. In case of a quench[10] of the magnet the field energy is transformed into heat which evaporates large amounts of liquid helium within a few seconds. An exemplary quench at a current of 250 A releases the field energy of ~ 141 kJ and would evaporate 53 l of liquid helium if transferred completely to the helium bath. This corresponds to 36 m^3 of gaseous helium at room temperature. The small exhaust lines of the transfer line and the current feed would not be able to carry these huge amounts of gas. To protect the tank against pressure overload, two additional exhaust lines are available, having a diameter of 66 mm each. One is connected to the receiver balloon of the liquefier, the second one is an exhaust to the experimental hall itself. Both lines are equipped with overpressure valves opening at ≈ 0.8 and ≈ 1 bar overpressure, respectively. The helium tank itself as well as the bellows are specified for an overpressure of 1.5 bar against atmosphere. The vacuum tank, which is specified for 300 mbar overpressure only, is protected against overpressure by a blind cover loosely put on one of the CF-100 flanges. When the tank is under vacuum, the pressure difference to the surrounding atmosphere is sufficient to press the blind cover tightly to the flange and still guarantee the insulation vacuum. Already a pressure of ≈ 60 mbar lifts the blind cover, which is secured against an uncontrolled blow-off.
The receiver balloon only has a limited capacity and in case of a quench the compressors are not sufficient to press the helium from the balloon back into the storage containers fast enough. Thus, roughly 20 l of liquid helium are lost during a quench - the amount depends strongly on the characteristics of the quench incident, i.e. the time scale of the energy dissipation.

Helium exhaust At the incident of a quench the current decays within a second or less [Ste11b]. The time constant of helium evaporation is governed by heat conductance in the superconductor and its support structure as well as by heat transfer through interfaces mainly between the liquid helium and the magnet surface. The detailed process is very complex and demands simulations with a realistic model. However, in order to estimate whether the exhaust lines are sufficiently dimensioned, the so-called choked flow is considered [BE08]: When the ratio of the pressure in the tank p_t and in the outlet p_o reaches a critical value, the mass-flow through the exhaust pipe has reached a maximum and stays constant even if the pressure gradient is further increased. At this point the velocity of the outflowing gas has reached its limit at the sonic speed. The maximum possible mass flow at this critical point must exceed the expected boil-off rate in case of a quench to protect the tank against overpressure. The maximum mass flow is given by

$$\dot{m} = \mu \cdot A_{\text{out}} \cdot \psi_{\max} \sqrt{2 p_t \rho_t}.$$

Here, A_{out} denotes the cross-section of the exhaust line, ρ_t and p_t the density and pressure in the tank. Losses due to friction and geometrical resistance are accounted for by the outflow number μ. The outflow function $\psi_{\max}$ is given by

$$\psi_{\max} = \left(\tfrac{2}{n+1}\right)^{\frac{1}{n-1}} \sqrt{\tfrac{\kappa}{\kappa-1} \cdot \tfrac{n-1}{n+1}},$$

where κ denotes the adiabatic exponent and n the polytropic coefficient of the helium gas. The correct choice of the outflow number μ is crucial. With an estimated $\mu = 0.48$ (cf. appendix B)

[10] The phenomenon of going from the superconducting state to the normal resistive state is called quenching. Large currents in the suddenly resistive conductor lead to enormous ohmic heating and build up of large voltages.

the maximal mass flow for one single exhaust line is

$$\begin{aligned} \dot{m}_{\text{real}} &= 0.58\,\text{kg/s} \\ &\equiv 107\,\text{l/s gas at 10 K, 1 bar} \\ &\equiv 6.91\,\text{l/s liquid helium.} \end{aligned}$$

The detailed calculations can be found in appendix B. Usually, sudden loss of vacuum is considered as a worst case scenario for bath cryostats. [Mil09] The experiment-based conservative estimate of $0.6\,\text{W/cm}^3$ heat input for sudden loss of vacuum in a cryostat with multi-layer insulation [LZ78] [XLW10] gives a boil-off rate of

$$\begin{aligned} \dot{m}_{\text{vac.-loss}} &\equiv 189\,\text{l/s gas at 10 K, 1 bar} \\ &\equiv 7.51\,\text{l/s liquid helium} \end{aligned}$$

for the CoTEx cryostat. As already one of the exhaust lines in the CoTEx setup covers nearly the whole expected mass flow, the pressure in the tank is not expected to increase further once the safety valves have opened.

4.3. Magnet power circuit

Two different setups exist to power the prototype magnet (cf. figure 4.3). The first version uses a unipolar DC-power supply from Xantrex. The major draw-back of this scheme is the long duration to reduce the field as the magnetic energy is dumped into the resistive parts of the system. Adding a special energy absorber with a discharge voltage of 5 V for this purpose, allows a faster de-energizing of the magnet. A low-ohmic stabilizing resistor provides a shortcut for high frequency oscillations, and a diode protects the power supply from overvoltage. An AMI Model 420 programmer allows to control the power supply remotely and logs the current by measuring the voltage drop over a shunt resistor.
An alternative setup is realized with a 100 V, 360 A power supply from Danfysik which is also foreseen for the final coil assembly in PENeLOPE. This power supply is bipolar: additional energy absorbers in the circuit are not necessary in this case. Energy dumps and over-voltage protection is incorporated into the power supply. Again, the AMI programmer is used to measure the current as it is more precise than the monitor of the Danfysik power supply.
In both setups cryogenic high-power diodes are connected parallel to the magnet to protect it against large voltages. They are installed directly at the magnet taps, thus immersed in liquid helium. A pair of anti-parallel diodes is installed for each direction. They act as a by-pass for the current until the power supply is shut down, whereas the reverse branch provides open-circuit protection. A sudden break of the outer power circuit generates large inductance voltages; the diodes limit this voltages and provide a closed circuit for the magnet.
A persistent switch, which allows to disconnect the power supply once the magnet is charged, is often used with superconducting magnets. However, this is futile for this test setup, as the magnet will be ramped up and down frequently, as in the later experiment.
Table 4.2 summarizes the specifications of the hardware involved, the circuit diagram of the test setup is given in figure 4.3.

Xantrex power supply XPR 20-300	
max. voltage	+20 V
max. current	+300 A
voltage noise	75 mVpp
current noise	1600 mA
stabilizing resistor	20 Ω
AMI 601 energy absorber	
discharge voltage	5 V
max. current per absorber	130 A
Danfysik power supply	
max. voltage	±100 V
max. current	±360 A
current stability	±100 ppm
voltage ripple	< 0.6 Vpp @17.5 kHz
AMI model 420 programmer	
$I_{\max}$	300 A
measurement resolution	0.6 mA
accuracy of $I_{\max}$	0.1 %
protective diodes	
forward voltage U_f	16 V

Table 4.2.: Specifications of the equipment used to power the magnet.

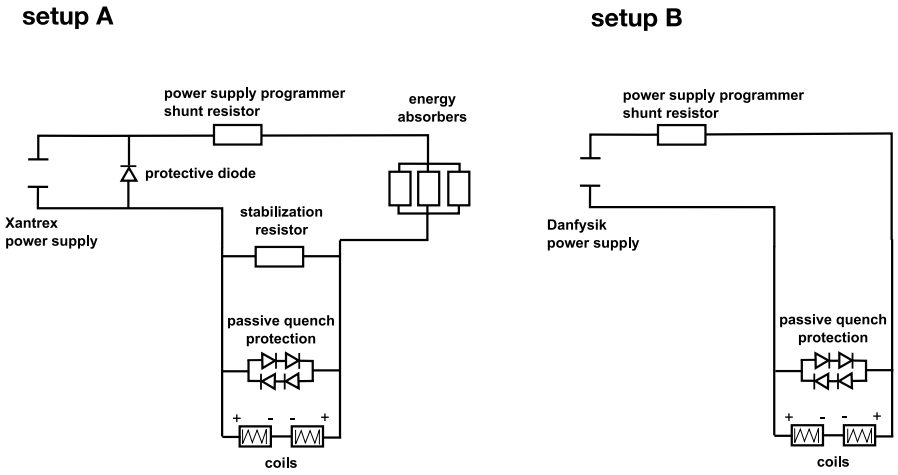

Figure 4.3.: Power circuit of the prototype magnet. Left: using the unipolar XPR power supply and energy absorbers. Right: using the bipolar Danfysik power supply.

4.4. Training of the prototype magnet

A superconducting magnet needs to be trained to its final operating conditions [NB99]: Powering the magnet induces large forces on the wires or between sections of the magnet due to the Lorentz force. These stresses might lead to frictional movement of the wires or coils with respect to each other which in turn generates heat. At cryogenic temperatures the heat capacity of the materials is very low, and even small heat input can increase the temperature significantly and drive the superconductor into its normal conducting phase. Thus, it is not likely the magnet reaches the maximum possible current, when powered the first time but it needs to adjust to the stresses and loads. Energizing the magnet again and again these pre-mature quenches occur at higher and higher currents until saturating at the final operating current the magnet is capable of.
To train the PENeLOPE prototype, the current was ramped up slowly with approximately 1.5 A/s until a quench occurred. Every 20 to 50 A the ramping was interrupted for 60-120 s to let the helium bath system settle to an equilibrium state.[11] In figure 4.4 the quench history of the PENeLOPE test-coils can be seen. It is clear that the design goal of 250 A was never reached. Furthermore, the magnet does not stabilize at a reliable maximum current (cf. quench number 10 in figure 4.4).

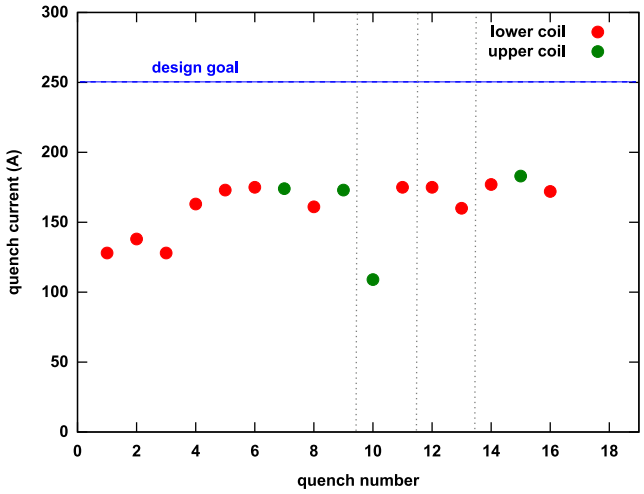

Figure 4.4.: Prototype training curve. The vertical dotted lines mark periods of warming up to room temperatures.

4.4.1. Exemplary quench event

Exemplary, the temperature evolution of the coils is depicted in figure 4.5 for a quench at 183 A: At $t \approx 200\,\mathrm{s}$ the magnet quenches and the temperature of the magnet increases. Three temperature sensors are attached to each solenoid (cf. figure 4.1). As the heat is generated in the resistive zone of the coil that quenched and distributes afterwards, the temperature of this coil increases more than for the other coil. In the test setup, this is the only way to decide which

[11] Although the ohmic resistance is practically zero in superconductors, due to the inductive resistance of the coil, the ramping leads to additional heat input into the cryostat.

of the two solenoids has quenched. In the given example the upper solenoid quenches and the temperature increases up to 40 K. However, the temperatures seen by the sensors are not at all a measure of the peak temperature reached during the quench in the coil. The temperature at the positions of the sensors depend strongly on the location and evolution of the quench as well as the heat conductance in the magnet itself. Moreover, the sensors are only attached to the surface of the magnet and immersed in liquid helium. Thus, the measured temperatures decrease very fast and have dropped below 5 K already 250 s after the incident.

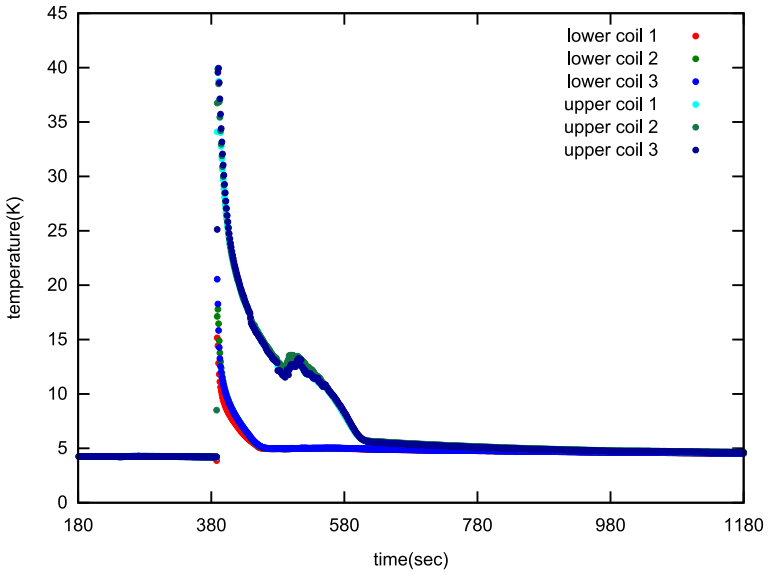

Figure 4.5.: Coil temperatures for an exemplary quench at 180 A.

The evolution of the voltage, the current and the magnetic field for the quench event are presented in figure 4.6. The voltage is directly measured at the magnet taps and the total current I_{tot} logged in the outer circuit by the AMI Model 420 programmer. The magnetic field is measured with a cryogenic hall sensor inside the cryostat. In this case the Danfysik power supply was used. The current is ramped up stepwise with approximately 1 A/s which requires about 5 V. The magnetic field rises correspondingly until at $t \approx 380\,\mathrm{s}$ the quench happens. Due to the resistive zone building up in the magnet, the current stabilizing power supply raises the applied voltage to keep the current up and to guarantee the desired ramp rate. At $V \approx 16\,\mathrm{V}$ the protective diode breaks through, and a second circuit parallel to the magnet opens (see figure 4.7). The rise of the voltage up to the break-through lasts only 50 ms. In figure 4.6 this voltage peak is not resolved due to the limited sampling rate of the data acquisition system.
Once the diode turns on, the voltage is immediately reduced as the resistance of the diode is much smaller than that of the now resistive magnet. The voltage drop over the diode is only 2 V. The current I_{coil} in the magnet dies away in less than a second as can be seen from the fast drop of the magnetic field. As long as the power supply is active, it keeps the total current I_{tot} up, which is now bypassed through the diode. It is important to shut off the power supply as soon as possible. The heat input from the quench evaporates large amounts of helium, and the diodes might not be covered with liquid helium any more. A lack of cooling bears the risk of destroying the diode by overheating. In this example, the power supply is manually turned off

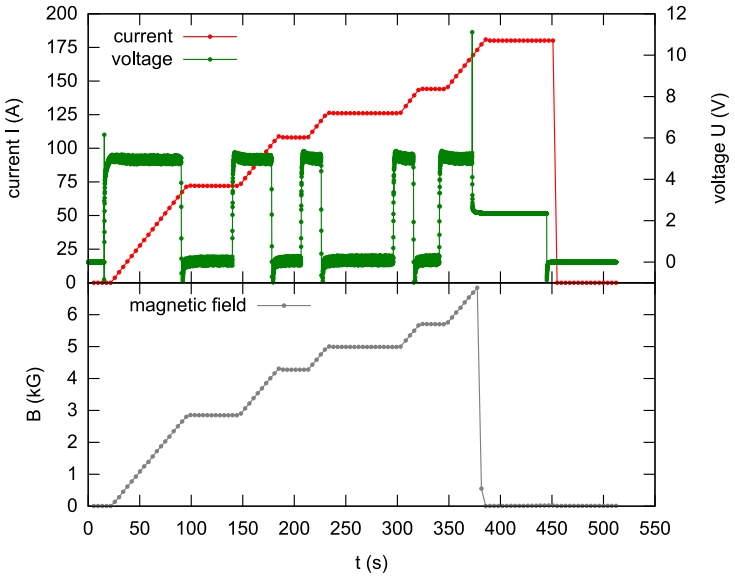

Figure 4.6.: Quench event at $I = 180\,\mathrm{A}$. Top: current and voltage versus time. Bottom: magnetic field versus time. For details see the text.

at $t \approx 450\,\mathrm{s}$. The sudden increase of the voltage can be used to detect a quench right after it happens and to trigger safety measures like turning off the power supply (see also 6.1.1).

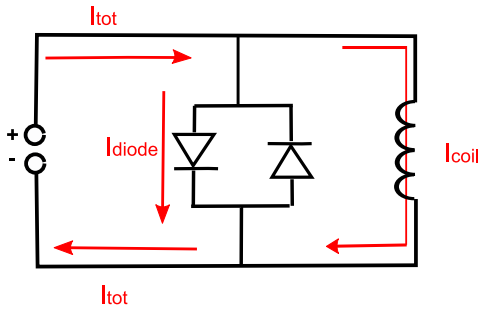

Figure 4.7.: Circuit in case of break-through of the diodes.

4.4.2. Ramping

Magnet characteristics Up to a reliable operating current of 120 A the nominal ramping speed has been checked. The design value of 2.6 A/s was reached at these low currents. The ramping speed up to a voltage of 15 V is depicted in figure 4.8. As can be seen in figure 4.9, there exists an overshoot when reaching the final current. The transient oscillation needs several seconds to settle down. To determine the ramp rate, the time when the current reaches the final current the first time has been used. The error for this time has been conservatively estimated to be 1 s.

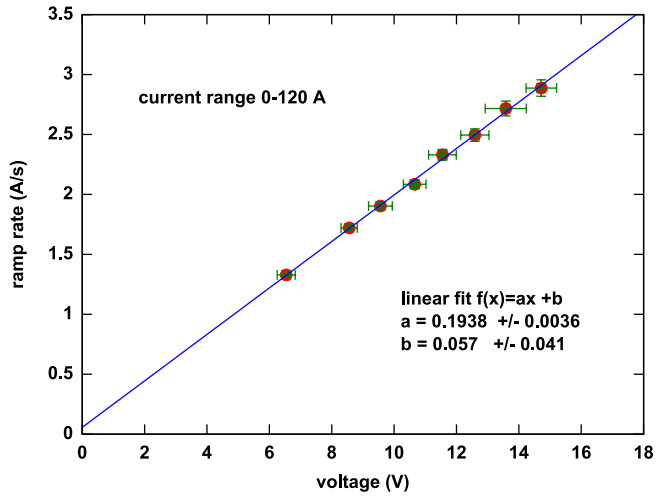

Figure 4.8.: Ramping speed as a function of the applied voltage.

From the voltage and the corresponding ramp rate the inductance L of the magnet can be estimated using the law of induction:

$$L = U/\frac{dI}{dt}.$$

A linear fit to the data in figure 4.8 gives an inductance of 5.15 ± 0.10 H. This value agrees with the inductance $L = 5.4$ H estimated in appendix A but disagrees with the specifications of Scientific Magnetics (4.6 H or 3.3 H; cf. table 4.1).

Circuit characteristics The ramping speed is not only limited by the capability of the magnet, but also the power supply needs to provide a voltage large enough. With the XPR power supply a voltage of only 20 V is available, further reduced by the 5 V-drop at the dump resistors. With the Danfysik power supply it is in principle possible to apply voltages up to 100 V. However, the protection diodes parallel to the magnet have a forward voltage of $U_f \approx 16$ V, and hence the magnet cannot be ramped faster than this implied limit of 3.1 A/s. When a voltage $U > U_f$ is existent, the protection diodes are triggered and a second circuit parallel to the magnet opens (cf. figure 4.7). Current sharing between the magnet circuit and the diode circuit will be the consequence. This case is depicted in figure 4.10. The current I_{tot} in the outer circuit is logged, which is the sum of both parallel circuits, the magnet part and the diode part. Two successive ramp cycles are presented. In the first ramp cycle the full voltage of ≈ 8 V that is applied is

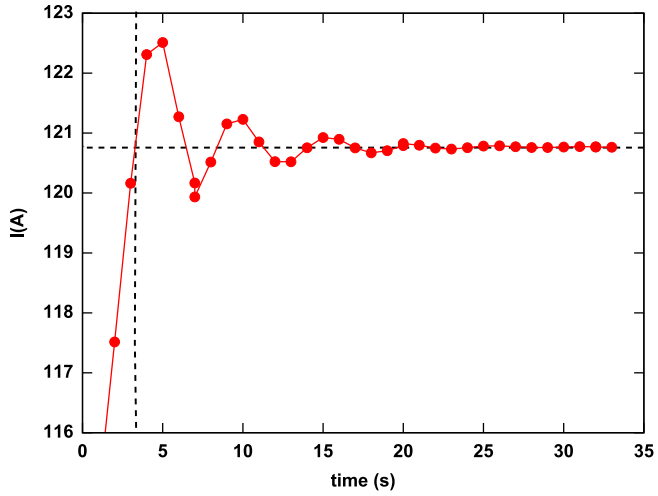

Figure 4.9.: Transient oscillation of the magnet current when ramping to a final value. The data points are connected by straight lines to guide the eye. For extraction of the ramp rate the time when the actual current first reaches the final current value has been used. This is indicated by the black dashed lines.

used to ramp the magnet with 1.6 A/s.[12] The current and the magnetic field reach their maxima at the same time. In the second ramp cycle, a higher ramping speed of 2 A/s has been set, thus a higher voltage of 10 V is initially applied to the magnet. Compared to the current in the outer circuit I_{tot} the magnetic field rises much slower with a rate corresponding to only 0.56 A/s and reaches its maximum 140 s later. This is clear evidence for current sharing between the diode and the magnet circuit. The fact that the break-through of the diode occurs already at 10 V instead of the 16 V specified, points to a malfunction of the diode. As ramping with up to 15 V with both polarities has been possible before, the failure must have occurred at some point during training. Change of the current direction loads the protection diode of the other orientation, and ramping with higher voltage is again possible. Most probable, the diodes have been damaged by overheating due to a a lack of cooling shortly after a quench.

[12] The monitor output voltage in figure 4.10 shows a faulty reading due to high frequency common-mode voltages across some isolation amplifiers on the mainboard of the power supply. [Nie11] The output voltage of the power supply is expected to be constant despite a slight increase to compensate the voltage drop at the resistive parts of the leads (cf. figure 4.6). This bug could later be repaired by installing ceramic capacitors parallel to the amplifiers.

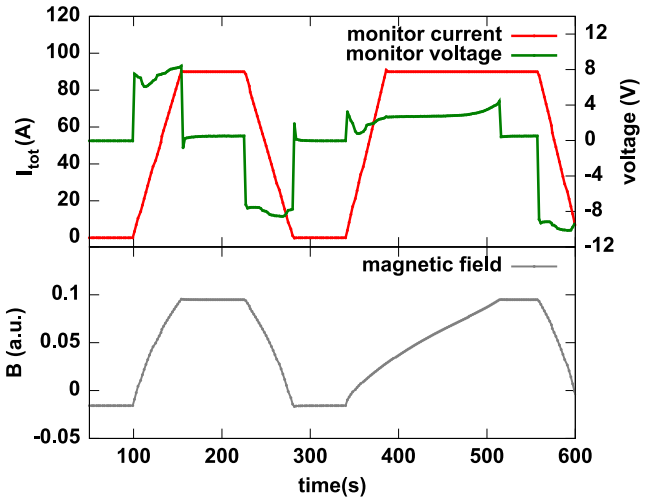

Figure 4.10.: Current sharing on diode break-through. Current and voltage monitored by the Danfysik power supply, magnetic field measured by hall sensors in the cryostat. For explanation see the text.

4.4.3. Reason of magnet failure

The combination of large current and high magnetic flux can drive a superconductor into its normal conducting phase. However, as can be seen in figure 4.11, this is not the reason of the poor performance of the prototype. The current value reached is far below the wire capabilities. According to Scientific Magnetics, a design failure in the interface of the coils to its support

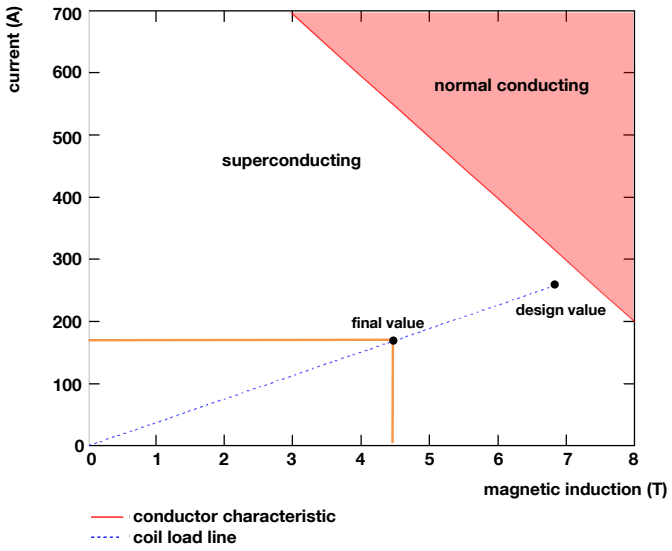

Figure 4.11.: Capabilities of the test magnets superconducting wire. The operating value is far from the limit. [Mil08]

structure is responsible for the low ultimate current. In figure 4.12 a sectional sketch of the coils is presented together with the results of finite-element calculations performed by Scientific Magnetics on the forces acting on the structure. [Mil08] For electrical insulation a G10 epoxy glass composite sheet is glued between the support structure and the coils. During cool down, the large difference in the thermal expansion coefficients (cf. figure 4.13) of the materials, especially aluminum and NbTi, leads to enormous stress (up to 200 MPa) on this sheet. Energizing the magnet leads to additional load; The shear strength of G10 even at room-temperature is only in the order of 131 MPa.[13] Thus, it cannot stand the resulting large shear stress and cracks. Sudden relief of the tension when the G10 sheet breaks leads to a motion of the coil provoking a quench.

Therefore, Scientific Magnetics proposed to build the support structure from stainless steel, which is stiffer and has a more favorable thermal expansion coefficient compared to aluminum. Additionally, instead of bonding the coil to the support structure via the insulation sheet, according to their approach, it is favored to have a *free-floating* mounting of the coils with a low friction surface between the coil and its support. [Mil08] The co-operation with the company has been stopped at this point.

[13] G10 FR4 Material Specification Technical Data Sheet, JJ ORLY, Inc.

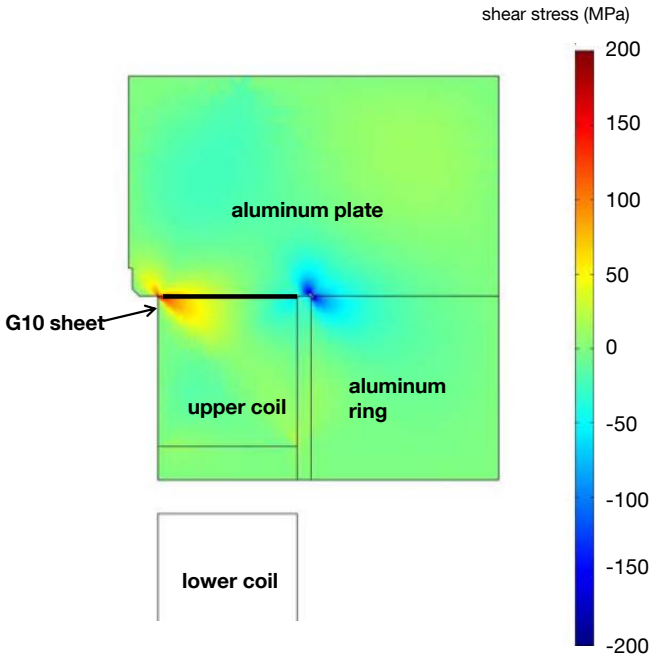

Figure 4.12.: Sectional view of the test magnet: shear stresses resulting from cool down and energizing of the magnet. [Mil08]

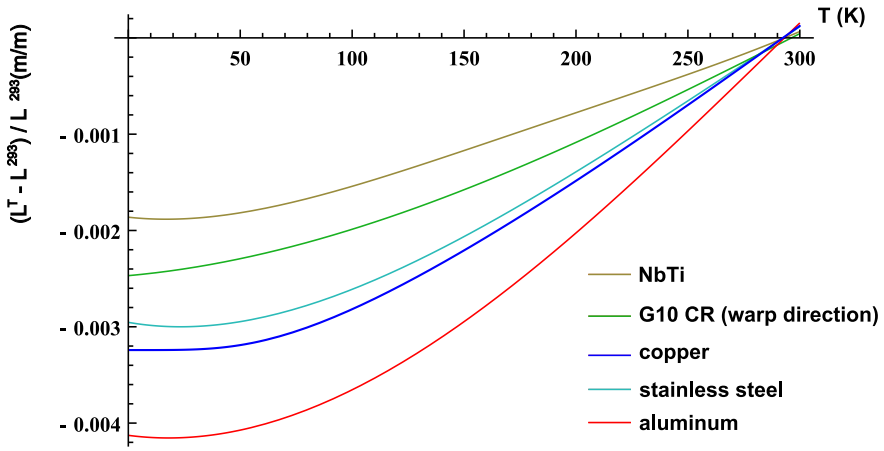

Figure 4.13.: Integrated linear thermal expansion $\Delta L/L$ from room temperature down to temperature T. The coil is made of copper and NbTi, the support structure of aluminum. [M+00]

5. CoTEx - Mapping of the magnetic field

In PENeLOPE the UCN are stored magnetically to avoid losses due to collisions with the walls of the trap (cf. chapter 3). In figure 5.1 the equipotential lines of the PENeLOPE trap are depicted. Towards the cryostat wall the retarding potential for the neutrons gets higher, and the larger the neutron energy the closer they get to the wall. The equipotential line of the envisaged trap

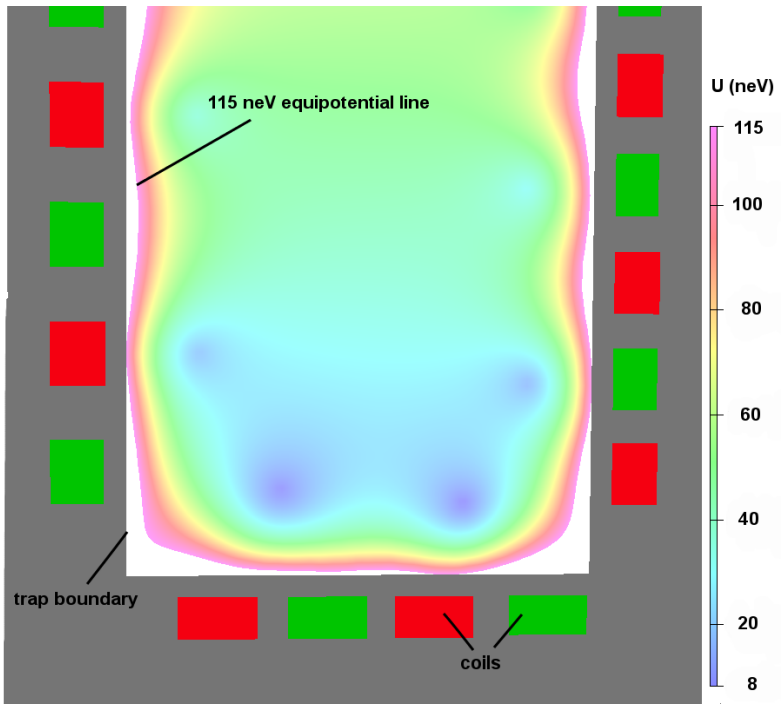

Figure 5.1.: Combined magneto-gravitational potential in the lower part of the PENeLOPE cryostat.

potential of 115 neV[14] is designed to have a distance from the cryostat wall of at least 5 mm to have space for further installations like electrodes for the proton extraction potential or neutron reflecting coatings. Especially in the lower part of the trap this equipotential line is getting very close to the storage volume boundary. Thus, the storage of the UCN is especially sensitive to the near field close to the coils, whereas the global shape of the magnetic field is only important for the proton extraction efficiency (see chapter 3). Although the magnetic field can be calculated precisely with finite element programs like OPERA[15], the coils cannot be constructed exactly according to the geometry in the simulation software. For example, when winding up the coil

[14] The energy is defined with respect to the bottom of the trap.
[15] Vectorfields Opera-3d - electromagnetic design in three dimensions.

in several layers, a crossing of the superconducting wire is inevitable at the transition from one layer to the next (see figure 5.2). This crossing occurs always roughly at the same position at each layer so that the deviation adds up. In figure 5.3 the resulting bulge for a prototype of

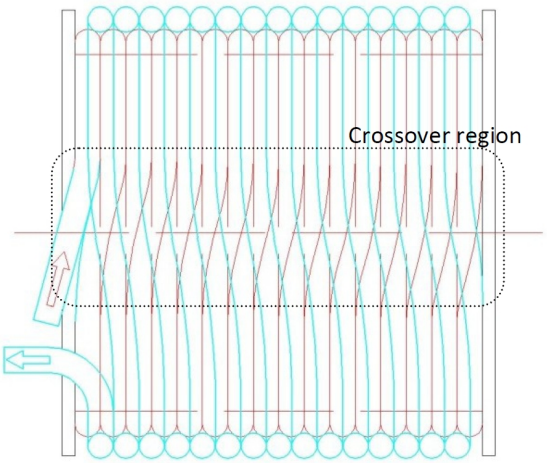

Figure 5.2.: Schematic of the wire crossing at the transition between two layers. [BS11]

the innermost base coil built by Babcock Noell (cf. chapter 6) is depicted. The figure shows the deviation from the ideal circumference at the radius $R = 251\,\text{mm}$. The deviation is up to 3 mm; 76% of the coil are within a tolerance of 0.3 mm. The non-ideal course of the wire at the bulge leads to an asymmetric azimuthal field component. This additional component adds to the azimuthal field created by the central current to fill up zero-field regions and thus suppress spin-flip (cf. chapter 3). Unfavorable constellations might lead to the generation of new zero-field regions. To estimate the impact on the PENeLOPE storage properties a deformation of the solenoids has been simulated for the PENeLOPE trap; [Sch11b] In figure 5.4, a critical region of low magnetic field is exemplified.[16] An overlap of those field components, as in the left part, can create zero-field points; on the right, the central current is large enough to repress zero-field regions. Spin-precession simulations of UCN confined to the critical region show that a minimum field larger than 5 mT has to be guaranteed to keep the spin flip probability at a negligible level. As a consequence, the deformation of every solenoid for PENeLOPE has to be measured and bumps have to be aligned accordingly during assembly of the cryostat. Additionally, the mapping of the magnetic field will be mandatory in the PENeLOPE setup to check the agreement of the magnetic field with calculations and whether the requirements on the magnetic field are met.
Magnetic field mapping has been tested using the existing CoTEx cryostat with the prototype coil from Scientific Magnetics.

[16] To clearly visualize the effect, all base coils have been deformed by 5%, although the measurements on the prototype suggest only a deformation $< 1.3\%$.

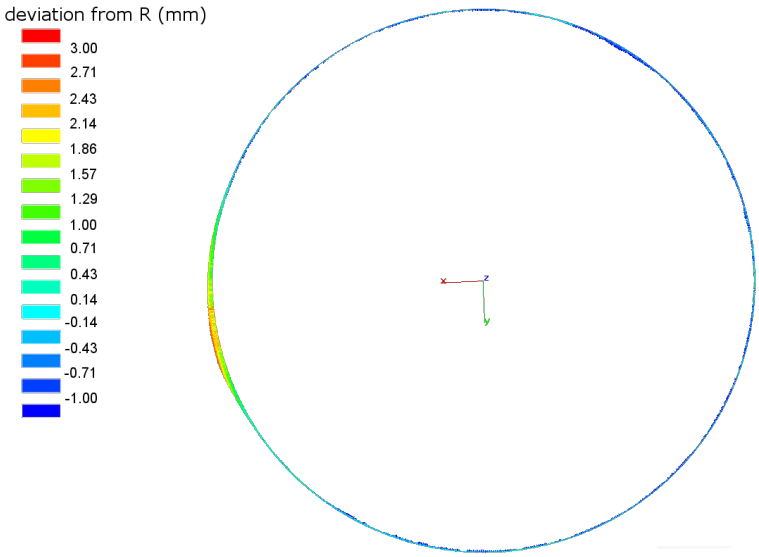

Figure 5.3.: Measured deformation of the inner base coil prototype from Babcock Noel. The coil is shown in top view. The deviation from $R = 251\,\mathrm{mm}$ is given color-coded. [Ste11a]

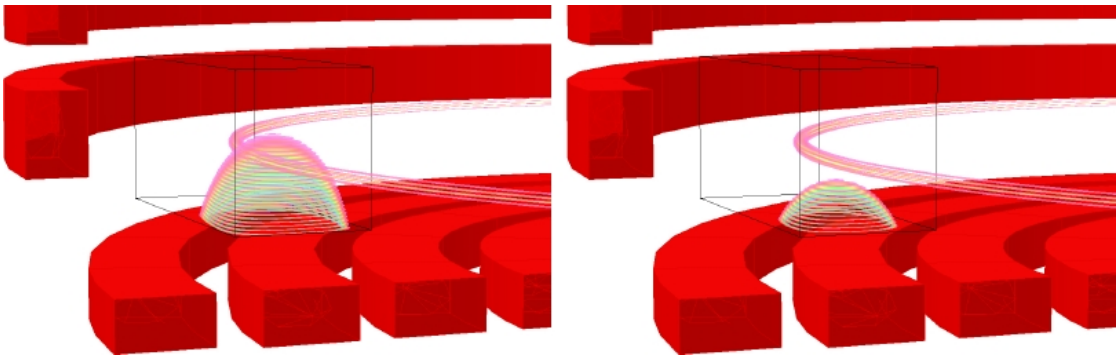

Figure 5.4.: Effect of coil deformation on zero-field regions: in red the solenoids are depicted; the purple annular lines depict zero points in radial and axial field components whereas the colored surfaces are zero points in the azimuthal field component. These two regions must not overlap to avoid zero total magnetic field. On the left the central current is 5 kA, on the right 12.5 kA.

5.1. Experimental setup

Hardware The ring-shaped helium vessel of the CoTEX setup allows helium-free access to the inner region surrounded by the prototype coils and thus mapping of the magnetic field. On top of the CoTEx vacuum tank a linear XYZ-translation stage has been installed. Via a swivel joint and a wobble stick it guides three cryogenic Hall sensors mounted at the end of a long extension rod to scan the magnetic field inside the bore of the helium vessel (cf. figure 5.5).

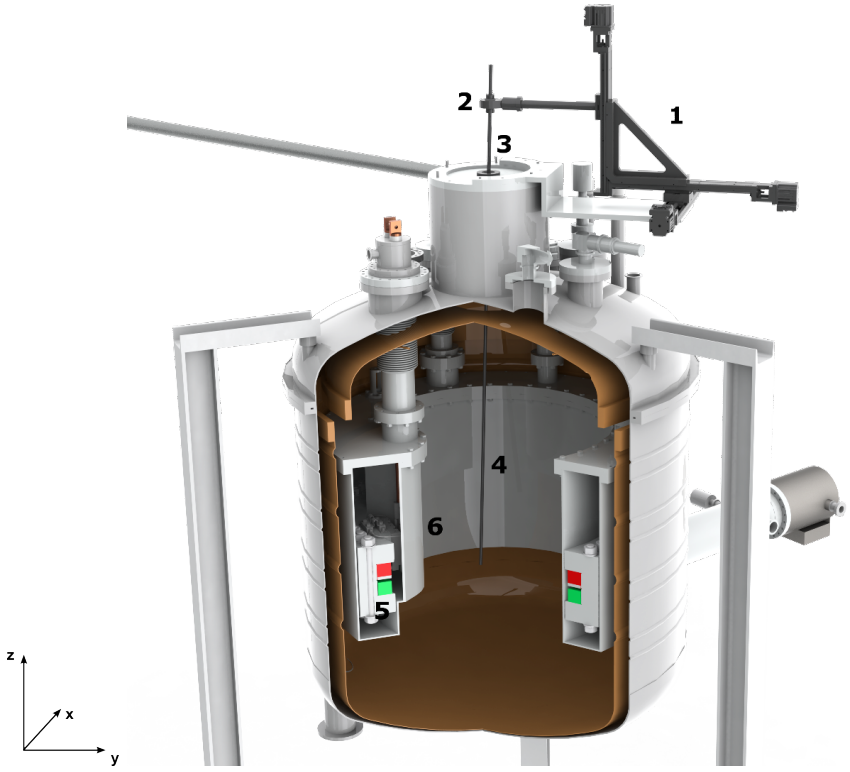

Figure 5.5.: Sectional view of the CoTEx cryostat extended by a device to scan the magnetic field: 1) linear XYZ stage, 2) swivel joint, 3) wobble stick, 4) extension rod, 5) coils, 6) bulge for the current leads.

The wobble stick allows a vacuum-tight transfer of the movement into the cryostat (cf. figure 5.6): A tube is connected to a bellow fixed in a rotation point, flexible in all angular directions up to an angle of 14°. A short rod inside the tube can be moved up and down, guided by a magnetic collar from outside the tube. Thus, movement in all three dimensions is transferred at once. A long extension rod is connected to the end of the wobble stick to reach down into the plane of the magnet. The translation stage is attached to the magnetic collar of the wobble stick via a cardanic swivel joint.
The central rotational symmetry axis of the magnet is parallel to the z-axis of the translation

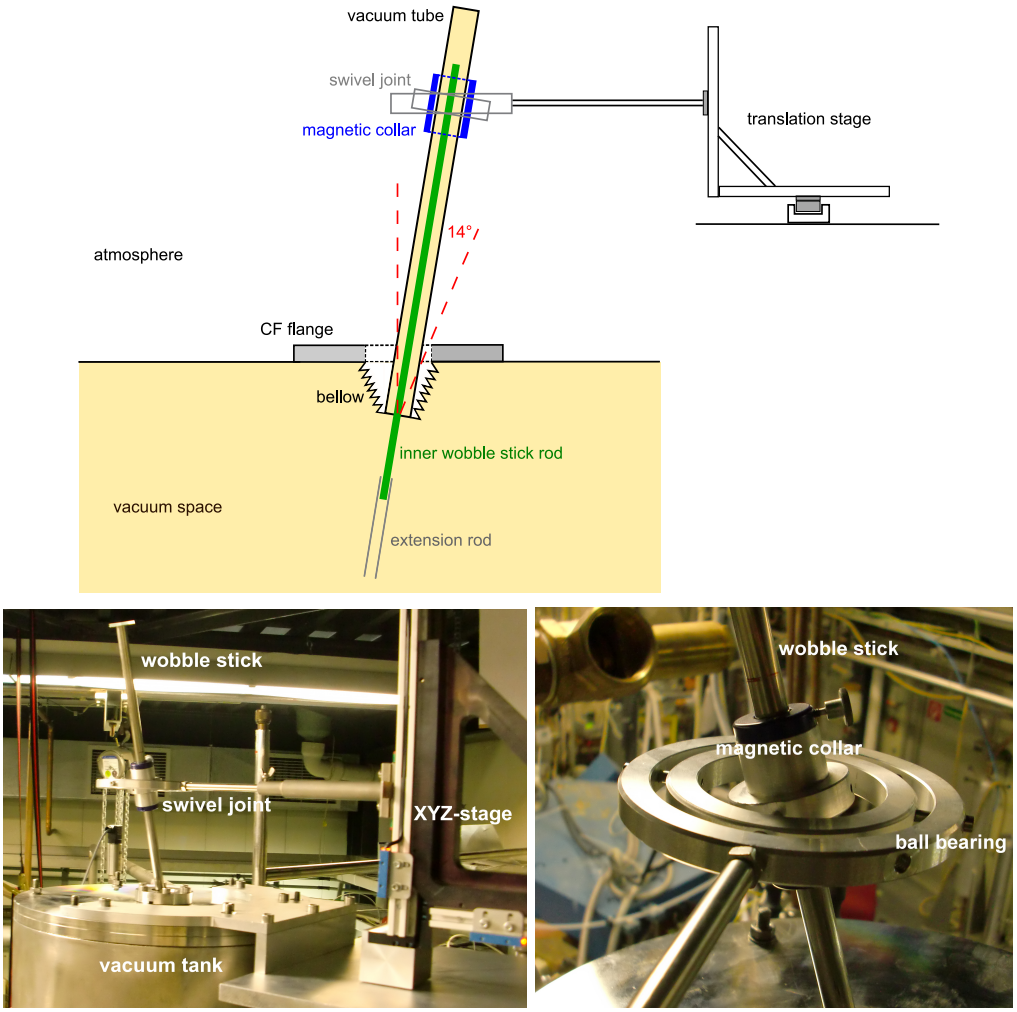

Figure 5.6.: Top: Schematic of the wobble stick - translation stage system. The sketch is not to scale. Bottom left: Pictures of the field mapping assembly with wobble stick, swivel joint and linear XYZ stage. Bottom right: a close-up view of the cardanic swivel joint.

stage and coincides with the wobble stick rod in its initial position.[17]
This special geometry implies that every movement is transferred over a rotation point. The sensor head is tilted as soon as it moves out of the central position straight below the rotation center. However, there is no rotation around the axis of the extension rod, the z-axis. This vertical z-axis together with the x- and y-axis of the translation stage define the laboratory frame. Magnetic parts in the setup have to be avoided. The extension rod is made of carbon-fiber reinforced plastics (CFRP) benefiting from its large stiffness, light weight and low thermal expansion coefficient. The sensor holder itself and the swivel joint are made of aluminum. The wobble stick consist mainly of stainless steel, but there is a magnetic collar. The translation stage has magnetic parts, as well. However, due to the large gradient of the magnetic field, at the cryostat top it has decreased below 1.1 mT at a magnet current of 90 A. Most of the measurements in section 5.5 were performed at a coil current of 70 A. Thus, no false effects from magnetic forces are expected during the measurements.

Software The translation stage is controlled with the commercial program JenCNC, the cryogenic Hall sensors are read out with a gaussmeter from Lakeshore. As there is no interface between these two programs, an indirect solution was implemented to combine the position of the translation stage, i.e. of the Hall probes, with the magnetic field measured at this position (see figure 5.7): With the JenCNC program a logical bit is set at the COM-port of one of the step motors as soon as a measuring position has been reached. This flag is watched continuously via a RedLab ADC from Meilhaus by a Labview program and triggers the Labview program to read the values of the Hall sensors from the gaussmeter which are than exported to a chart. In the end, the file with the Hall sensor values is joined with another file listing the positions of the XYZ stage.
The XYZ stage stops at every measuring position for a moment, and the long extension rod starts swinging. This effect is minimized by choosing a very small scan velocity and a pause of 1 s before the translation stage moves to the next position. This pause is also necessary as the Labview program needs time to register whether the measuring bit is set. Missing a bit corrupts the file storing the magnetic field values, which cannot be joined with the position file anymore, and the complete scan is obsolete. With a pause of only 0.5 s the Labview program misses seven out of 10000 measuring flags, whereas none of 10000 is missed with a pause of 1 s.
However, the low velocity and the long pause leads to long measuring times. E.g., a full circular scan at a fixed radius of ≈ 350 mm and measuring every 10 mm along the circumference takes roughly three hours.

Scan geometry and path calculation With a self-written C++ program the path to scan a defined section in the measuring region is calculated. The program creates a command file readable by the JenCNC software as well as a table file listing the positions of the scanning path. The program checks that only allowed positions are set. This assures that the sensor holder does not run into any structure of the cryostat, as a breaking of the wobble stick would lead to a sudden breakdown of the insulation vacuum. Restrictions are given by

- the maximum possible inclination angle of the wobble stick,
- the maximum possible travel of the wobble stick and

[17] The alignment is not perfect. As will be pointed out in section 5.2 there is an offset of a few mm between the center of the coil and the center of the measuring setup i.e. the rotation point of the wobble stick. The coil is also slightly tilted with respect to the XYZ-translation stage. Thus, the z-axis of the measuring system does not exactly coincide with the rotational axes of the magnet.

- the inner radius of the cryostat, respecting that the tank is not circularly symmetric, but has a bulge, where the current leads are connected to the coils (cf. figure 5.5).

Scan geometries implemented in the C++ program are - with respect to the coil plane - horizontal (xy-plane) and vertical (rz-plane) scans (cf. figure C.1). Depending on the chosen geometry, the user defines boundary parameters of the area to be scanned like the radial range, position/range in height, angular position/range and the point distance of the measuring grid. From these parameters the program automatically calculates the positions of the measuring points as well as the corresponding coordinates the XYZ stage has to move to and generates the JenCNC command file. A detailed description of the algorithm to calculate the coordinates from the measuring positions is given in appendix C.

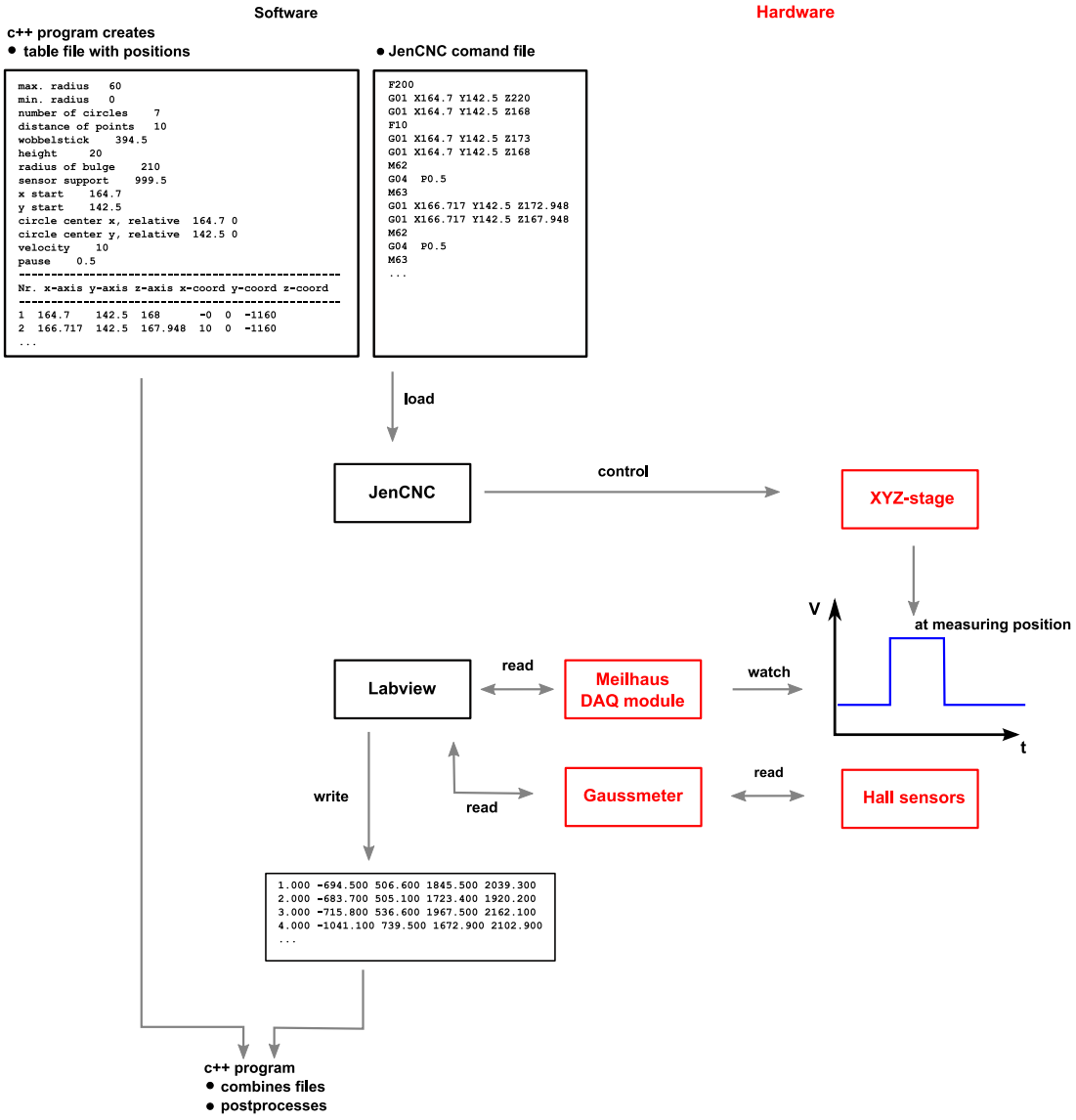

Figure 5.7.: Flow chart of a magnetic field scan. Details are given in the text.

5.2. Limitations of the measuring setup

Besides many advantages of the chosen system - all actuators are outside the cryostat and still only one feed through is necessary, the movement is observable and thus checkable from the outside - the combination of the translation stage with a swivel proved to be problematic. The interplay of many parts imply the existence of mechanical tolerances. Any uncontrolled movement or displacement on top of the tank is enhanced by the long level arm of the extension rod ($l \approx 1200\,\mathrm{mm}$) and leads to large effects on the sensor position (c.f. figure 5.8). Several geometrical constants, which can only be measured with a certain accuracy, are used in the algorithm to calculate position and tilt of the Hall probes. Many measures have been taken to improve or determine the uncertainties. In the following, the main effects are listed and discussed. They are summarized at the end in table 5.1.

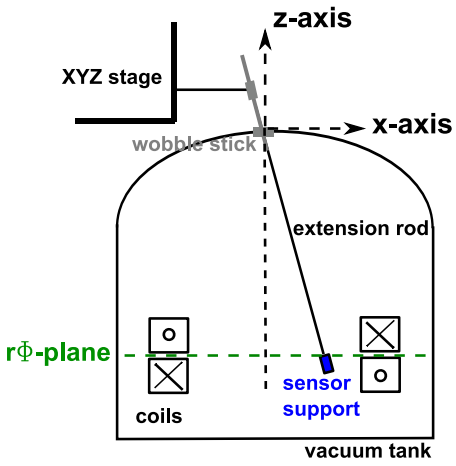

Figure 5.8.: Sketch of the measurement setup in side view (zx-plane).

Absolute precision

- The absolute vertical alignment of the z-axis of the setup was checked with the help of a laser beam: The beam of a small laser, installed at the Hall ceiling, points to a mirror attached to the top of the wobble stick (see left side of figure 5.9). The point on the ceiling indicated by the reflected laser beam marks the orientation of the wobble stick. If the wobble stick is vertically aligned and parallel to the z-axis of the translation stage the laser spot should not move, when the XYZ stage, which is connected with the wobble stick, moves up and down along the z-axis. Considering the size of the spot itself, any shifts down to 0.7 mm are visible. This corresponds to an angular deviation from the vertical axis of 0.09° and thus a deviance of the sensor head from the central position in the coil plane by 1.5 mm.
- The accurate orientation of the Hall sensors with respect to the axis of the laboratory frame, given by the axes of the XYZ stage, is much more crucial: When calculating the magnetic field in the laboratory frame from the measured projections, exact alignment is assumed. Any oblique orientation would imply that a wrong value for the magnetic field in the laboratory frame is derived from the measured projections. A conservative error

estimation gives an angular deviation smaller than 0.17° for this alignment (cf. right side figure 5.9).

- The magnet is orientated to the linear XYZ stage such that the wobble stick with the extension rod in its home position coincides with the rotation axis of the magnet, and thus the xy-plane of the translation stage is parallel to the rϕ-plane of the magnet (figure 5.8). The precise alignment of the magnet to the linear XYZ stage is hard to realize in this setup, but of minor importance, as any misalignment of the coils like a transversal offset and a tilt around the x- and y-axes can be extracted directly from measurements (compare sections 5.3 and 5.5).

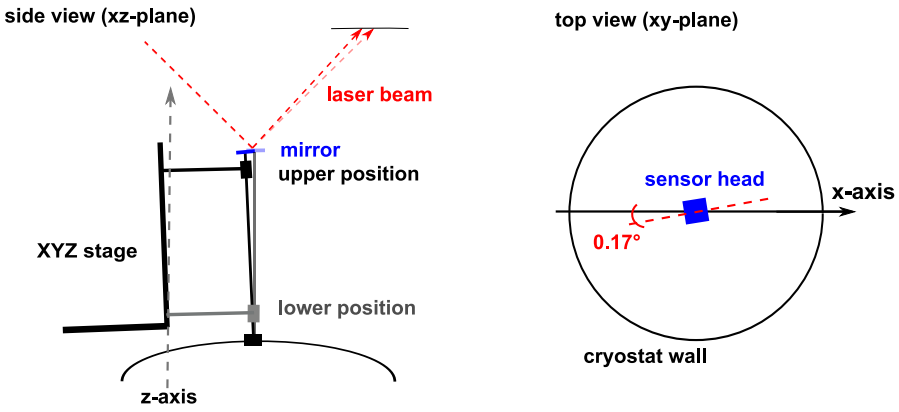

Figure 5.9.: Left: A tilt of the z-axis of the stage-wobble stick system can be revealed with the help of a laser. Right: Alignment of the sensor head.

- The extension rod is a tube made of CFRP with a diameter of 8 mm and a wall thickness of 1 mm, very light-weight and extremely stiff. A bending of the bar due to the torque exerted when moving the sensor head to any position out of the center is negligible, as the sensor head weighs only 5.2 g. However, due to the manufacturing process the tube itself cannot be produced perfectly straight. The rod installed in the setup deviates over the length of 975 mm from a straight line by ≈ 0.1 mm - corresponding to a bending radius of 1.1 km. This implies a tilt of the sensor head by only 0.05°.

- Using CFRP for the extension rod also has the advantage of minmizing effects due to thermal contraction. The thermal expansion coefficient of CFRP is in the order of $10^{-6}\,\mathrm{K}^{-1}$. During operation the sensor head settles at a temperature of ≈ 120 K, whereas the wobble stick rod at the top stays at room temperature. Assuming in the worst case a temperature of ≈ 120 K for the complete rod, the thermal shrinking makes up only $10^{-6}\,\mathrm{K}^{-1} \cdot 170\,\mathrm{K} \cdot 1\,\mathrm{m} \approx 0.2$ mm.

- The accuracy of the XYZ stage is specified with 10 μm per axis. However, it is a composite system consisting of three individual linear units (see figure 5.10). The x-axis unit forms the base of the system. Attached to its carrier is the y-axis unit together with the z-axis unit. Thus, most of the weight of the translation stage (in the order of $10 - 15$ kg) is supported just by the carrier of the x-axis unit. When the translation stage moves in y-direction, the

center-of-mass of the upper part shifts by up to 15 cm off the x-axis resulting in a torque on the x-unit carrier. Given the mechanical clearance of the carrier, the top-installation will tilt. To reduce this effect, a support has been installed under the y-axis unit which applies a pretension by means of a spring (cf. figure 5.10). With a micrometer gauge, the tilt has been estimated to be smaller than 0.06° at full extension of the XYZ stage. This corresponds to an inaccuracy of the z-position of the sensor support in the order of 0.2 mm and of the radial position of 1.2 mm. However, when scanning the magnetic field, the translation stage cannot move in the complete range but is limited to a small area around the center, which reduces this effect further.

- Several geometrical constants of the setup, like the length of the extension, occur in the algorithms to calculate the positions and the tilt of the Hall probes. Conservatively estimated, the uncertainties in the knowledge of these values sum up to 2 mm. Appendix C gives more details.

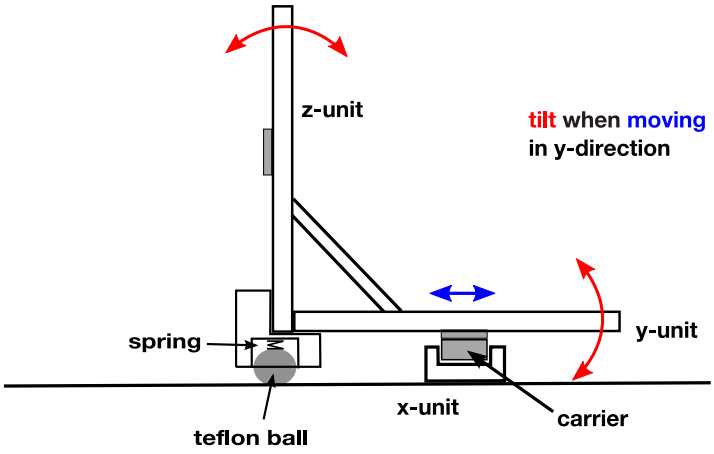

Figure 5.10.: Schematic view of the translation stage distortion. Moving the XYZ stage back and forth (blue arrow) leads to a tilt (red arrow) as a torque is created by shifting the center of mass of the XYZ stage.

Reproducibilty The reproducibility can be checked in several ways. Additionally to using the laser-mirror system at the top of the cryostat, in the same way a mirror was installed at the side of the Hall sensor support. A shift of the position of a laser spot reflected from the mirror reveals deviations larger than 0.05°.
With this method it was shown that going to the same position once from the top moving down the wobble stick and once from the bottom going up differs by up to 4 mm in z-direction. This offset originates from cumulative tolerances in the wobble stick magnetic collar and the connection to the XYZ stage. Thus, in order to maintain reproducibility, all measuring points have to be approached always from the same direction. This is realized in two ways: first of all, before going to the actual measuring point, a position 5 mm above the scan point is taken. Secondly, the path to scan the measuring area is chosen such that points with larger z-value of the XYZ stage are piloted first.
In anticipation of the measurements presented in section 5.5, in figure 5.11 the consequence of this tolerance for the field mapping is exemplified. The same path has been scanned going back and forth four times. Depicted in red are the magnetic field values measured when going the path in one direction and in green for the opposite direction. Between the different directions, a discrepancy as large as 40% shows up, whereas the repetitively measured values going in the same direction coincide nicely - for both directions, respectively. This is a clear evidence for a tolerance that creates a reproducible shift of the sensor position. Another issue is the

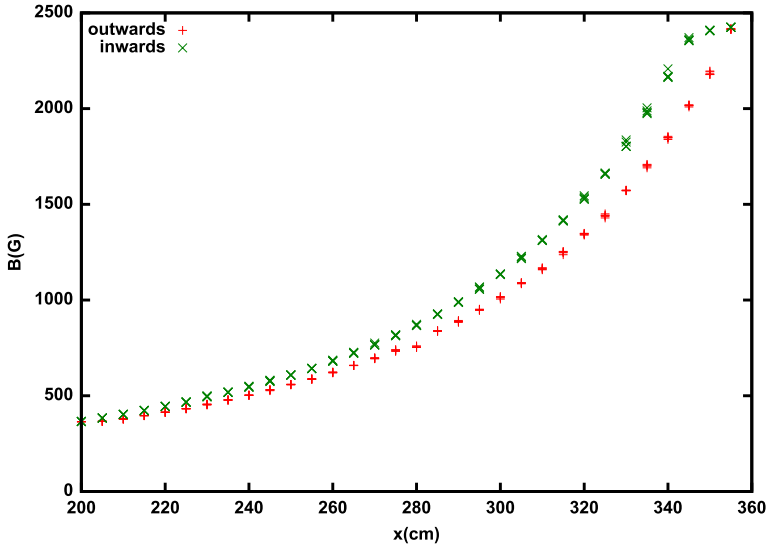

Figure 5.11.: Impact of wobble stick tolerances on magnetic field measurement without countermeasures. Four times the same path has been scanned forward and backward. See also figure 5.19 in chapter 5.5.

precision of the translation stage itself. To reach the specified precision, the XYZ stage needs to be calibrated when starting the JenCNC program which controls the stage. It moves to a defined home position and later on takes any position relative to this reference point. However, as this homing position is outside the geometrically allowed range when the wobble stick is attached, the latter has to be disconnected for calibration. Special care has to be taken that

reattachment does not lead to position changes due to any tolerances. An easy to open and close joint between the translation stage and the wobble stick has been installed which guarantees position reproducibility by means of a stop (cf. figure 5.12). It was proven that going along

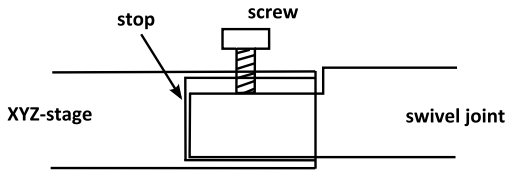

Figure 5.12.: Sketch of the connection between the swivel joint and the linear XYZ stage. See also figure 5.6.

arbitrary paths and performing calibration including the detachment and re-attachment of the wobble stick does not lead to any deviations within the measuring accuracy of the described methods.

item	**uncertainty in position of sensor head (tilt in degree, offset in mm in central position)**
vertical alignment of the wobble stick to the z-axis of the XYZ stage	$< 0.09°$, < 1.5 mm in r
orientation of sensor head w.r.t. the laboratory frame	$< 0.17°$
bending of the extension rod	$< 0.05°$
thermal contraction of the extension rod	< 0.2 mm in z
tolerance of the XYZ stage	$< 0.06°$,< 1.2 mm in r, < 0.2 mm in z
geometrical constants of setup	< 2 mm in z
reproducibility (including calibration procedure)	$< 0.05°$

Table 5.1.: List of position deviations and tolerances in the setup to map the magnetic field.

5.3. Coil position and alignment

The absolute position and orientation of the magnet with respect to the laboratory frame given by the wobble stick and the translation stage can be measured mechanically or by scanning the magnetic field. The latter will be discussed in section 5.5.
Mechanically, these values can be determined by going with the sensor head once around a circle with a fixed radius as close as possible to the coils and measure the distance in radial and in z-direction to the magnet.
The measurements of the radial distance are depicted in figure 5.13. The sensor position as well as four individual measurements of the magnet are depicted for the height h=0.[18] To cover a larger range in z-direction, the helium tank was closed, and the distance to the helium vessel wall instead of the magnet has been measured, too. As the magnet is embedded tightly in the helium tank, their center positions correspond roughly. The offset of the coil is (at $h = 0$) 0.30 ± 0.29 mm in x- and 11.2 ± 0.6 mm in y-direction. To extract the tilt of the magnet, the distance from the

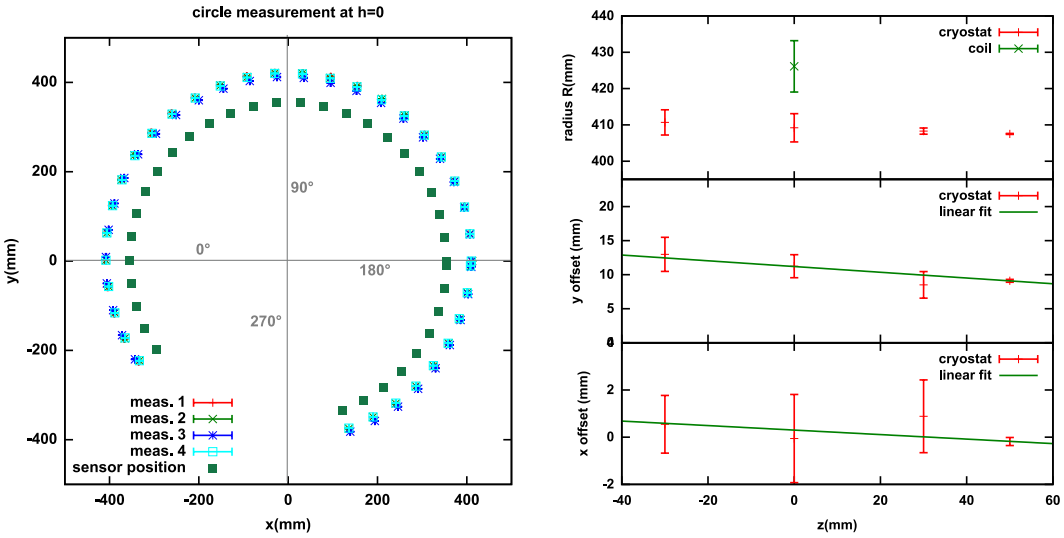

Figure 5.13.: Left: Four exemplary measurements of the coil position at the height h=0. Right: Mean fit results for the radius as well as the x- and y- offsets from the measurements of the distance to the cryostat wall and the coil for several heights.

sensor head to the bottom edge of the magnet has been measured. Results are given in figure 5.14 together with a sinus function fitted to the data. The parameter d gives the orientation of the tilt axis and b the tilt angle α: $\sin(\alpha) = b/r$ with the radius r of the magnet. Thus, the coil is tilted by $\alpha = 0.43° \pm 0.02°$ around an axis at $d/2\pi \cdot 360 = 190.8° \pm 4.0°$, i.e. roughly the x-axis.

5.4. Transformation of measured magnetic field projections

The Hall probes get tilted as soon as a measuring position off the z-axes through the rotation center of the wobble stick is taken. As the tilt depends on the position, different projections of the

[18] The height is defined with respect to the central plane which is assumed to be the middle plane of the coil system. See also C.

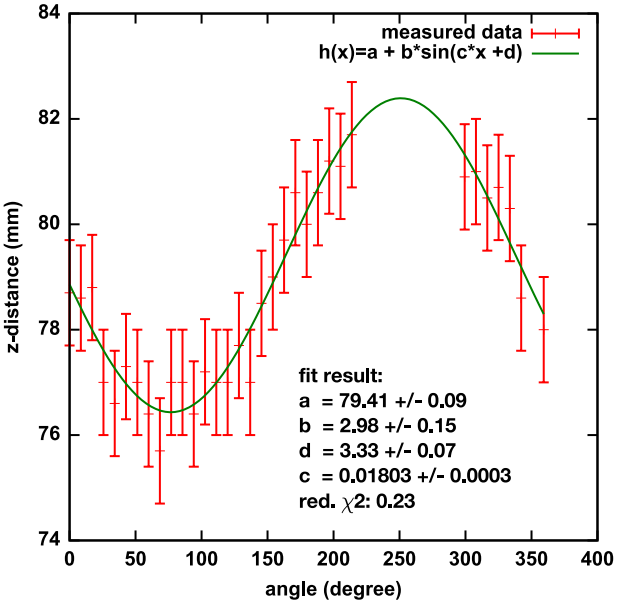

Figure 5.14.: Distance of the sensor head to the bottom edge of the coil. 0° is on the negative x-axis in figure 5.13.

magnetic field are measured at each position. These have to be transformed into the laboratory frame by applying a rotational transformation. In the following considerations, quantities in the laboratory reference frame O, given by the x-,y- and z-axis, are denoted with unprimed symbols. Its origin is located in the rotation center of the wobble stick. Primed symbols are quantities in the rotated coordinate system of the sensor support O' spanned by the unit vectors in x'-,y'- and z'-direction.
Due to the construction of the swivel joint there is a rotation around the x-axis and a rotation around the y-axis but not around the z-axis. The order in which the rotations have to be applied is also given by the swivel joint geometry (cf. figure 5.6): The outer rotation at the swivel joint which is the rotation around the x-axis has to be applied first as it transforms also the rotation axis of the inner part of the swivel joint - the rotation around the y'-axis.
The rotation matrices for a rotation around the x- and the y-axis are

$$R_x = \begin{pmatrix} 1 & 0 & 0 \\ 0 & \cos\alpha & -\sin\alpha \\ 0 & \sin\alpha & \cos\alpha \end{pmatrix}, \; R_y = \begin{pmatrix} \cos\beta & 0 & \sin\beta \\ 0 & 1 & 0 \\ -\sin\beta & 0 & \cos\beta \end{pmatrix}.$$

To transform between the laboratory frame and the reference frame of the tilted sensor head, the product of these matrices is applied to the vector to be transformed:

$$\begin{pmatrix} x' \\ y' \\ z' \end{pmatrix} = \underbrace{R_y \cdot R_x}_{R} \begin{pmatrix} x \\ y \\ z \end{pmatrix}.$$

The rotation angles α and β can be determined from the position of the sensor head i.e. the scan position. Due to the choice of the axes the unit vector in z'-direction, $\hat{z}'$, always points to the center of rotation i.e. the origin of the reference frame. This implies that rotating the unit vector pointing from the origin to the sensor head by R gives the unit vector in z'-direction within the O' coordinate system or in other words rotating the unit vector $\hat{z}'$ by R^{-1} gives the coordinates of this vector in the laboratory frame O:

$$\begin{pmatrix} x \\ y \\ z \end{pmatrix} = R^{-1} \begin{pmatrix} 0 \\ 0 \\ 1 \end{pmatrix} = \begin{pmatrix} -\sin\beta \\ \cos\beta\,\sin\alpha \\ \cos\beta\,\cos\alpha \end{pmatrix}.$$

Hence, the conditional equations for the angles are

$$\tan\alpha = y/z,\ \tan\beta = -x/\sqrt{y^2+z^2}.$$

The magnetic field vector in the reference frame can be calculated from the projections measured in the rotated system of the sensor support by

$$\begin{aligned} \vec{B} &= R^{-1}\cdot\vec{B}'^{\text{meas}} \\ &= B'^{\text{meas}}_{\text{X}}\cdot\hat{x}' + B'^{\text{meas}}_{\text{Y}}\cdot\hat{y}' + B'^{\text{meas}}_{\text{Z}}\cdot\hat{z}'. \end{aligned}$$

Combination of projections in a skew coordinate system. The Hall probes, being mounted on the faces of a cuboid, are placed a few mm apart from each other. Neglecting these offsets would entail combining the magnetic fields measured at different locations. The resulting error is in average about $\approx 7\%$ as will be shown in section 5.6. To avoid this, when scanning the magnetic field, the sensors are positioned at the same point in the laboratory reference frame one after the other. Due to the geometry with the rotation center, this leads to different tilt angles of the sensor head each time one projection is measured. This implies that the magnetic field vector is measured in a skew coordinate system, as the projections of the magnetic field seen by the Hall sensors in their measuring position, respectively, are not perpendicular to each other. Whereas for an orthogonal coordinate system the measured projections can be simply combined and transformed as explained, in a skew coordinate system the measured projections are not the correct coefficients c_x,c_y and c_z to combine the resulting magnetic field vector linearly from the unit vectors in the x',- y'- and z'-direction (see figure 5.15):

$$\begin{aligned} \vec{B} &= c_{\text{X}}\cdot\hat{x}' + c_{\text{Y}}\cdot\hat{y}' + c_{\text{Z}}\cdot\hat{z}' \\ &\neq B'^{\text{meas}}_{\text{X}}\cdot\hat{x}' + B'^{\text{meas}}_{\text{Y}}\cdot\hat{y}' + B'^{\text{meas}}_{\text{Z}}\cdot\hat{z}' \end{aligned}$$

Instead, the correct magnetic field vector is calculated via the intersection of the three planes perpendicular to the skew axes, supported by the vectors given by the measured projections and the unit vectors pointing in the direction of these axes, respectively. The coordinates of the unit vectors $\hat{x}'$,$\hat{y}'$ and $\hat{z}'$ in the laboratory frame O are calculated with the rotation matrix R and the angles α and β derived from the position of the sensor head as described before. Thus, the support vectors for the planes are known and their direction vectors are constructed with the help of the vector product. First, the intersection line between two of the planes e.g. the one perpendicular on the x'-axis and the one on the y'-axis, is calculated, thereafter the piercing point of this line with the remaining plane. All possible combinations are equally good. Thus, one obtains the correct magnetic field vector in the laboratory frame.

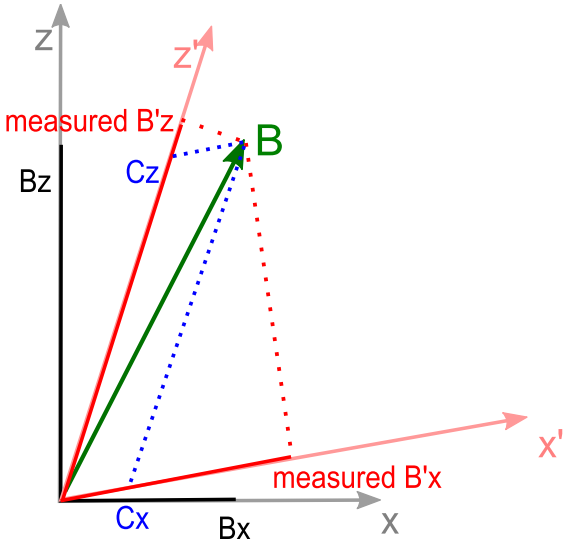

Figure 5.15.: Measured projections (red) of the magnetic field vector $\vec{B}$, coefficients C_i of the linear combination in a skew coordinate system (blue) and projections in the laboratory frame (black). For clarity only two dimensions are depicted.

Algorithm checks To verify that the algorithm calculates the correct magnetic field vector, 10000 random magnetic-field vectors have been generated. These were projected onto x'-,y'- and z'-axes which were created by independent rotations of the laboratory axes by, again, randomly generated angles α and β. Finally, these projections were fed into the reconstruction algorithm and its result compared to the initial B-vector. In all but 40 cases the reconstructed vector equals the initial vector exactly. Looking at the cases the reconstruction fails, no suspicious constellations could be found. The rotation angles of the axes and the initial B-vectors are evenly distributed as well as the orientation of the randomly generated vectors with respect to each other. Most likely, the failure is due to numerical precision problems, occurring, when extremely large and small numbers have to be handled in the algorithm.

5.5. Magnetic field measurements

5.5.1. Hall sensors

A stable and reliable operation of the Hall probes is mandatory for the magnetic field mapping as the sensors are inside the cryostat and cannot be exchanged without warming up and opening the cryostat. In addition, depending on the size of the mapped area, a scan takes several hours. Any drifts or fluctuations of the sensor values have to be small compared to the aspired precision. According to the specifications, the error of the sensors itself is below 1% in the range up to 3000 G (= 0.3 T). An individual calibration curve as well as an error estimate is given for each probe (cf. appendix D).
Figure 5.16 shows the Hall sensor values logged over 40 hours as well as the temperature measured at the setup. The drift within this time period is smaller than 0.4 G, the short term fluctuations of the sensors are ≈ 0.05 G. There is clearly a temperature sensitivity especially of the z-sensor.

The effect in figure 5.16 is mainly from the cable connecting the sensor with the controller whose resistance changes with temperature. To minimize this effect the cable has to be kept as short as possible - in this case it is about 4 m from the vacuum feed through to the controller. The

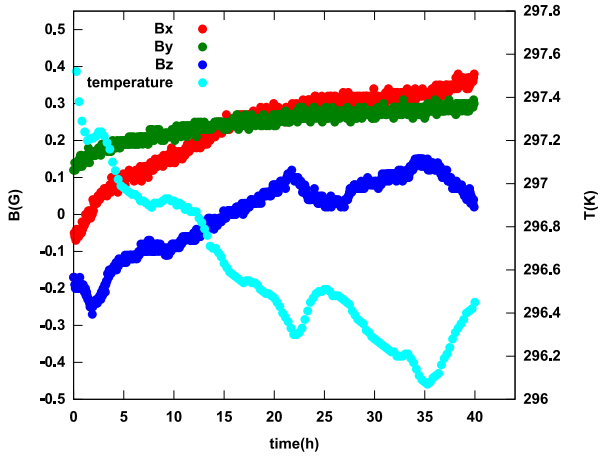

Figure 5.16.: Long-term stability of Hall probes.

temperature dependence of the resistance of the Hall sensors itself affects of course the readings as well. In figure 5.17 the drifts of the values of the x-, y- and z-sensor during cool down of the cryostat are depicted. Reaching the final operation conditions in the cryostat, the sensors stabilize at a temperature of $\approx 120K$. Hence, the drift of the values can be treated as a constant offset and corrected for.

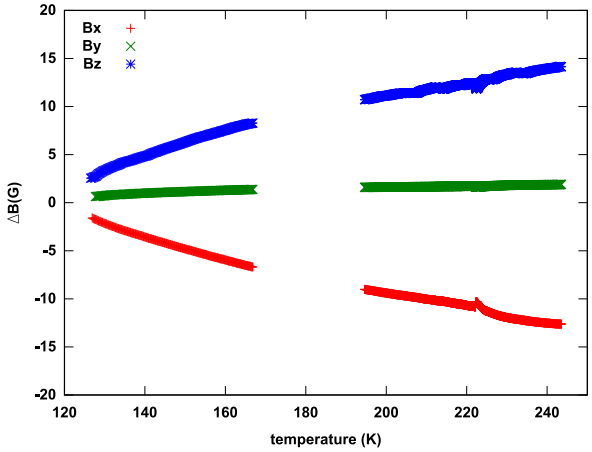

Figure 5.17.: Drift ΔB of Hall probes due to temperature. In the range between $T \approx 167\,\mathrm{K}$ and $T \approx 196\,\mathrm{K}$ the data has not been logged.

Hysteresis effects Any magnetization, e.g. of the sensor support, would falsify the measured field. As the field scans are done at constant coil current, a magnetization of the cryostat tank would just impose a constant offset. However, a magnetizable sensor support would distort the measured magnetic field when moving from high-field to low-field regions while scanning the gradient magnetic field. To exclude this effect, non-magnetic materials have been used for sensor support and extension rod, as mentioned before. In figure 5.18 each sensor has been placed at a position with a high magnetic flux in the direction it measures, and the magnet has been ramped up and down. The deviation from linearity is smaller than 0.4%

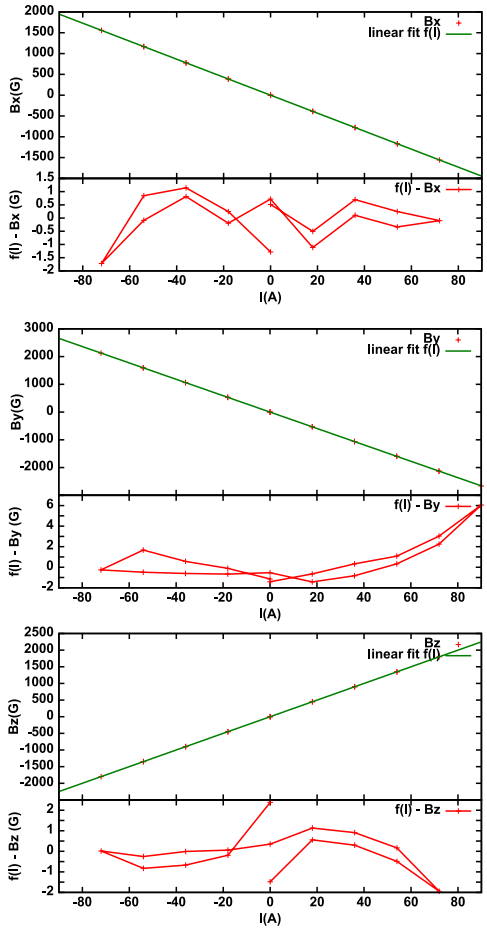

Figure 5.18.: Magnetic field Bx, By and Bz measured at a fixed position while the current is ramped between -80 A and +80 A. Whereas the upper parts of the diagrams show the measured data, the lower parts give the residuals, i.e. the differences between the measured values and a linear curve fitted to the data points. To visualize the sequence of the measuring points, they are connected with straight lines.

5.5.2. Reproducibility

To check the influence of setup tolerances (cf. chapter 5.2) on the magnetic field measurements, an arbitrary path has been scanned several times. As illustrated in 5.19 the relative deviation of the individual measurements compared to the first one is smaller than 0.8%.

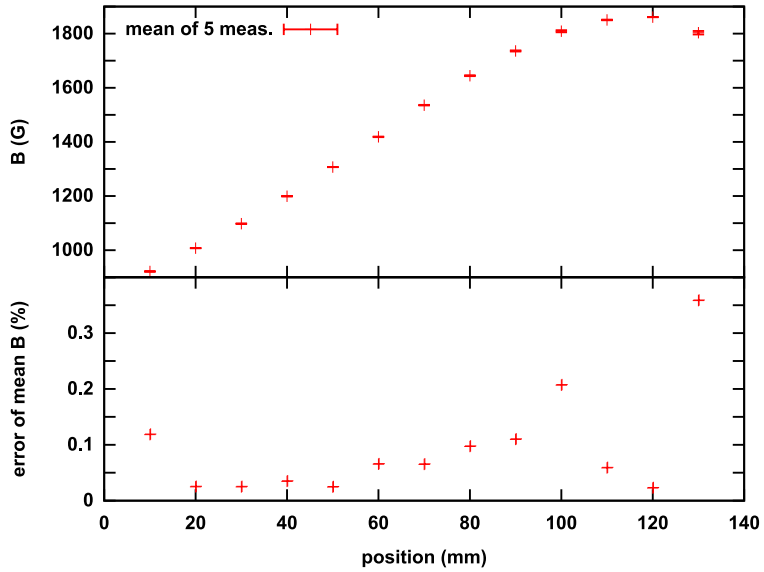

Figure 5.19.: Top: Magnetic field measured repeatedly along an arbitrary path. The mean of 5 measurements is given. Bottom: Error of average of the measurements in percent.

5.5.3. Coil position

As described in chapter 5.2, the central rotation axis of the magnet does not coincide exactly with the z-axis of the laboratory frame given by the wobble stick assembly. Due to the opposite current direction of the two coils there is a magnetic flux minimum in the center, as visualized in figure 5.20. The center of the magnet can be extracted from field measurements by localizing this minimum. This way, the offset between the magnet and the wobble stick assembly can be extracted and the performance of the measuring setup tested.
The area around the coil center is scanned in several horizontal slices, each at a different height (see figure 5.21). In each slice, which consists of circular scans around the middle, the strength and position of the field minimum can be extracted. Comparing the results of the scans at the different heights, the global field minimum can be localized.

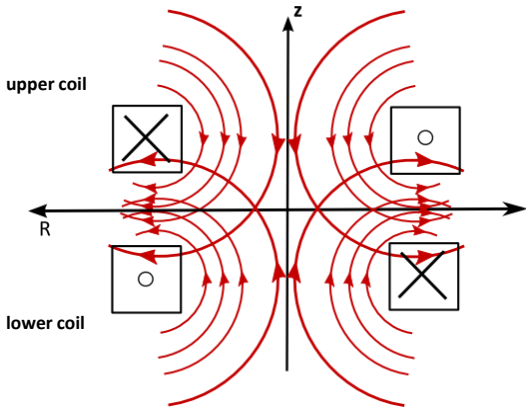

Figure 5.20.: Schematic, sectional view of the R-z plane of the coils: The magnetic field cancels in the center of the magnet.

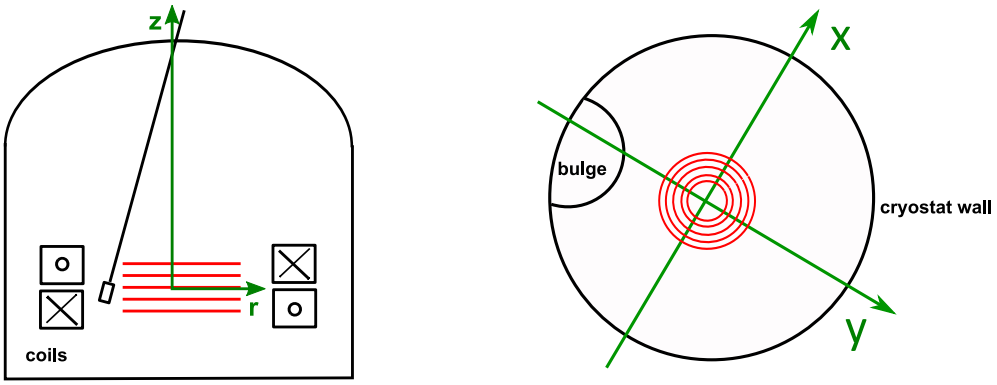

Figure 5.21.: Scan geometry to find the center of the magnet. Left: side view, right: top view.

Examplary, the result of one circular horizontal scan is given in figure 5.22. To find the field minimum, several methods have been tried. A second order polynomial fit did not yield satisfactory

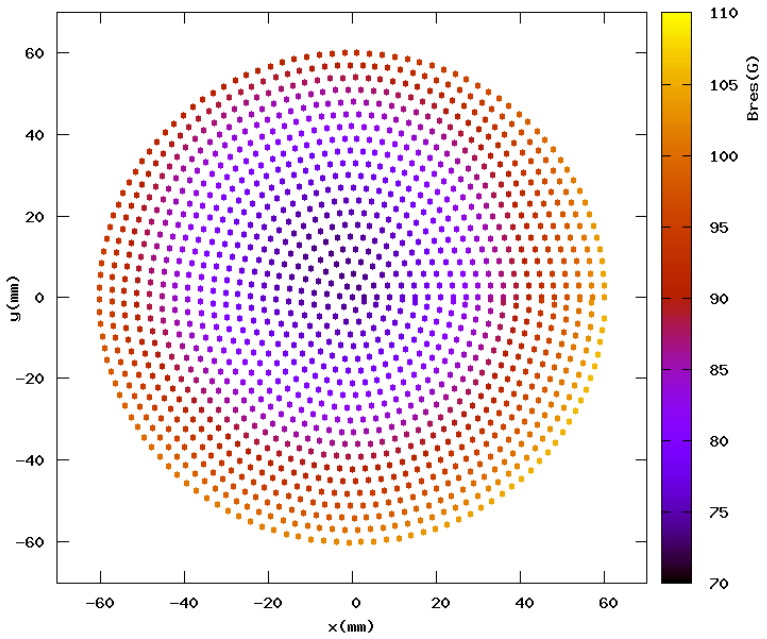

Figure 5.22.: Examplary horizontal scan at h=0 to find the coil center. The absolute value of the magnetic flux density is depicted in color code.

results (see figure 5.24).
Therefore, the so-called simplex downhill method (see [Pre07] for details) is applied to localize the minimum. This is a simple and robust, but slow minimum-search algorithm, that does not need any derivatives of the function to minimize. However, it needs to evaluate the function - in our case the absolute value of the magnetic flux as a function of the position - at arbitrary positions. As there is no simple, analytic expression describing the magnetic field data, an interpolation of the measured data is performed. The measuring points are not on a regular rectangular grid so that a simple tri-linear interpolation, as described in section 5.6, cannot be used. Instead, two different interpolation methods have been implemented: the radial basis function (RBF) interpolation and the Kriging algorithm, both described in [Pre07]. To test the performance of the different minimum finders, they have been applied to a field map calculated with Opera (see section 5.6). The result for the coil position determined by the minimum search algorithm can easily be compared with the position of the coils chosen in Opera when generating the field map.

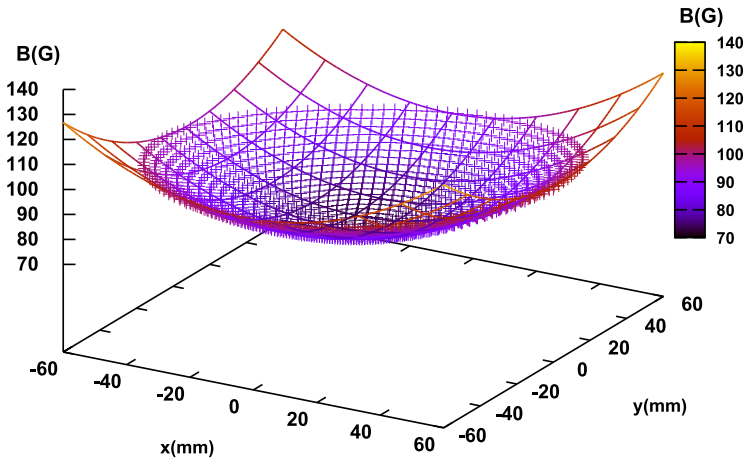

Figure 5.23.: Second degree polynomial fit to a horizontal magnetic field scan around the center of the magnet.

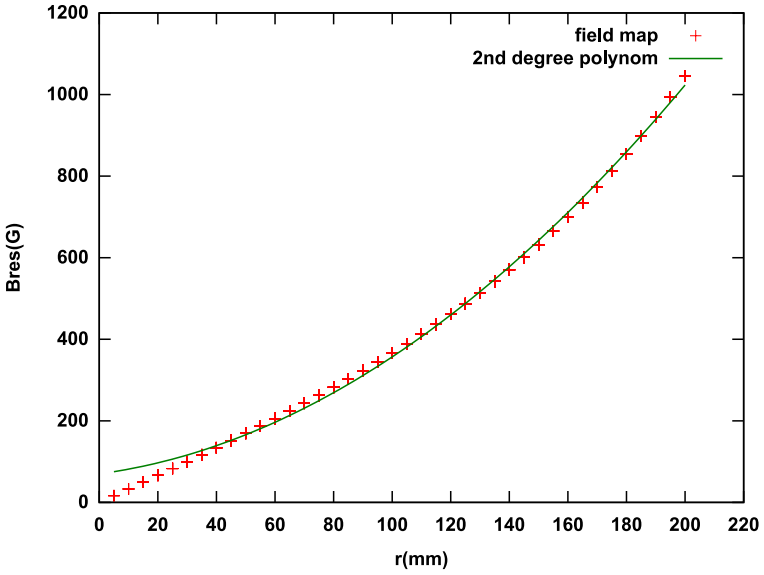

Figure 5.24.: Magnetic field B_{res} going radially outwards fitted with a second degree polynomial function. The relation does not represent the true geometry of the magnetic flux in the minimum.

Radial basis function interpolation RBF In this method, the magnetic field at a position is calculated by taking into account all known data points weighted by an assumed functional form ϕ that only depends on the distance r of the position to the data points. The standard model, the so-called 'multiquadric' function,

$$\phi(r) = (r^2 + r_0^2)^{1/2},$$

is used, where r_0 is a scale factor lying in between the point distance and the scale on which the data characteristics changes significantly. In figure 5.25 the influence of this parameter is depicted. It turns out to be rather small ($< 0.3\%$ in position, $< 5\%$ in the field value) especially when choosing r_0 in the range between 10 mm and 25 mm.

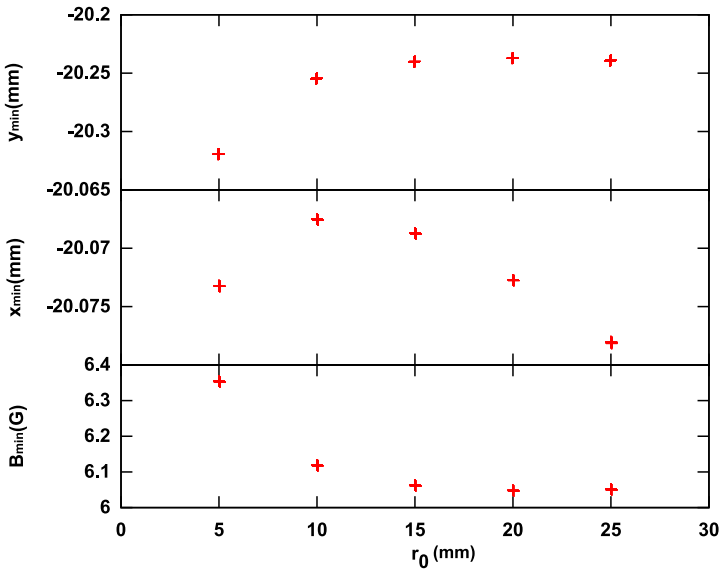

Figure 5.25.: Influence of the parameter r_0 on the results of the minimum search using the radial basis function interpolation. The algorithm has been applied to a field map calculated with Opera for a magnet with its center placed at $x = -20\,\text{mm}$ and $y = -20\,\text{mm}$. No coil tilt is implemented. From top to bottom the x-position, y-position and magnetic field value of the extracted field minimum is given.

Kriging interpolation and fit The Kriging method uses an estimator $v(r)$ for the mean square variation of the function to interpolate, depending again on the distance r to the next data point. For the interpolation, the method forces the function values strictly to the known data points. For a smoother and statistically better result, errors can be assigned to the data points and the interpolated values are allowed to differ from the data points within these errors. This procedure corresponds to a fit to the data points without knowing the analytical form of the function to fit. In both cases, the common model

$$v(r) = \alpha r^\beta$$

is used to estimate the variance, where β is a fixed parameter $1 < \beta < 2$ chosen by the user, and α is varied by the algorithm to find the optimum solution. The dependence on the choice of

β is shown in figure 5.26. In the fit method a 10% error has been assumed for the data points. Compared to the RBF-method, the influence of the model parameter is much larger: up to 2% in the position and 20% in the field value. Figure 5.26 does not clarify the choice of the parameter β. Whereas $\beta \approx 1.1$ gives a correct x-position, the y-position is only poorly reconstructed and suggests $\beta \approx 1.9$. Figure 5.27 again favours small β: For this plot, a map in which every second point has been omitted was fed into the interpolator. The omitted points were reconstructed by the interpolator and compared to the real values. This gives an interpolation error of less than 5% with single exceptions up to $70 - 80\%$ (for clearness their extreme values are not shown in figure 5.27). For smaller values of β the interpolating error is smaller.

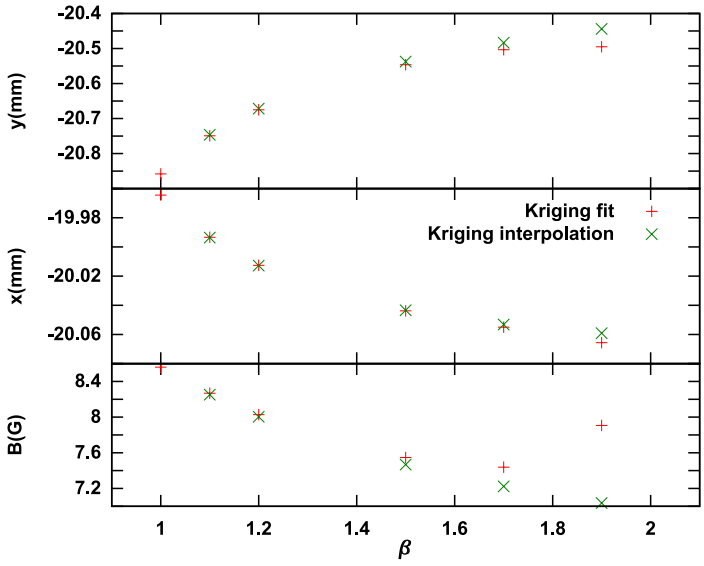

Figure 5.26.: Influence of the model parameter β on the results of the minimum search using the Kriging interpolation/fit. The algorithm has been applied to a field map calculated with Opera for a magnet placed at $x = -20\,\text{mm}$ and $y = -20\,\text{mm}$. From top to bottom the x-position, y-position and magnetic field value of the extracted field minimum is given.

The results of the different methods to localize the field minimum of the Opera map are summarized in figure 5.28. Additionally, the data point of the discrete map with the lowest magnetic field value is given. As the magnet center does not coincide with a grid point, this minimum only poorly represents the real center. The errors are either from the fit in case of the polynomial model or from the averaging over the model parameters in case of the interpolation methods. For all methods, varying the start point or the initial step size in the simplex downhill routine does not affect the results. Although the polynomial fit results in a magnetic field value which is far too high, the position is reconstructed correctly within < 1mm. The interpolation methods reconstruct the magnets center more precisely (within < 0.5mm) whereas the RBF-method is favored as the variation of the result with the model parameter is less pronounced (compare figures 5.25 and 5.26).

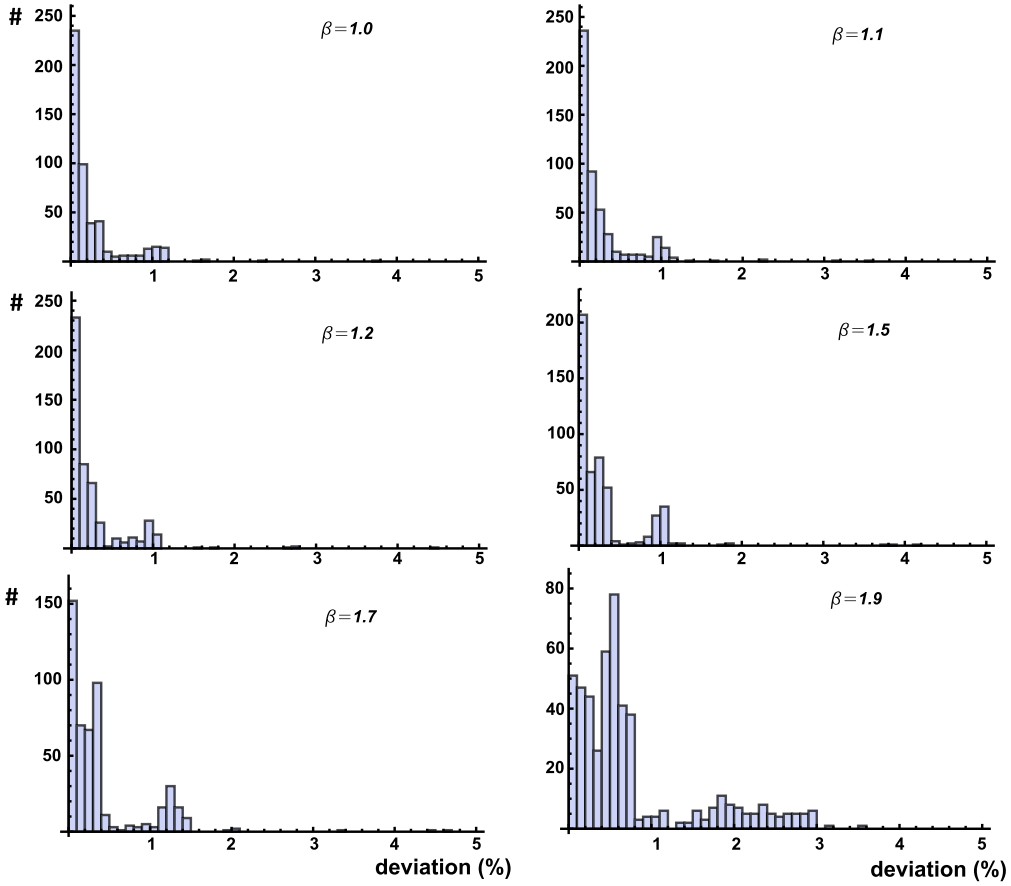

Figure 5.27.: Histogramm of relative deviation of the absolute magnetic field calculated with the Kriging fit algorithm for different β: In a map every second point is omitted and then reconstructed by the Kriging algorithm. The interpolated value in these positions are compared to the real values. The deviation is given in percent.

Results with real data When applying the RBF-interpolation to measured data the result is not independent of the choice of the start point nor the initial step size of the minimizer. In addition, it varies strongly with the model parameter r_0. Exemplary, in figure 5.29 the x- and y-position, derived with the RBF method, is given for one start point. The root mean square, when averaging the results obtained with different model parameters, is about 5mm.

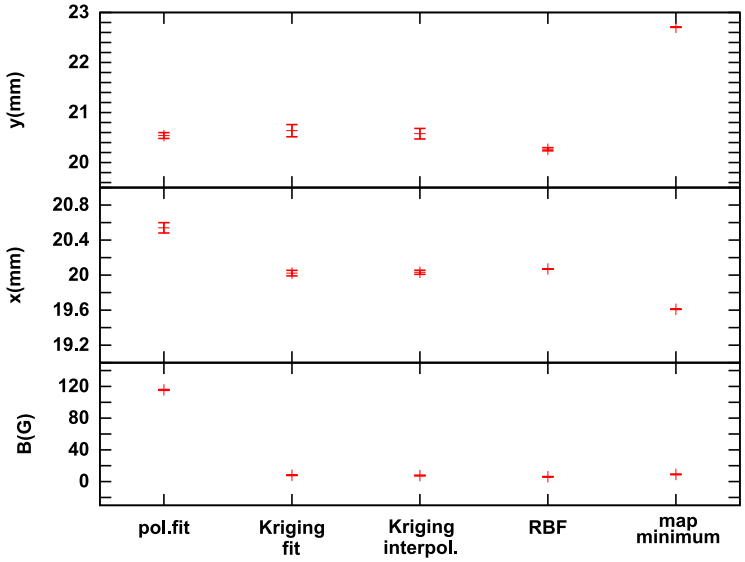

Figure 5.28.: Results of the minimum search on the calculated field map using different methods. Details are given in the text.

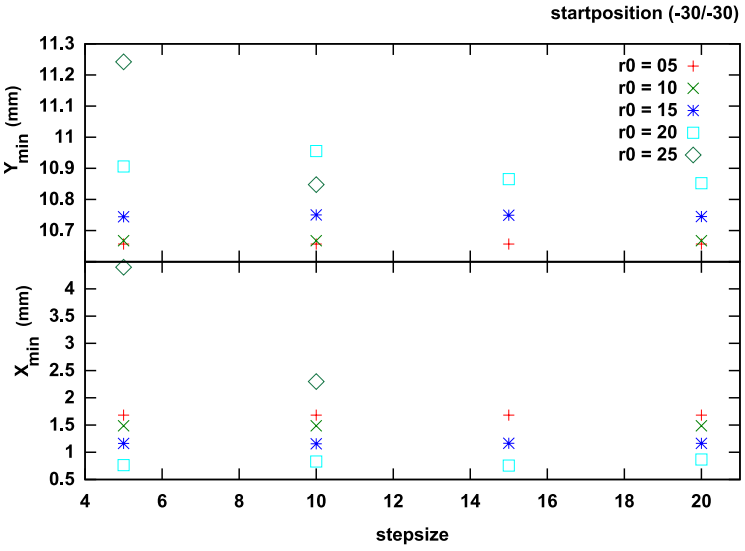

Figure 5.29.: Results for the x- and y-position of the field minimum using the RBF method on measured data. The initial step size as well as the model parameter r_0 were varied. The start point was at x=-30 mm, y =-30 mm.

As the Kriging method does not show this behavior, it has been used to locate the field minimum in the measured maps. In figure 5.30 the results are shown: the minima which have been found in the horizontal scans are plotted versus the height of the scans. The global minimum is extracted approximatively by the intersection of the linear fits to the falling and rising edge of the minimum. Looking at the x- and y-position of the local minima versus the height (cf. figures 5.31 and 5.32) yields the position of this global minimum. The fit results are summarized in table 5.2. The magnet center is finally determined with the Kriging fit method to be:

$$\begin{aligned} h &= 19.90 \pm 0.09\,\text{mm}, \\ x &= 0.2 \pm 0.3\,\text{mm}, \\ y &= 11.6 \pm 0.3\,\text{mm}. \end{aligned}$$

This result agrees with the mechanically determined position of the coil center: $x = 0.30 \pm 0.29\,\text{mm}$ and $y = 11.2 \pm 0.6\,\text{mm}$ (cf. section 5.3).

	slope m	Δ m	axis intercept b	Δb
linear fit to extract h-position of field minimum				
falling edge Kriging interpolation	-3.95	0.02	80.14	0.20
leading edge Kriging interpolation	3.91	0.01	-76.06	0.59
falling edge Kriging fit	-3.95	0.02	80.27	0.19
leading edge Kriging fit	3.88	0.01	-75.54	0.41
linear fit to extract x-position of field minimum				
kriging fit	-0.137	0.010	2.92	0.22
kriging interpolation	-0.127	0.019	2.75	0.41
polynomial fit	-0.130	0.004	3.19	0.09
linear fit to extract y-position of field minimum				
kriging interpolation result	-0.027	0.017	12.22	0.37
kriging fit	-0.030	0.009	12.23	0.2
polynomial fit	-0.050	0.008	11.71	0.18

Table 5.2.: Fit results of minimum search. C.f. figures 5.30, 5.31 and 5.32.

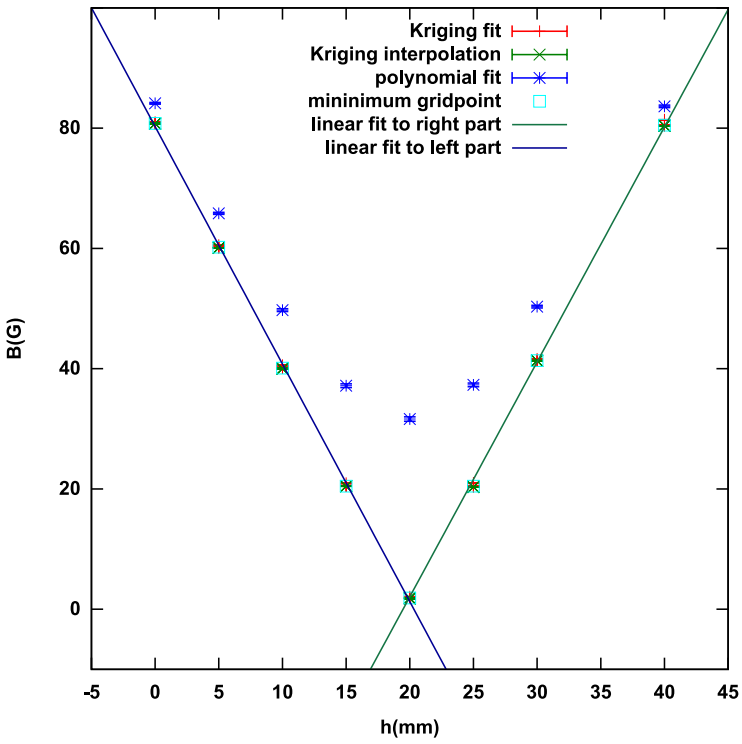

Figure 5.30.: Field minima of horizontal scans vs height to extract the global minimum.

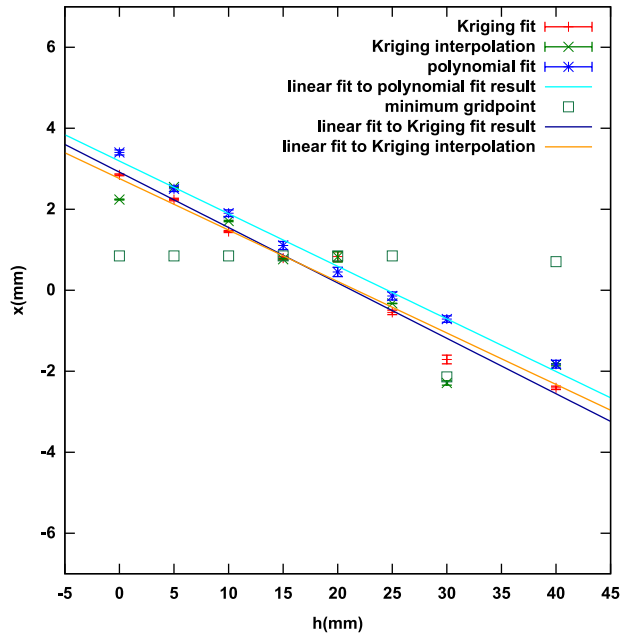

Figure 5.31.: X-position of the field minima from horizontal scans vs height.

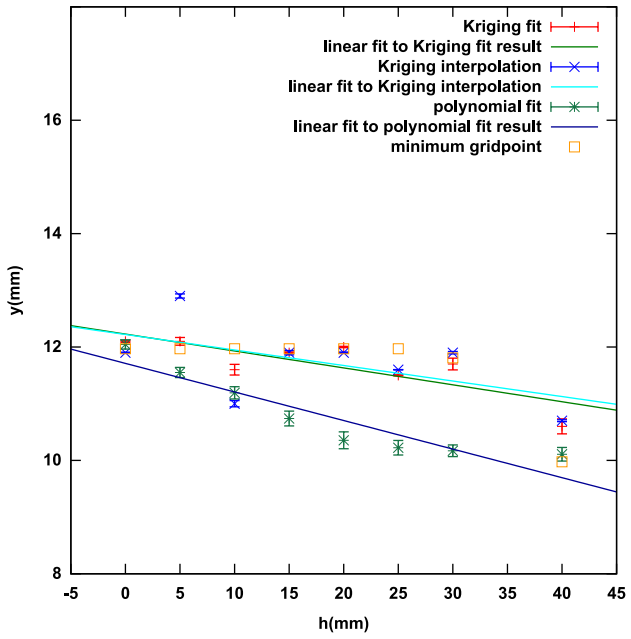

Figure 5.32.: Y-position of field minima from horizontal scans vs height.

5.6. Field calculations

With the finite element program Opera the magnetic field at any arbitrary position can be calculated using the Biot-Savart rule that gives the field around a current-carrying conductor:

$$d\vec{B} = I\mu_0/(4\pi)d\vec{l} \times \vec{r}/r^3.$$

With this calculated field map false effects like tilt and misplacement of the sensors can easily be investigated.

5.6.1. Interpolation

To save resources and avoid time-consuming field calculations, a grid of the whole magnetic field map is created once and thereafter the field at an arbitrary position is calculated via interpolation. As a regular rectangular grid can be created, it is possible to use a simple and fast tri-linear interpolation [Pre07]: First, the eight grid points being the corners of a box surrounding the target position are identified. The magnetic field at the target position is calculated by summing the magnetic fields at the corners of the box weighted by the distances from the target point to the corner points, respectively. For explanation, see figure 5.33. To estimate the error introduced

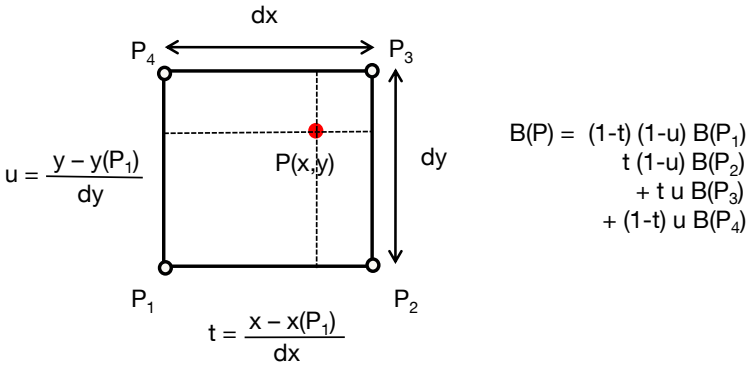

Figure 5.33.: Tri-linear interpolation of magnetic field grid. For clearness only a two dimensional example is given.

by the interpolation, three grids covering the same range with one, two and four mm spacings, respectively, have been compared. The error increases when getting closer to the coils due to the large gradient of the multi-pole arrangement. However, because of the magnet support and the cryostat wall the region close to the coils cannot be accessed by the Hall sensors and field mapping is restricted to the more benevolent area with a radial distance $r < 360\,\text{mm}$ from the central axis. In this region, the error is mostly smaller than $\approx 1\%$, when using the 2 mm grid spacing (see figure 5.34). Naturally, the relative error of the z-component is very large in the middle plane of the magnet, where the z-component has its zero crossing. Closer to the coil, with $r > 360\,\text{mm}$, the error quickly increases up to 10% for the dominant radial field component.

5.6.2. Sensor offset and tilt

The Hall generators for the three field components, mounted on the sensor support, have an offset of several mm with respect to each other and to the center of the support. As already pointed

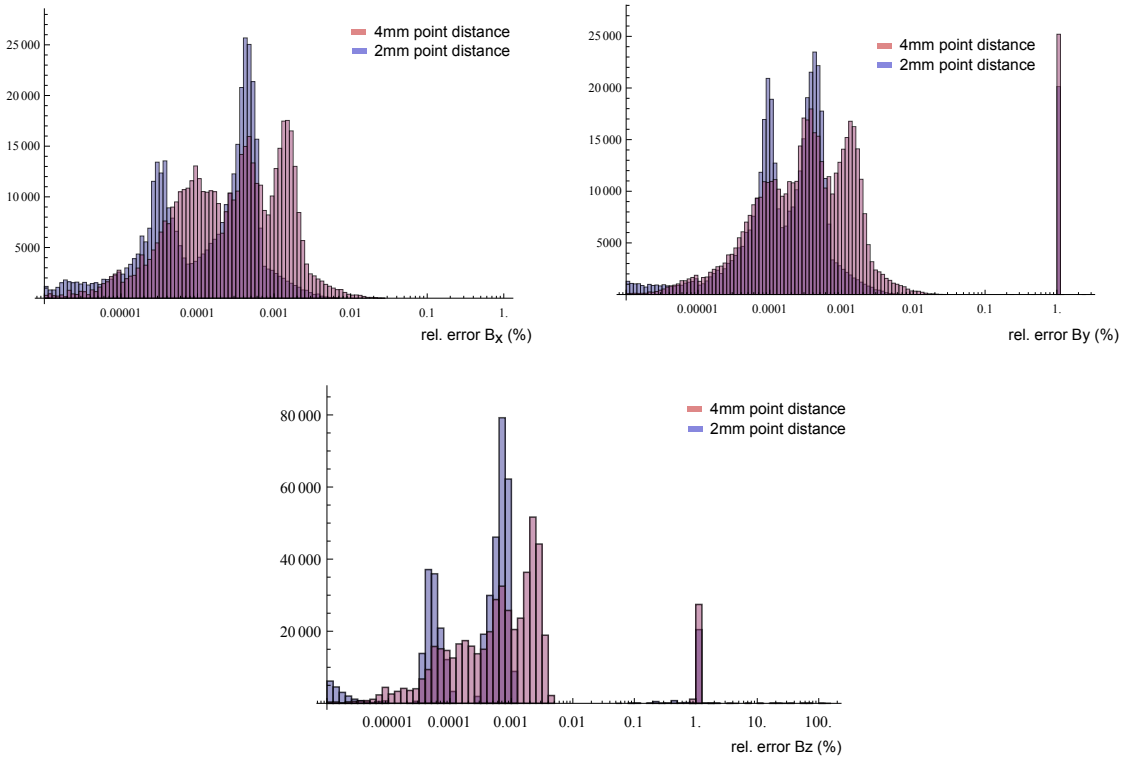

Figure 5.34.: Relative error introduced by interpolating the magnetic field grid in the area $r <$ 360 mm. Grids of two and four mm are compared to a one mm grid spacing for B_x (top left), B_y (top right) and B_z (bottom). The points where both grids coincide are not plotted. For these the error is zero by construction.

out in 5.4, correcting for this by placing every sensor in the same measuring position one after the other leads to a different tilt for each sensor and thus to the measurement of non-rectangular projections. With the calculated field map the consequences of both these effects - the offset and the tilt - can be estimated. The actual position and tilt of the sensors are calculated as described in section C. Figure 5.35 depicts the error induced by the Hall sensor offsets. The relative deviation of the magnetic field seen by the sensors at their real positions, respectively, to the magnetic field at the central position of the sensor head (the assumed position of the sensors when the offsets are ignored) is given. The relative error is mostly smaller than 10%. As the error is relative to the real magnetic field it is largest in low-field regions, thus in the middle of the magnet. E.g. the error in the z-component is up to 1000% in the middle plane (z=0) where B_Z has a zero crossing. However, in this region this component is also neglegible versus the radial part B_r and thus does not contribute to the absolute magnetic field.
Analogue, in 5.36 the error induced by the different tilt of the sensors is depicted. It is largest near the coils.

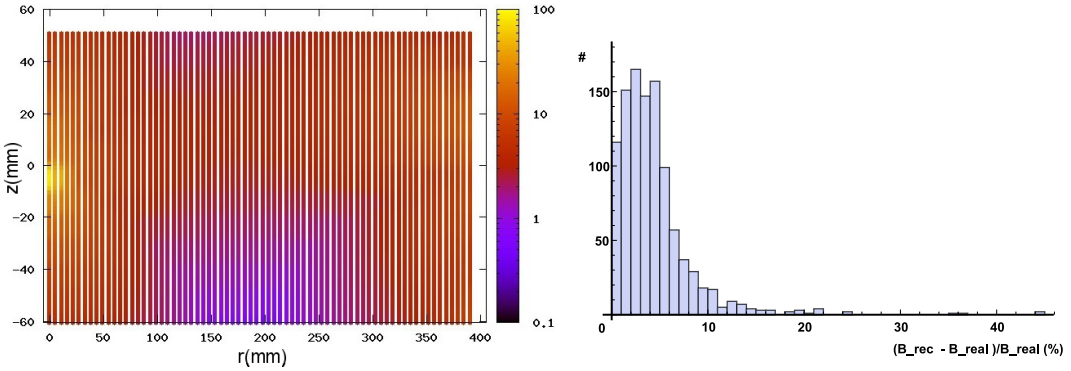

Figure 5.35.: Relative deviation of the magnetic field introduced by the sensor offsets for a vertical slice in the Rz-plane. The absolute magnetic field composed by the components at the actual sensor positions is compared to the real magnetic field at the central position of the sensor support. Left: error vs R-z-coordinates. Right: histogram of the error. Note the different scales compared to figure 5.36.

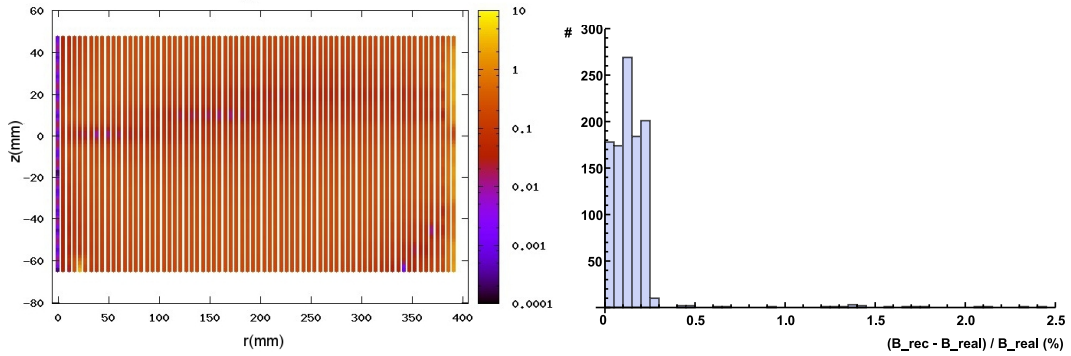

Figure 5.36.: Relative deviation of the magnetic field introduced by the sensor tilts for a vertical slice in the Rz-plane. The absolute magnetic field composed by the components seen by the tilted sensors is compared to the real magnetic field at the central position of the sensor support. Left: error vs R-z-coordinates. Right: histogram of the error. Note the different scales compared to figure 5.36.

5.6.3. Conclusion

Magnetic field mapping will be mandatory in PENeLOPE. Whereas an extensive search for unexpected zero-field regions will not be possible due to the large volume to be scanned and the spatial resolution necessary, a coarse global check of the magnetic field as well as selective, detailed scans of critical regions can be performed.
The main feature of the presented measuring setup is that the movement to guide the magnetic sensors is fed into the cryostat over a rotation center with two degrees of freedom. It turns out that this system is unfavorable due to the fact that small angular deviations on top of the cryostat lead to a large displacement of the sensors in the measuring plane. Small uncertainties, mainly connected with tolerances in the XYZ stage and the wobble stick, quickly sum up to a few mm. Angular misalignments transfer into wrongly reconstructed magnetic field components. Moreover, the measuring system is not applicable in the PENeLOPE setup with the geometry of two nested cylinders: the wobble stick would have to be placed off-center and would only reach a part of the volume to be probed. Several of these measuring systems would have to be used in parallel or sections scanned one after the other while rearranging the system in between. Instead, following the geometry of the experimental setup, a circular platform with the cross section of the storage volume, movable along the z-axis of the setup should be installed (see sketch in figure 5.37). On this platform a carriage could travel around on a circular track to adjust the angular position in the r-Φ-plane. Finally, on the carriage itself a linear movable sensor head would be needed to change the radial position. Whereas the height of the platform, the z-position, could be regulated by means of a linear feed through with the actuator placed outside the cryostat, the movement in angular and radial direction would have to be managed by actuators placed inside the cryostat. Thus, low-weight actuators capable of cryogenic temperatures and operable in high vacuum are needed.[19] This arrangement would imply that the magnetic field is measured

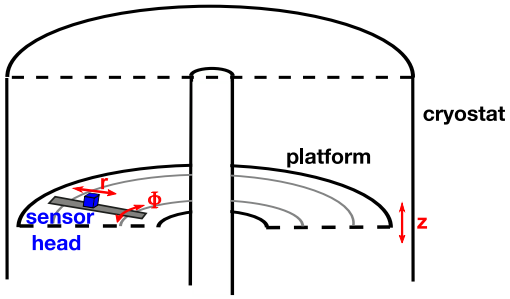

Figure 5.37.: Sketch of an alternative field mapping setup for PENeLOPE.

in a cylindrical coordinate system. The transformation of the measured field components into a Cartasian laboratory frame is much easier than with the system used in CoTEx, as there is no position dependent tilt of the sensors and thus the components are measured in an orthogonal coordinate system. Moreover, the FEM programs used to calculate the field map, like Opera, also give the field components in exactly this cylindrical coordinate system as it follows the natural

[19] The same problems show up at other aspects of the PENeLOPE experiment. A movable neutron absorber, needed to shape the neutron spectrum for systematic studies and suppression of false effects will be installed. These have to be actuated and moved in the same harsh environment inside the cryostat. Thus, development of these components can lead to synergies.

symmetry of the coil system.
Analyzing the measured field map might require interpolation as an analytical form of the field shape does not exist for the highly complex field geometry of the PENeLOPE system. For regular rectangular or irregular grids standard algorithms have been successfully applied as described.
The presented minimum search shows that information on the magnetic field, here its center of zero field, can be extracted with a precision of an order of magnitude better than the accuracy in positioning the sensors themselves. Again, for the minimum search a standard algorithm, the simplex downhill method, could be used. The matching of a measured map with a calculated map would also result in a minimum search; the variable to be minimized is the sum over the differences between the magnetic field in the grid points of the measured map to the magnetic field of the calculated map. The parameters to vary are at least the translative offsets between the maps in all three dimensions and the tilt of the maps with respect to each other around all three axes. In a rotational symmetric system the degree of freedom for the rotation around the symmetry axes must be omitted to have a defined solution. A scale factor for each field component to compensate for offsets of the sensors can be introduced as well. The large number of parameters and measuring points will possibly lead to an immense computing time, if a solution is found at all. The possible misalignment of the individual coils of the PENeLOPE magnet with respect to each other and the resulting deformation from the ideal field complicate this even more. Thus, only sections or two dimensional slices could be investigated. Important field regions are e.g. those close to the storage container walls to check the trap potential and suspected zero-field regions.

6. CotEx 2 - cryostat upgrade and test of base-coil prototype

In the detailed design phase of the PENeLOPE magnet with Scientific Magnetics as industry partner, severe problems occurred: Scientific Magnetics suddenly questioned the feasibility due to engineering problems, and the first prototype coil pair failed at 70% of its nominal current. Subsequently, the coil manufacturer was changed to Babcock Noell (BNG): a new feasibility study was started in 2010, which was followed by a detailed design. A thorough revision of the experimental design lead to the setup as described in chapter 3. The new approach for the coil design taken by Babcock Noell implied the need of another prototype coil. [Ste11a] This test magnet resembled the innermost bottom coil of the PENeLOPE system as construction wise this coil is expected to be the most problematic one due to its unfavorable dimensions (a large radial thickness combined with a small outer radius). The new prototype did not fit into the existing CoTEx cryostat with its ring shaped helium vessel, and a complete new cryostat had to be built. The CoTEx 2 cryostat was designed to fit all PENeLOPE coils for future training - individually or in stacks of up to three coils. The cryostat setup and the performance test of the prototype from Babcock Noell are presented in this chapter.

6.1. Base-coil prototype

In contrast to the first test magnet from Scientific Magnetics, which consisted of two coils to test the inter coil forces, the new prototype is a single coil with the dimensions of the innermost base coil of the PENeLOPE setup (see figure 6.1). The specifications of the prototype are summarized in table 6.1, a technical drawing is given in appendix E. The superconducting wire is again made of NbTi, has a bare diameter of 0.9 mm and a varnish insulation of 0.25 mm thickness. The copper to superconductor ratio is with 1.5 to 1 a bit lower compared to the wire used in the first prototype. The critical current at 5.5 T is about 450 A. Scientific magnetics suggested a free-floating bearing of the coil (see section 4.4.3). Instead, BNG favors a rigid support including a large pretension on the wire preventing any movement of the coil with respect to the support structure. To compensate for the different thermal and electro-magnetic stresses produced during cool down and powering of the magnet, a different pre-stress is applied to the wire for every single layer of the coil pack while winding the coil onto the former. However, the wire tension needed to prevent a detachment from the former under all conditions might lead to tensile stresses on the former of more than 200 MPa, which is getting close or even possibly exceeds the strength of the former.
Babcock Noell uses a winding machine with a precisely controlled wire feed by means of an automatic break. In contrast, Scientific Magnetics wounded by hand, exerting an undetermined and not reproducible manual force on the wire. With the prototype, the envisaged winding technique of the PENeLOPE coils was tested.

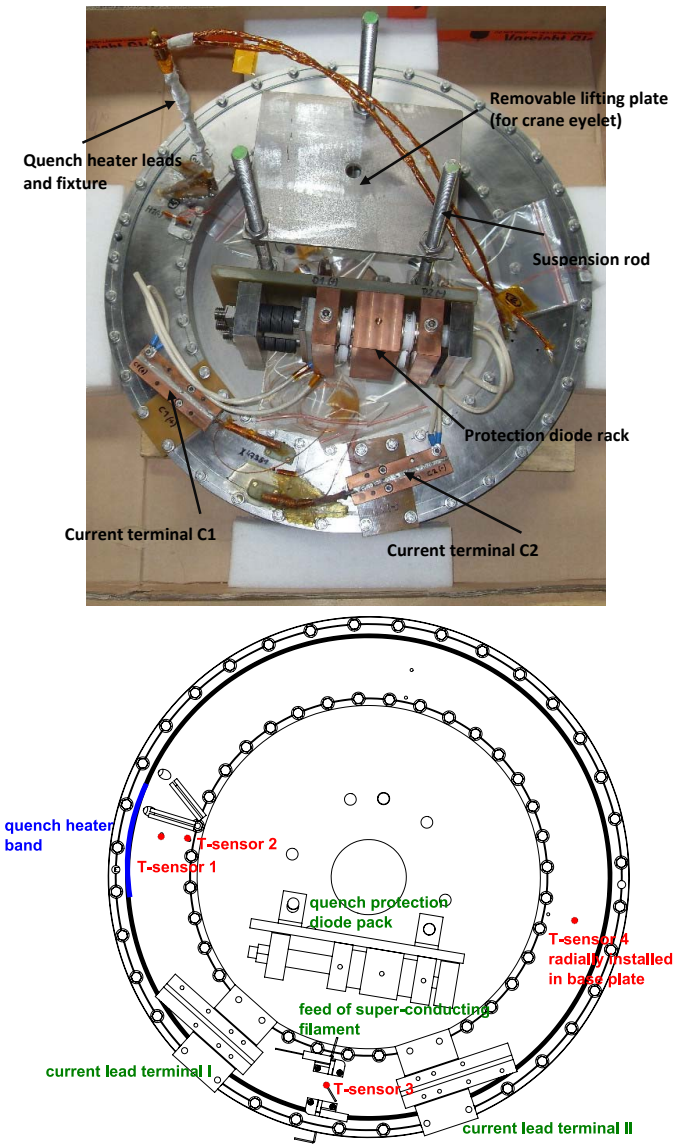

Figure 6.1.: The prototype coil from Babcock Noell. Top: a picture. Bottom: a top view sketch.

geometry	
outer radius of support	252 mm
inner radius of support	198 mm
height of support	56 mm
inner radius of coil windings	198 mm
radial width of coil windings	53 mm
height of coil windings	33 mm
windings	1885
weight	80 kg
$\alpha = r_o/r_i$	1.29
operating conditions	
operating current	291.5 A
current density (w.r.t. complete wire)	411 A/mm^2
stored energy	105 kJ
maximum field at nominal current	5.5 T
nominal ramp rate	2.9 A/s
normal resistance R	112 Ω
inductance L	2.49 H

Table 6.1.: Specifications of the test magnet from Babcock Noell. [Ste11a] See also figure 6.1.

6.1.1. Peripheral components

Temperature sensors The temperature of the magnet is logged with four sensors specially designed for cryogenic temperatures. The sensors are integrated in the coil support structure as close as possible to the coil winding package (see figure 6.1).

Protection diodes Like the test magnet from Scientific Magnetics, the new prototype coil is equipped with cryogenic high-power diodes to protect the coil against large voltages. For each current direction, two anti-parallel diodes with a forward voltage of $U_f \approx 14\,\mathrm{V}$ in total are installed. Exact values for U_f at cryogenic temperatures and in magnetic fields are not know (see section 6.3.2).

Quench detection system The passive protection system with the diodes, has been extended with an active quench detection. The voltage at the magnet is measured directly at the coil taps with a high time resolution of 250 ksamples/s using an Agilent U2352A acquisition module. The voltage increase following a quench (compare section 4.4.1) is detected by the device, which subsequently triggers the shut down of the power supply within 150 ms. For more details refer to [Sen11].

Quench heater A resistive steel band is attached to the magnet which can be powered with a short, but large current pulse. The joule heating of this resistive band ($R \approx 70\,\mathrm{m\Omega}$ at liquid helium temperature) than artificially induces a quench of the magnet. The steel band has a length of 100 mm, a width of 10 mm and a thickness of 0.1 mm; it is wrapped in Kapton tape for electrical insulation and directly attached to the coil winding package at its outer radius (cf. figure 6.1).

6.2. Cryostat upgrade

The CoTEx 2 cryostat comprises a new vessel system: the helium tank, the radiation shield, the vacuum tank and the complete support structure including a lifting device. Still, a big part of the infrastructure of the old setup could be reused, namely the helium and nitrogen transfer lines, the bellows and the safety installations (back-gas line, safety valves), the complete sensor equipment (for temperature, vacuum, overpressure, helium level and magnetic field measurements) and the slow-control, vacuum feed-throughs and the current leads for the magnet (cf. section 4.2).

6.2.1. Cryostat design

A sketch of the new cryostat is given in figure 6.2. It has been designed based on the experience

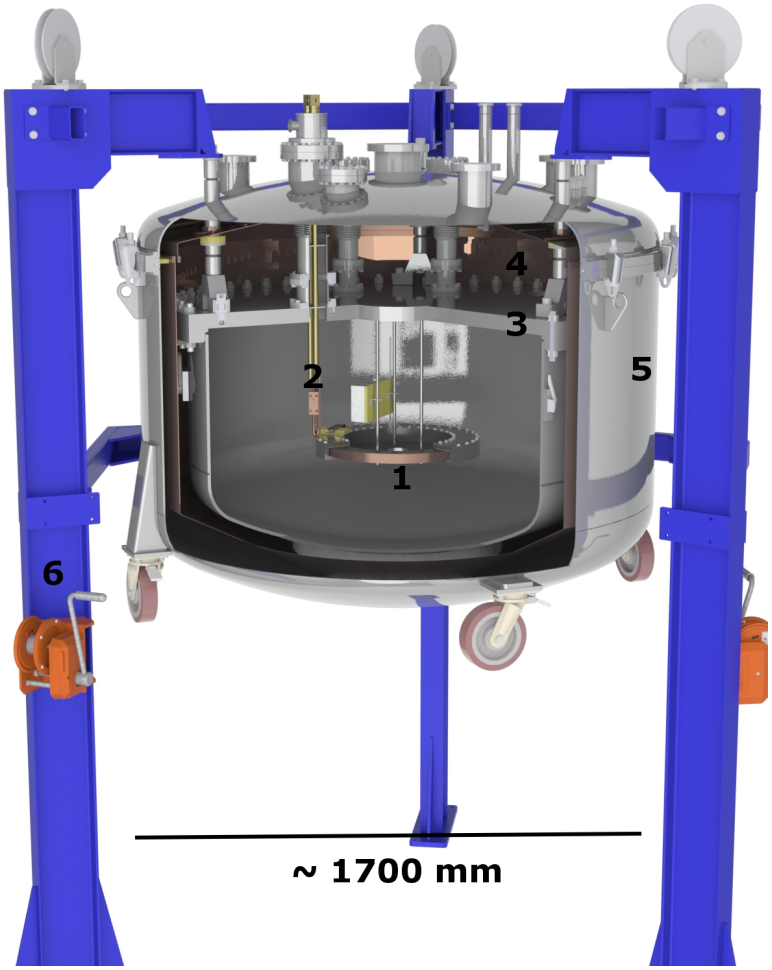

Figure 6.2.: 3D-model of the CoTEx 2 setup. (1) Prototype magnet (2) current leads (3) Helium vessel (4) radiation shield (5) vacuum tank (6) prop frame with lifting device.

with the CoTEx 1 setup. Whereas basic design principles have been reused, larger dimensions,

bigger masses and higher expected magnetic field energies, lead to several changes in the setup:

- The new cryostat can be used to test all PENeLOPE coils, individually and in packages of three. Thus, the helium vessel is not ring shaped like in the CoTEX 1 cryostat, but a cylindrical vessel, 0.8 m high with a diameter of 1.4 m. It has a volume of $\approx 1000\,\mathrm{l}$, six times as much as the old helium vessel. The installation of a magnetic field mapping device has been omitted.

- The helium vessel of CoTEx 1 was made of aluminum to reduce weight and material costs. The top cover had a thickness of 28 mm. In the beginning, leakage problems showed up, especially in the region of the balcony in case of overpressure, preventing a successful cool down. Either the surface was not perfectly flat or the combination of material and flange thickness resulted in a lack of stiffness of the top cover, so that the force necessary for the indium sealing to be pressed tight could not be applied. Only the additional installation of clamps at the balcony made an operation of the cryostat possible. Thus, in view of the much larger surface the (over-)pressure is acting on, the new helium vessel is made of stainless steal instead of aluminum. The thickness of the top plate has been increased from 28 mm to 47 mm. To press it to the vessel body, 42 M22 bolts are used.

- To safe liquid helium, it is necessary to fill the helium vessel mostly with polystyrene as displacement. In order to still allow for an efficient heat transfer via helium gas convection, channels have been foreseen in the polystyrene blocks. [Sen11]

- As in case of the old cryostat, all inner parts are suspended from the vacuum tank top, which itself is mounted to a support structure. The mass of the complete setup sums up to $\approx 2.5\,\mathrm{t}$ in total, depending on the coil configuration. The much increased weight compared to CoTEx 1, especially of the helium vessel and the coil system, demanded for a thorough design of the support, which has to be stiff enough to bear the load but uses as little material as possible to minimize heat input to the cold parts. Three support rods made from stainless steel, with a diameter of 50 mm and a length of 240 mm, are welded into the vacuum tank top. They are fixed at the top to the outer prop frame and reach down into the vacuum tank. At an intermediate height, the nitrogen shield is attached; at the lower end, the lid of the helium tank is fixed. The rods, being in direct contact to the helium vessel as well as the support frame at room temperature, introduce a thermal bridge; The nitrogen shield and helium tank top are thus attached using GFK spacers as insulators. A cryogenic inspection is given in section 6.2.2. The main advantage compared to the old setup is that the complete load is transfered in a straight line through a stiff part to the outer support frame.

- To increase safety against critical overpressure, a burst disk has been installed at the helium tank, besides the safety valves already used in the CoTEx 1 setup. The disk triggers at 1.2 bar, the opening pressure of the safety relieve valves at the back-gas line to the receiver balloon has been reduced to $\approx 500\,\mathrm{mbar}$ and the ones at the tank top opening to the experimental hall itself to 800 mbar (at CoTEx 1 it was 800 and 1000 mbar, respectively). The bellows have been equipped with prop tubes welded to the inner side of the vacuum tank top, covering 2/3 of the length of the bellows. This obviates the bellows buckling off to one side.

6.2.2. Cryogenic design

During the first cool-down attempt of the CoTEx 2 setup, helium could not be liquefied into the tank but the temperatures of the helium vessel stagnated at $\approx 20\,\mathrm{K}$. Besides a bad helium gas circulation due to the styrofoam insert, the heat input to the helium vessel through the support rods and the bellows was suspected to be too large. Hence, afterwards a heat bridge by means of a copper cable has been installed between the support rods and the nitrogen shield. Also the prop tubes around the bellows introduce additional warm surfaces close to the helium vessel; they have been coupled to the liquid nitrogen shield, too. Thus, heat load is shifted from the helium tank to the nitrogen shield. Remaining uncovered surfaces of the rods and the bellows have been wrapped in reflecting super-insulation foil. These measures reduced the heat input by roughly 18 W.[Sen11]

Support rods The heat input through the three support rods has been estimated with a simplified model and more detailed using the Solid works simulation tool. A sketch of one of the support rods is depicted in figure 6.3. It consists of the rod itself and a yoke attached at its lower

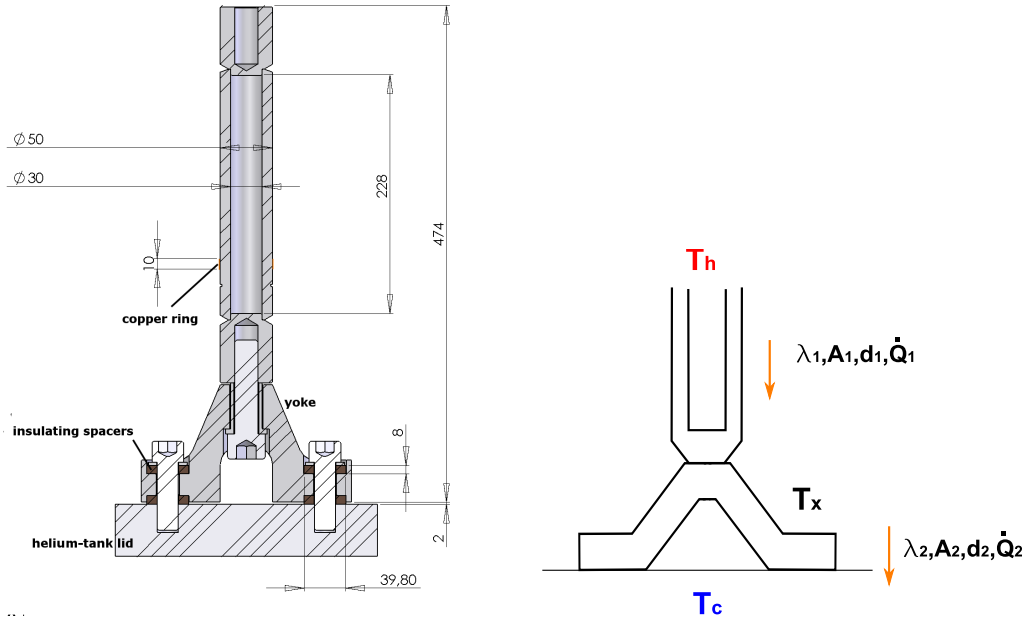

Figure 6.3.: Left: CAD drawing of the support rod. The copper ring has only been added for the thermal analysis. It represents the coupling to the radiation shield. Dimensions are in mm. Right: Simplified model for estimation of the heat input through the support rods.

end, which is screwed to the helium tank lid using insulating spacers made of FR4 for thermal decoupling of the parts. In its middle section the rod is designed as a tube to minimize the cross section and therewith the heat conduction.
In figure 6.3, right part, the model of the support used to roughly estimate the heat transfer is illustrated. The heat flow $\dot{Q}$ from the warm part at temperature T_h to the cold part at T_c calculates as

$$\dot{Q} = \frac{\lambda}{d} \cdot A(T_h - T_c).$$

Here, λ denotes the heat conductivity of the material, A and d the cross section and length of the object. In a simplified picture two bottlenecks exist for the heat transfer: The first one is the part of the rods having the minimum cross section - length combination; this is the tube-like section. The second bottleneck is constituted by the insulating spacers between the yoke and the helium tank lid. In the equilibrium state, the heat flow $\dot{Q}_1$ from the warm reservoir with temperature $T_h = 300\,\mathrm{K}$ through the first bottleneck (A_1, d_1, λ_1) to the middle part equals the heat flow $\dot{Q}_2$ from the middle part through the second bottleneck (A_2, d_2, λ_2) to the cold reservoir $(T_c = 12\,\mathrm{K})$[20]. The middle part (the yoke) then stabilizes at a temperature T_x:

$$\begin{aligned}
\dot{Q}_1 &= \frac{\lambda_1}{d_1} \cdot A_1(T_h - T_x). \\
\dot{Q}_2 &= \frac{\lambda_2}{d_2} \cdot A_2(T_x - T_c). \\
\dot{Q}_1 &= \dot{Q}_2 = \dot{Q}. \\
\Rightarrow \dot{Q} &= \frac{\lambda_1 A_1}{d_1}(T_h - T_c) \cdot \frac{1}{1 + \frac{\lambda_1 A_1 d_2}{\lambda_2 A_2 d_1}}.
\end{aligned}$$

With

$A_1 = 1256\,\mathrm{mm}^2$, $d_1 = 240\,\mathrm{mm}$,

$\lambda_1 = 10$ W/mK (the value of the heat conductivity of stainless steel at room temperature),

$A_2 = 4 \cdot 926\,\mathrm{mm}^2$ (four spacers are installed at the screw connecting the yoke to the helium vessel lid),

$d_2 = 8\,\mathrm{mm}$ and $\lambda_2 = 0.15$W/mK (the value of the heat conductivity of FR4 at 30 K)

the heat input through one support calculates to 8.5 W corresponding to an evaporation of 11.6 l/h liquid helium. The temperature of the middle section is $T_x = 135\,\mathrm{K}$. For comparison, the same calculation for the geometry of the old CoTEx 1 setup gives a heat input of 1.26 W per support, which translates to 1.7 l/h of liquid helium consumption.
This simple estimation is lacking the real geometry and the temperature depended heat conductivity of the materials. Thus, the Solid Works simulation tool has been used to model the temperature distribution more realistic. The model uses the real technical geometry with all screws, washers and spacers (cf. figure 6.3) and includes data for heat conductivity of stainless steel and FR4 from room temperature down to 4 K. [M+00] The top surface of the upper end of the rod has been fixed to 300 K; the bottom surface of the material block representing the helium vessel lid to 12 K. Missing is the correct heat transport characteristics at material boundaries. A perfect heat transport has been assumed here as a worst case scenario. The results are depicted in figure 6.4. Also the case when the support rod is coupled to the liquid nitrogen cooled radiation shield has been considered. To this end, in the simulation model a copper ring has been attached to the rod and fixed at $T = 78\,\mathrm{K}$. Without the coupling to the radiation shield, the temperature of the yoke is $T_{\mathrm{yoke}} \approx 90\,\mathrm{K}$ and the heat input to the helium tank lid about 1.6 W per rod. With the simple estimation mentioned above the temperature was calculated to be 135 K; thus, the calculation overestimates the heat input. The coupling to the radiation shield reduces the temperature to $T_{\mathrm{yoke}} \approx 60\,\mathrm{K}$. In this case, the heat input is 1.26 W per rod, according to the simulation.

[20] The lid of the helium vessel showed a temperature of 12 K when the cryostat was filled with liquid helium.

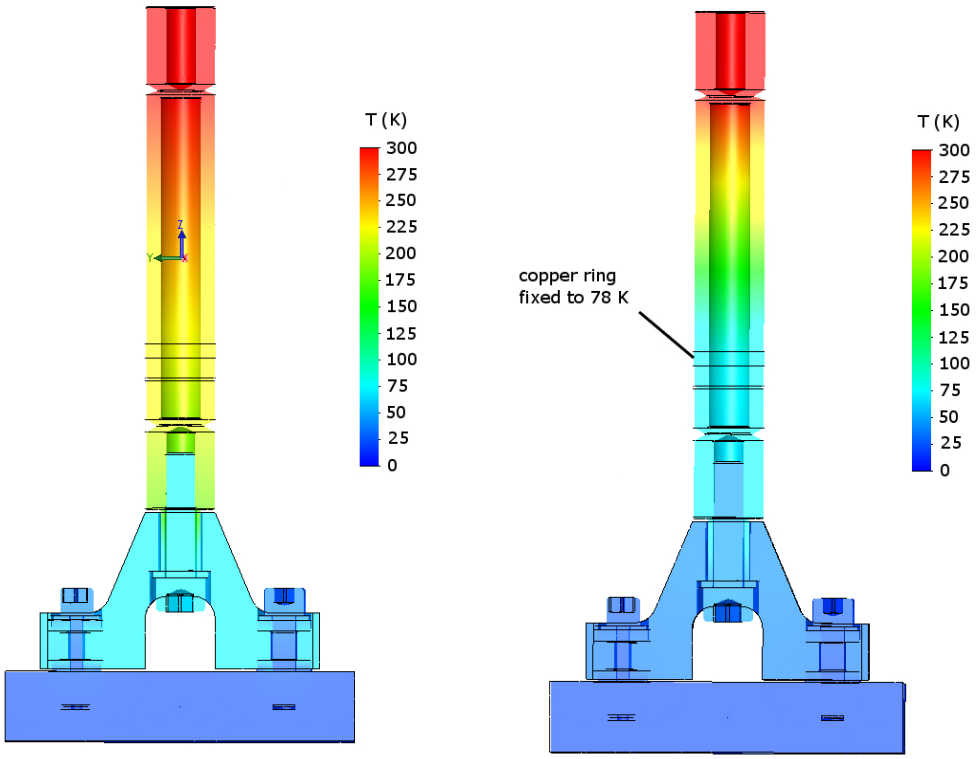

Figure 6.4.: Thermal analysis of the support rods. Left without, right with the coupling to the nitrogen shield.

The temperature distribution has also been monitored in the experiment by several sensors attached to the support: the yoke stabilizes at a temperature of $T_{\text{yoke}} \approx 76\,\text{K}$. This agrees quite well with the simulation result; in particular, because a possible bad coupling of the sensors might suggest higher temperatures than the parts really have. The screws fixing the yoke to the helium tank lid had $T_{\text{lid}} \approx 18\,\text{K}$ and the support rod $T_{\text{rod}} \approx 56\,\text{K}$ (in the middle between the yoke and the position where the liquid nitrogen shield is coupled to the rod). From the measured temperature distribution, the heat input $\dot{Q}_{\text{support}}$ to the helium tank through the support is estimated with the formulas listed above to be $\dot{Q}_{\text{support}} \approx 4\,\text{W}$, thus significantly higher than the simulation suggests. Additionally, the total heat input to the helium tank can be calculated from the temperature increase during warming up the cryostat, when the liquefier is turned off. This gives $\dot{Q} = 17\,\text{W}$, including not only conduction through the three supports, but also thermal radiation.[Sen11] The measurements, supported by the simulation results, show clearly that the measures to reduce the thermal load on the cryostat were effective.

6.3. Performance tests

The main objectives of the tests were the confirmation of the coil design and the exploration of the magnet limits. In detail this includes a validation of the production process i.e. the winding scheme and the achievable wire packing factor and the investigation of the operating behavior of the coil such as training and quench characteristics, longterm stability and ramping losses. At the same time, further components such as quench heaters, protection diodes and the quench detection system were tested. The scheme and the equipment to power the magnet has been taken from CoTEx 1.

6.3.1. Packing factor

The packing factor is defined as the ratio of the coil cross section filled with superconducting wire to the total area. A 3d laser scan measurement of the winding package revealed that the packing factor is about 81.5% (cf. figure 5.3). Theoretically, at most 79.6% should be possible with the regular hexagonal packing pattern used and glass cloth as interlayer insulation. The higher packing factor of the prototype results most probable from a compression of the glass cloth layers during winding. The effective thickness of the insulation must have reduced from 0.1 mm to 0.08 mm. Beside the bump due to the wire crossing at layer transitions, which has been already discussed in the introduction of chapter 5, the laser measurement suggests a very regular structure of the coil winding and confirms the winding technique. [Ste11a]

6.3.2. Training

As in the training of the prototype magnet from Scientific Magnetics, the coil has been ramped up stepwise and slowly with 0.5 A/s until a quench occurred. There was a pause of at least 30 seconds at every holding point of the ramp curve. The quench history is depicted in figure 6.5. With the

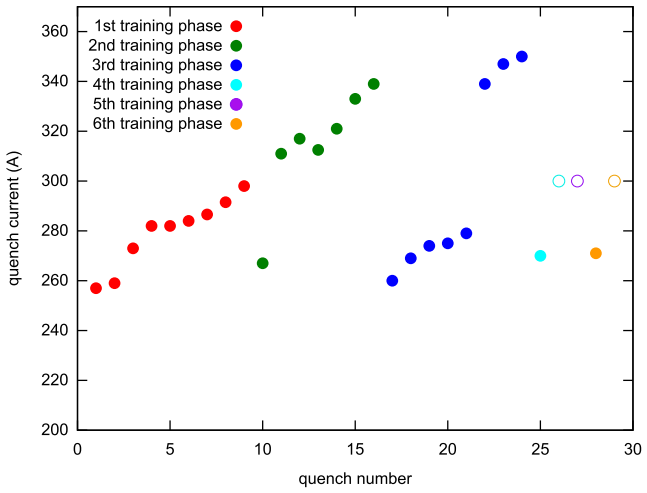

Figure 6.5.: Training curve. While the full circles give quench currents, the unfilled circles mark ramps, where the nominal operating current has been reached without a quench. See text for details.

ninth quench at 298 A the nominal operating current of the coil (291.5 A) has been exceeded already. Subsequently, the coil has been warmed up to room-temperature and cooled down again. In this way it was checked whether the coil remembers the training effect or if stresses from large temperature changes make a re-training necessary. The first quench after the temperature cycle was at 267 A and thus at a lower current than has been reached before. However, already at the next ramping a new maximum current of 311 A was reached. Four more training phases with temperature cycles to room temperatures in between were performed after this work and gave a clearer picture of the re-training behavior: In the third training phase five quenches occurred, before the nominal operating current was exceeded again (reaching a new maximum current of 350 A). Thereafter, the magnet quenched only once or not at all while ramping to nominal operating current.[21] For PENeLOPE this implies long training phases for every coil including temperature cycles. Additionally, also in the running experiment quenches, when ramping up the magnet after a phase at room temperatures, cannot be excluded. In figures 6.6 and 6.7 the temperature of the coil, current and voltage of the coil as well as the magnetic field monitored by a cryogenic hall sensor are given for an exemplary quench. Noticeably, at every quench

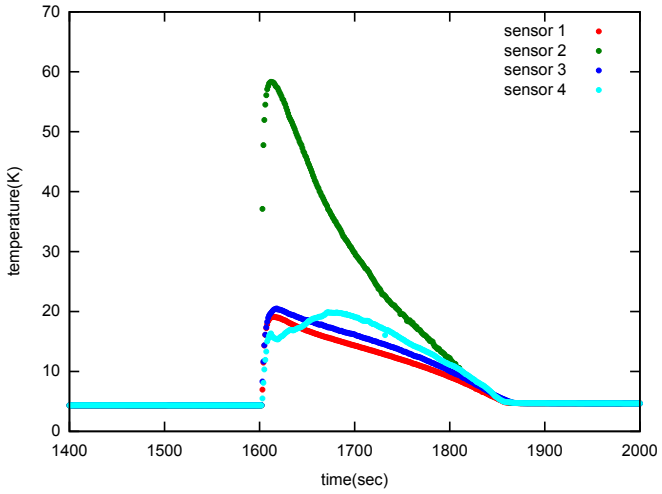

Figure 6.6.: Exemplary temperature development at a quench.

incident the temperature sensor 2 showed the largest temperature increase. Sensors 1,3 and 4 experienced an increase all in the same order, but much smaller; in this example only one third. Looking closer, sensor 3 seems to have the second highest temperature increase - sometimes more, sometimes less pronounced. Whereas sensors 1,2 and 3 reacted promptly, a delay of the order of 60 s can be observed for sensor 4. This behavior is easily understood if looking at the location of the sensors (cf. figure 6.1): as the heat transportation perpendicular to the superconducting wire is much worse than along it, the temperature distribution suggests that the quench always happened at the inner radius of the coil, probably close to the position of temperature sensor 2 or 3. As depicted in figure 6.8, the peak temperature does not change significantly with the quench current. There is only a slight increase of the temperatures, more prominent for sensors 1,3 and 4 than for sensor 2.

[21] As already 120% of the nominal current were reached in the third phase, it was omitted to go for higher maximum currents, in order not to risk damaging the magnet.

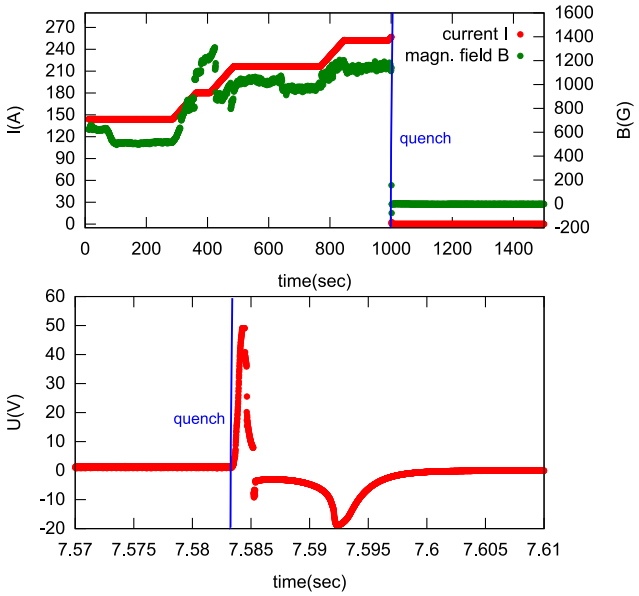

Figure 6.7.: Current, voltage and magnetic field development for an exemplary quench. Due to a malfunction of the hall sensor the magnetic field value fluctuates. Please note that the time scales differ in the plots, as for the voltage logging a small time period, highly resolved, is depicted.

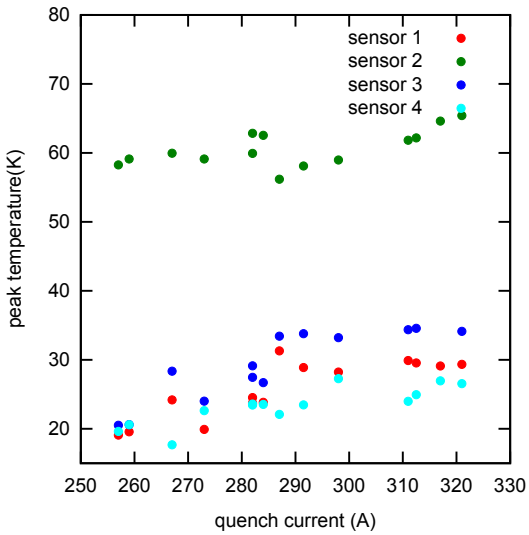

Figure 6.8.: Peak temperatures vs. quench current.

Looking at the quench voltage in figure 6.7, it is striking that the voltage reaches more than 50 V before the protection diodes parallel to the magnet open and prevent a further increase of the voltage. However, a forward voltage of 6-8 V for a single diode, thus 12-16 V for two in series, was expected. Hence, a separate, thorough measurement of the diode characteristics was performed after this thesis with a separate diode of the same type. [Sch12] The exposition to the magnetic field influences strongly the behavior of the diodes: The forward voltage increases from $\approx$ 7 V without magnetic field to about 25 V when the coil is powered with 320 A (see figure 6.9). For theses tests, the diode has been placed such that the magnetic field lines are dominantly orientated transversal to the diode (5.2 mT/A in transversal and 0,075 mT/A in parallel direction). For a coil current of 350 A, the transversal field is 1.8 T.

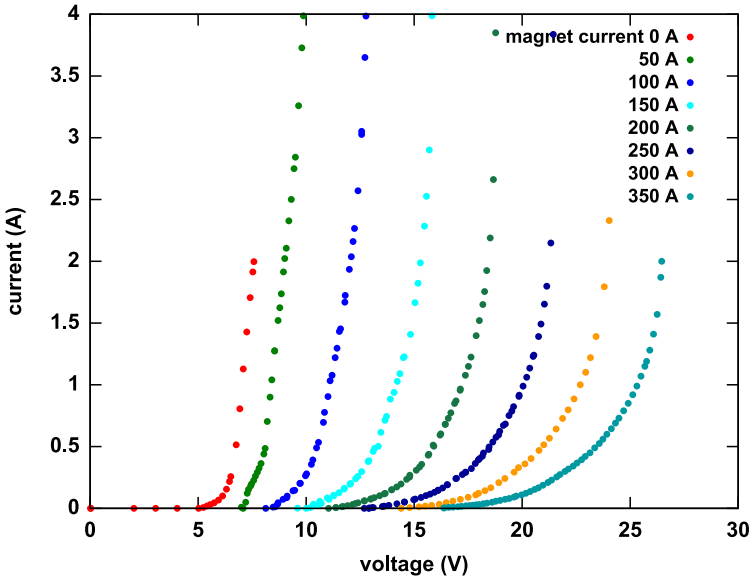

Figure 6.9.: Diode characteristic for different magnet currents i.e. magnetic flux.

6.3.3. Longterm test

The magnet was powered with nominal current of 291.5 A for 8 hours and 24 minutes without any incidences or remarkable effects. The temperature of the coil was not affected at all. The resistive current leads in the cryostat were cooled by gaseous helium boiling off from the liquid helium bath. Their temperature increased only slightly by a few K, which is not problematic.

6.3.4. Cycling

100 cycles from zero to nominal current of 291.5 A and down to zero again with a ramp rate of 3 A/s have been performed. The holding time at zero and maximum current was 7.6 s, so that the cycle time was in total 209.9 s. The actual current as well as the magnetic field is depicted in figure 6.10 exemplary for four cycles. The total temperature trend is depicted in figure 6.11, a

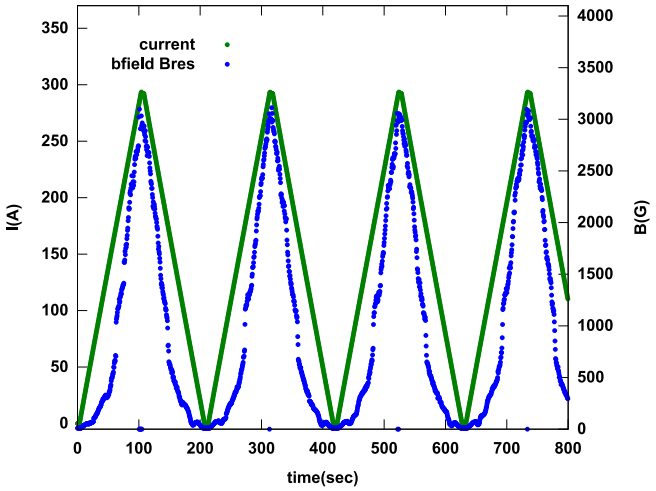

Figure 6.10.: Current and magnetic field during the cycle test. Due to a malfunction of the hall sensor, the magnetic field value is not proportional to the coil current.

close-up of the first 32 cycles in figure 6.12. Whereas the temperature of the current leads clearly mirrors the cycling, the coil temperature is not affected.

6.3.5. Ramp rate

Up to a current of 310 A, the coil was successfully ramped without holding points with ramp rates up to 8.5 A/s. Again, there is no effect on the coil temperature visible. The power supply does not allow for higher ramping speeds. The quench protection diodes - assuming a forward voltage of 6-8 V per diode - should have limited the ramp rate to 5 A/s. Thus, as already noticed from the quench voltage measurements, the forward voltage of the diodes is much higher than expected.

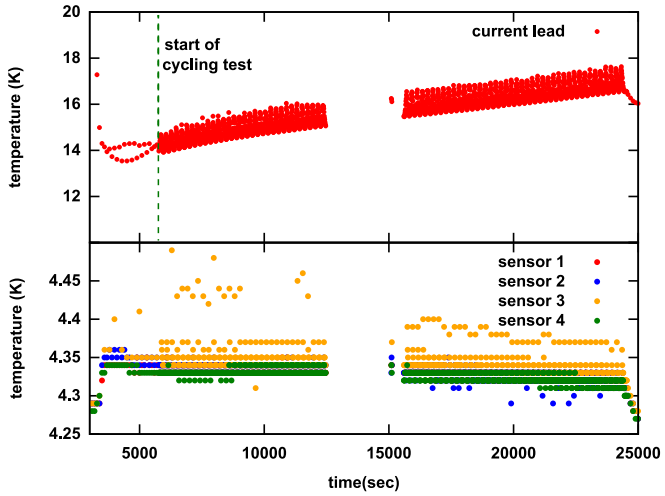

Figure 6.11.: Temperatures during complete cycling test. In the upper part the temperature of the current leads are depicted; the lower part shows the temperatures at the coil. In between some data is missing due to a crash of the slow control. The discrete jumping of the sensor reading in the lower part is due to the limited resolution of the measuring equipment.

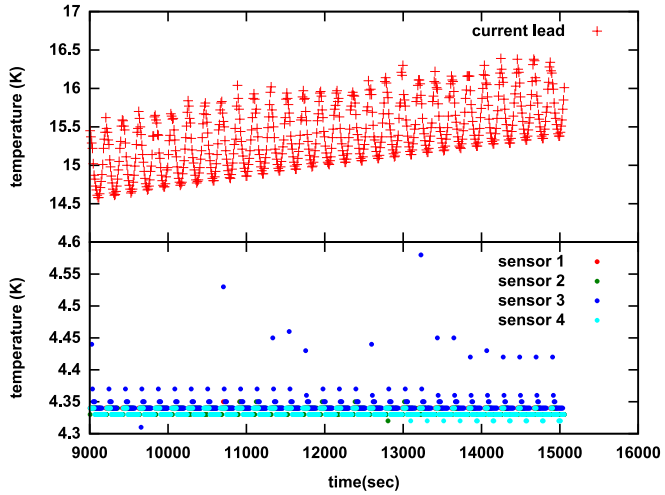

Figure 6.12.: Temperatures during the first 32 cycles. The discrete jumping of the sensor reading is due to the limited resolution of the measuring equipment.

6.3.6. Quench heater tests

The quench heater is fired by discharging capacitors with a capacitance of $C = 4400\,\mu\text{F}$, charged to U=178 V. The energy of $E = 1/2CU^2 = 69\,\text{J}$ is released within a short time span; the time constant of the discharging circuit is only $\tau = 0.45\,\text{ms}$. More details e.g. on the electrical scheme are given in [Sen11]. The heater can also be operated with a constant supply current introducing a permanent heat load onto the magnet. The load line of the magnet as well as the critical current I_c of NbTi for various temperatures is depicted in figure 6.14. The formula to calculate $I_c(B,T)$ is given in F. At the outer radius of the coil package, where the quench heater is placed, the magnetic field reaches about 3.5 T at nominal current (see figure 6.13). At this point, the superconductor turns normal conducting above 6.6 K.

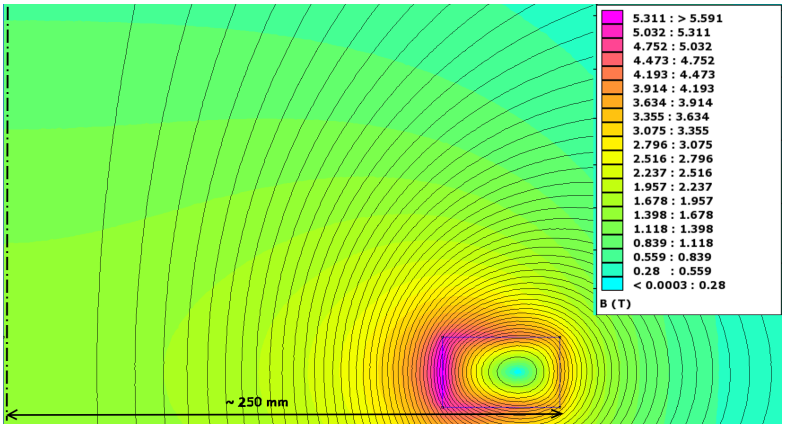

Figure 6.13.: Field map of the prototype magnet for the operating current of 291.5 A. A sectional view of the rz-plane is given. The blue line indicates the boundary of the coil winding package.

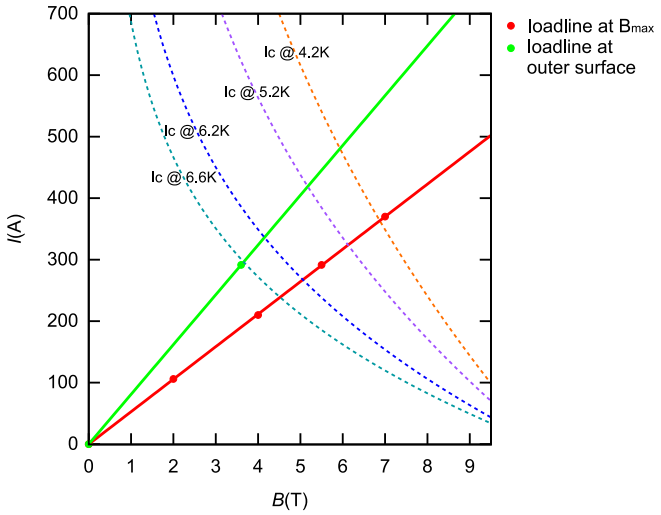

Figure 6.14.: Load line for the prototype magnet. In red the load line for the spot with the peak magnetic field is given, in green for the outer radius of the coil winding package. The limits of the superconductor are given for different temperatures in dashed lines.

Artificially induced quenches

The quench heater has been fired when the coil was powered with 50, 100, 200 and 292 A. Every time a quench was induced. The quench voltages and temperatures of the coil are depicted in figures 6.15 and 6.16. The lower the coil current is, the slower the quench seems to be: For small currents the voltage at the magnet does not reach the forward voltage of the protection diodes before the power supply is shut off. It is only 5V for a coil current of $I_{\text{coil}} = 50A$. Comparing to the spontaneous quenches during training it is striking that for the induced quenches sensor 4 instead of sensor 2 shows the highest temperature. Regarding again the better heat transportation along the circumference compared to the radial direction and the position of the heater band at the outer radius of the magnet, this temperature behavior is reasonable. The peak temperatures are generally smaller (see figure 6.17 compared to 6.8).

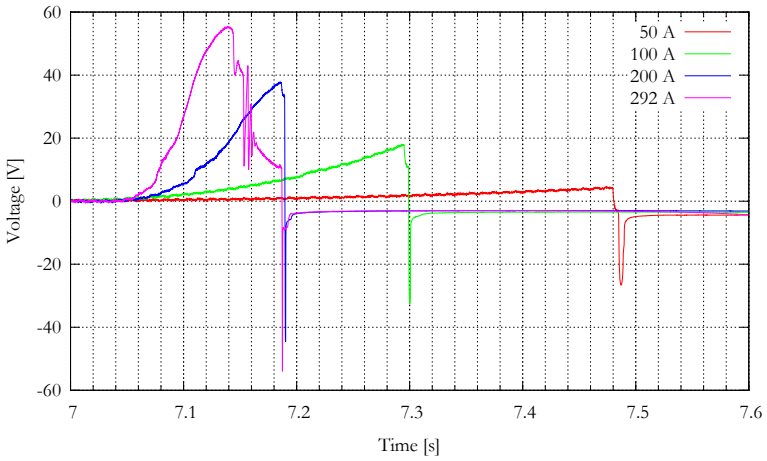

Figure 6.15.: Quench voltages at an induced quench for different coil currents. [Sen11]

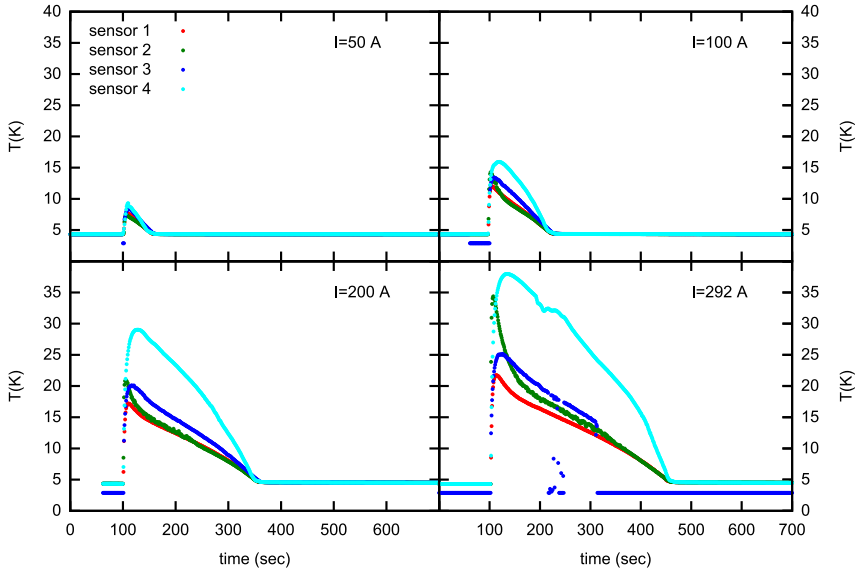

Figure 6.16.: Coil temperatures at an induced quench for different coil currents.

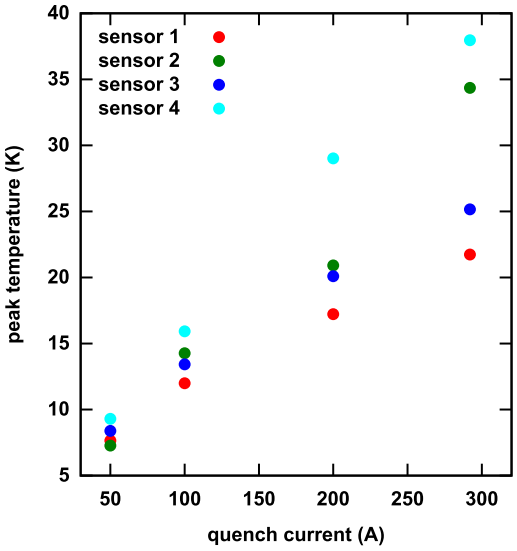

Figure 6.17.: Peak coil temperatures for the induced quenches.

Steady state operation

The quench heater can be used to increase the magnet temperature and thus decrease the temperature margin for the superconducting phase of the coil. Performing a rough estimation, Babcock Noel claimed that a steady supply current of 50 mA through the quench heater steel band would lead to a drastic increase of the coil temperature and a quench of the magnet. However, liquid helium cooling and a sophisticated model for heat transportation to and in the magnet were not considered. In dedicated test measurements, the coil itself was powered at nominal current. The applied heater current has been increased from 25 mA up to 400 mA in steps of 20 mA with holding times of approximately 200 s. Up to a current of 400 mA no significant temperature increase could be observed nor a quench was initialized. Thus, if quench heaters will be included into the quench protection concept, a thorough simulation and dedicated measurements are necessary to decide on the specifications of the heaters.

Simulations With the Solidworks simulation tools an estimative calculation has been performed to crosscheck the values from Babcock Noel and estimate the heat input needed to affect the coil temperature. A simplified coil model, depicted in figure 6.18, has been used in the simulation. For the stainless steel housing as well as the coil package the real dimensions in radial and axial

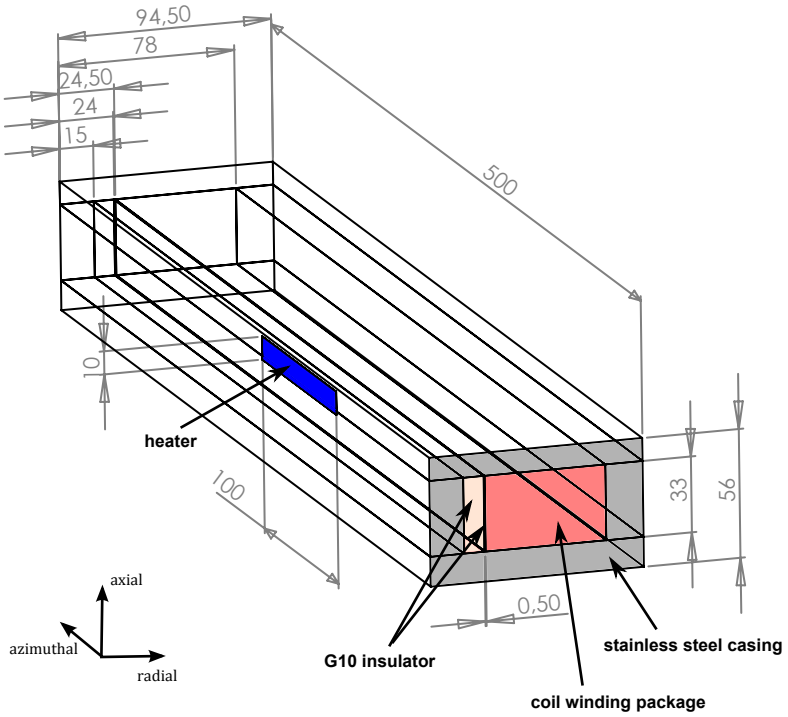

Figure 6.18.: Sketch of the model used to simulate the quench heater. Dimensions are in mm.

directions have been used. However, instead of modeling a full circular coil, just a straight box of 500 mm length has been implemented. At the side corresponding to the outer radius of the coil, the quench heater - a steel band with a thickness of 0.1 mm, 10 mm high and 100 mm long - is attached to the coil package separated by 0.5 mm G10 insulator (effective epoxy - glass fiber mixture). The heater is centered in height and azimuthal direction with respect to the coil package box. Additionally, 9 mm of G10 insulator fill the space up to the stainless steel housing in radial direction. Temperature dependent data for the heat conductivity of stainless steel, the G10 insulator material and the coil winding package has been taken either from NIST [M+00] or - in case of the coil windings - received from BNG [Ste11b]. For the latter, different heat conductivities in radial, azimuthal and axial direction have been used. The data is depicted in figure 6.19. The heat transfer coefficients at the boundaries between different materials have not been incorporated; thus an ideal heat transfer is considered in the simulation. To model the liquid helium bath, the outer surfaces in radial and axial direction have been set to 4.22 K. There is no boundary condition for the end plates in azimuthal direction. The steel band itself is the heat source in the simulation. In figures 6.20 and 6.21 the resulting temperature distributions for a heat input from 0.016 W (corresponding to a current of 400 mA) up to 60 W are given, respectively.

The peak temperature at the coil surface facing the quench heater for different heat inputs is

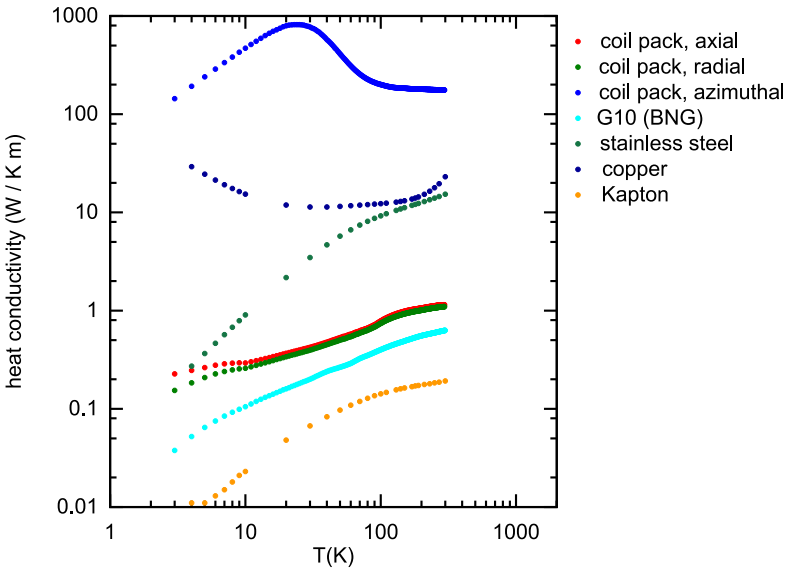

Figure 6.19.: Heat conductivities used in the quench heater simulation. For comparison also data for copper and Kapton is given.

depicted in figure 6.22. The rest of the coil should stay below this maximum. From figure 6.14, where the load line of the magnet and the critical current as a function of the magnetic field for different temperatures is depicted, it can be extracted that the magnet - when powered at nominal current - should not enter a normal resistive state below a peak temperature of 6.6 K. Thus, according to these estimations the coil should not quench, even when the heater is powered with 60 W. The tests showed that the coil quenches when the heater releases an energy of 69 J - even at much lower operating currents of the magnet down to $I_{\text{coil}} = 50\,\text{A}$. However, when firing the heater, the energy is released within a very short burst - the discharge time of the capacitors is only $\tau = 0.25\,\text{ms}$. Hence, the instantaneous heat input is by orders of magnitude higher. Assuming a constant energy release over 0.50 ms, it would be about 138 kW. Thus, a transient thermal analysis is necessary to simulate the correct behavior. Nevertheless, from the simulations it is obvious that

- with a heater supply current of 400 mA one is far from affecting the coil temperature,
- the temperature sensors which are embedded in the housing will not register a temperature increase before the coil quenches due to the efficient cooling through the stainless steel.

6.3.7. Conclusion

With the prototype magnet from Babcock Noell all nominal operation values could be reached and even exceeded; thus, the tests totally confirmed the coil design. It was shown that training needs to include temperature cycles to reduce the number of quenches, when ramping to nominal current after the experiment was at room temperatures. For PENeLOPE, with its 29 coils, this imposes long training phases. The CoTex2 test facility itself proved to be adequate for training all coils of PENeLOPE. Tests with the cryogenic high-power diodes showed that their characteristics change in strong magnetic fields. This, also has to be accounted for, when designing the

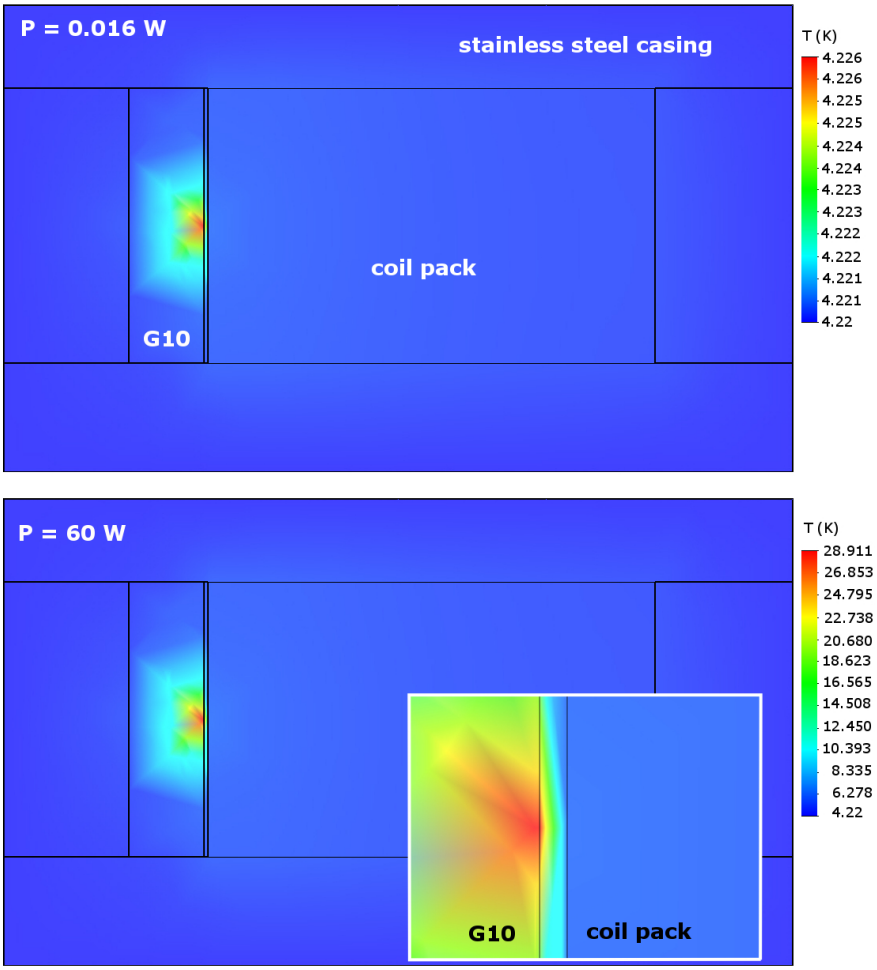

Figure 6.20.: Simulated temperature distribution in the magnet for a heat input of 0.016 W (top) and 60 W (bottom). Please note the different scale in temperature. A sectional view of the magnet is given. The small insert shows a zoom of the area around the heater for the scenario with a heat input of 60 W.

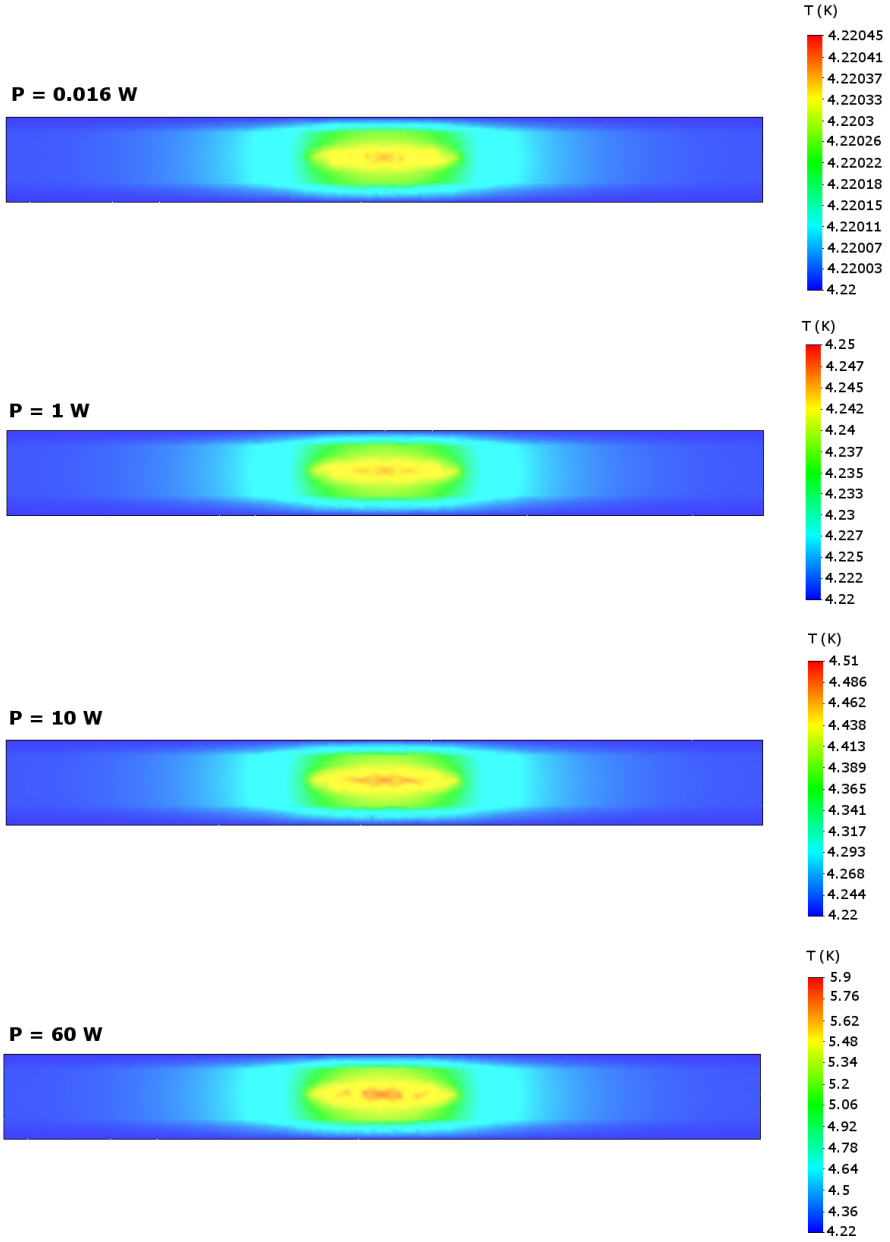

Figure 6.21.: Simulated temperature distribution on the coil surface facing the quench heater. From top to bottom, the heater is powered with 0.016 W, 1 W, 10 W and 60 W. Please note the different scales in temperature for the different scenarios.

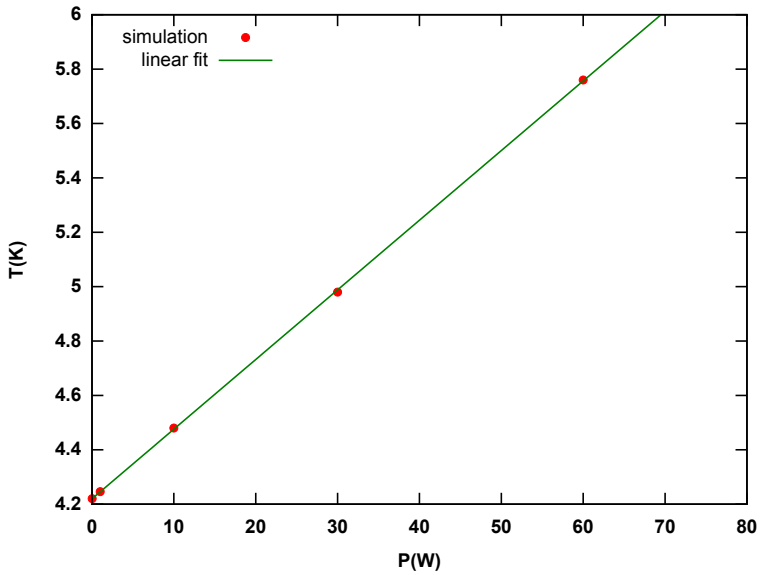

Figure 6.22.: Simulated peak temperature as a function of heat input through the quench heater.

quench protection system of PENeLOPE. When this system includes quench heaters, dedicated simulations and measurements on the energy input of the heaters to the magnet need to be performed, as rough calculations fail to estimate the correct effect of the heaters.

7. Microchannel plates for proton detection in PENeLOPE

7.1. Decay particle detection in PENeLOPE

7.1.1. Requirements

To determine the neutron lifetime via the detection of the decay particles, in principle, only reliable counting of these is needed. A detection efficiency highly stable in time is mandatory. The detection of both, electrons and protons, separately or in coincidence, can be used. The possibility of separating the decay electrons from the decay protons or having an electron blind proton detector, is not required. It will give, however, another handle for studies of systematic effects. The same holds true for energy or spatial resolution. The focus lies on proton detection as a larger extraction efficiency can be reached (see figure 3.3).
To detect the particles itself, several alternatives are studied in the PENeLOPE collaboration. The detector has to fulfill certain stringent criteria:

- **High voltage** As discussed in section 3.2, an electric field is needed for efficient extraction of the decay protons from the trap volume. Furthermore, depending on the choice of the detection principle, a post-acceleration of the low-energy protons from neutron decay might be favorable or even necessary for efficient detection. Both implies that the detector is to be set to negative high voltage, the cryostat being at ground potential. Whereas for the extraction only a voltage of $U_{\text{extr}} = -15\,\text{kV}$ is needed (cf. figure 3.3), the post-acceleration should be as large as possible: Even protons with 30 keV penetrate only a few hundred nm into material (cf. figure 7.1) and deposit only little energy in the detector or get even stuck in insensitive front layers without producing a signal. However, high-voltage installations are limited by technical feasibility. The electrons, having energies as large as 750 keV from the decay, are hardly affected by the additional electrical field.

- **Signal generation and amplification** Due to the low energy of the protons, the detector must not have any insensitive entrance layer. If a window is unavoidable, it should be as thin as possible to reduce the energy loss in this dead zone. Even a water layer building up at hygroscopic front surfaces has to be avoided. The tiny energy deposit requires a high intrinsic primary gain of the detector and at the same time a low noise level, to be able to clearly detect single protons while minimizing false counts.

- **Background** In addition to intrinsic noise source, external background has to be avoided. The PENeLOPE setup will be placed close to a neutron source, at a reactor or a particle accelerator; thus, the detector will be operated in high-radiation environment. Although being encapsulated inside the cryostat, it must be insensitive to neutron and γ-radiation. The importance of low background is discussed more detailedly in section 7.1.2.

- **Energy and spatial resolution** The distribution of the neutrons in the trap volume is given by their energies: different regions in the trap have different neutron energy populations. Energy dependent losses affect the storage time measured in different trap regions.

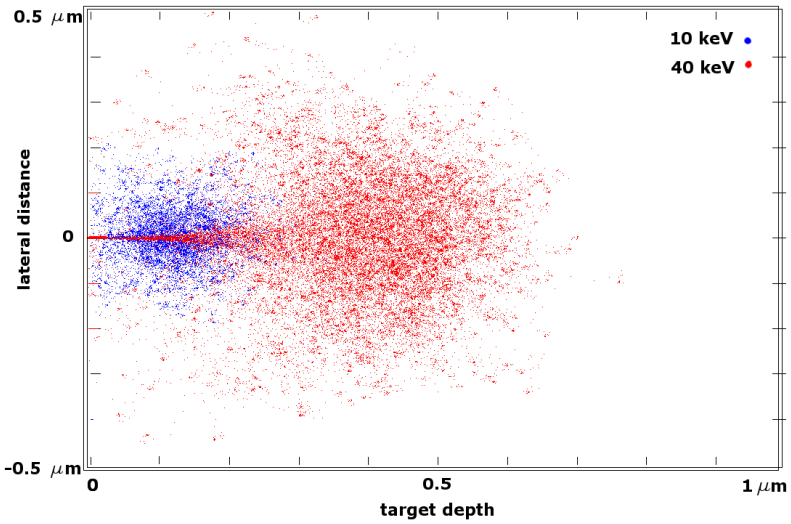

Figure 7.1.: Simulation of range of 1500 protons with 10 keV (blue) and 40 keV (red), respectively, impinging on CsI, a typical scintillator material, using the SRIM software. [JZ85]

Thus, probing the location of the neutron decay, could give an additional handle on systematic effects. The proton is guided from the location of the neutron decay to the detector by the magnetic field.
The proton energy is mainly dictated by the electrical potential the detector is set to - some tens of kV. If an additional extraction voltage along the trap will be applied (cf. section 3.2), the energy of the protons might differ by a few keV, depending on the height in the trap the neutron decay took place. The energy of the electrons from neutron decay is up to two orders of magnitude higher; the distribution being much wider. Resolving the spectrum will give minor information for the neutron lifetime measurements.

- **Count rate** Assuming a maximum number of neutrons in the trap of $8 \cdot 10^6$ [Sch11b], the decay-particle rate is expected to be up to $7 \cdot 10^5$ cnts/s. This rate distributes over the whole detector so that the rate load for a single channel (of a segmented detector) is reduced. On the level of the aspired precision of 10^{-4}, no rate dependend effects, such as pile-up or saturation in the electronics, are allowed, as they would introduce a false effect in the determination of the neutron lifetime from the count rate evolution.

Further restrictions are given, as the detector will be placed directly on top of the storage volume inside the cryostat:

- **Temperature** Facing directly the inner walls of the helium vessel, the detector needs to be operated at cryogenic temperatures to reduce heat input into the cryostat. Coupling the detector to the cryostat's radiation-shield cooling circle, will stabilize the detector at liquid nitrogen temperature. This implies according to the Stefan-Boltzmann law a heat input by thermal radiation to the helium vessel in the order of 0.6 W.[22] As this load goes with the fourth power of the temperature, a lower detector temperature would be favorable, but imposes larger restrictions on the detector design.

[22] Assuming the emissivity of 1 for a perfect black body surface.

- **Vacuum** Good vacuum conditions are needed for the storage of the UCN. To keep effects on the measured lifetime due to absorption or up-scattering of UCN on rest gas below $\Delta\tau = 0.1\,\mathrm{s}$, the vacuum has to better than $\approx 5 \cdot 10^{-8}\,\mathrm{mbar}$.[MP+09] Thus, the detector must be made of non-degassing materials. Although the helium cryostat acts as a big cryopump, the freezing of rest gas particles on its surface has to be minimized to keep its good neutron reflecting properties.

- **Magnetic field** A large magnetic field will exist close to the UCN trap volume. At the place of the particle detector the magnetic field will be $\approx 0.6\,\mathrm{T}$ with the field lines pointing upward, perpendicular to the detector's surface. This e.g. excludes standard photomultipliers for secondary light detection. Any detector having a drift of secondary electrons over a considerable distance (e.g. gas multiplication detectors) has to account for the deflection of the electrons by the magnetic field.

- **Dimensions** The detector should cover an area of $\approx 2300\,\mathrm{cm}^2$. In order to reduce the absolute magnetic field the detector is exposed to or to gain in distance for post-acceleration of the decay protons, the detector could be placed at a larger distance to the uppermost coil. However, the magnetic field lines will quickly fan out and - as the charged particles will follow the field lines - the area to be covered increases rapidly (compare figure 3.2). The installation of additional focusing coils has been thought of. [Pic08] The smaller size of the detector trades for the increased complexity of the whole system, the costs and the limited access to the storage volume due to additional superconducting coils.

7.1.2. Influence of background rate on the measuring time

In figure 7.2 simulation results for the time to reach a precision in the neutron lifetime measurement of $\Delta\tau_n = 0.1\,\mathrm{s}$ is plotted versus the background rate (external or intrinsic noise) in the proton detector. This is assumed to be constant in time, only modulated by statistical

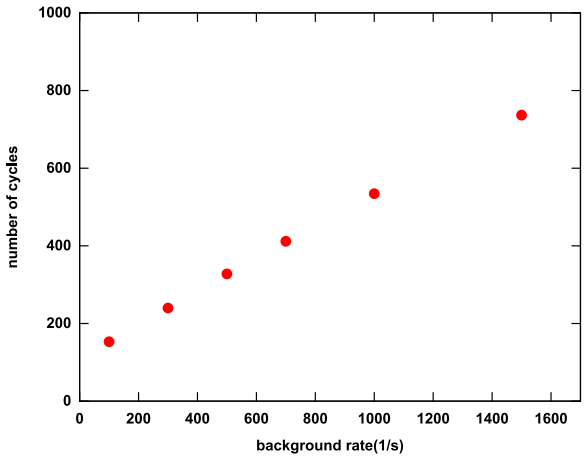

Figure 7.2.: Number of experimental cycles to reach a precision of $\Delta\tau_n = 0.1\,\mathrm{s}$ versus the background rate in the proton detector. For more details see text.

fluctuation. Moreover, it has been assumed in the simulation that every background event is misinterpreted as a proton signal. However, due to the different nature of the various noise

sources, this must not be the case (see also paragraph 'noise' in section 7.2.2). The neutron lifetime and its error is extracted from a fit to the exponential decay curve of time-resolved proton counting. A proton collection efficiency of 0.6 and a detection efficiency of 0.4 are assumed. The initial number of stored neutrons is $\approx 10^7$. The time is given in experimental cycles, where a cycle consists of four runs with storage times of 1000, 3000, 5000 and 8000 s. As can be seen in figure 7.2, a low background rate in the detector is very important to save experiment time, which is in turn needed for systematic studies.
The count rate evolution in a single storage phase is given in figure 7.3. In longer storage phases,

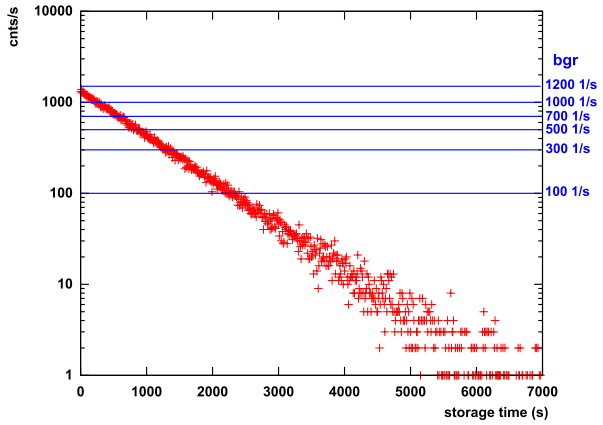

Figure 7.3.: Simulated proton count rate evolution during the storage phase. In red: proton count rate without background. In blue: background rates. Statistics of a single run.

the proton count rate drops below the background rate - the sooner the higher the background rate is. E.g. for a background rate of 500 cnts/s, already at a storage time of ≈ 1000 s the background counts exceed the proton counts. From this point of view, for the lifetime extraction very long storage phases can be discarded in favor of more statistics by repetition of runs with short storage times. However, the error of the lifetime $\Delta\tau$ extracted from a fit to the proton count rate evolution is very large, if the fit spans only a short storage time: In figure 7.4 $\Delta\tau$ is plotted versus the storage time for different background rates. Especially at lower storage times, the background rate strongly influences the error of the lifetime extracted from the fit. For longer storage times higher background rates have a minor impact. It is clear from the figure, that using storage times above 3000 s does not improve the error of the fit. Thus, short storage times with higher fit errors $\Delta\tau$ but time for more repetitions trade off against larger storage times with smaller $\Delta\tau$ but less time for gathering statistics. It has to be accounted for the fact, that an experimental cycle does not only consists of the storage phase, but that additional fixed time is needed for e.g. ramping up and down the magnet, filling of the neutrons and cleaning the neutron spectrum. A total of ≈ 1000 s has to be added to the storage time in every cycle.[23]
To find the optimum, in figure 7.5 the time needed to reach $\Delta\tau_n < 0.1$ s is plotted versus the storage time for various background rates. In contrats to figure 7.2, here, every data point gives the measuring time, when only runs with one specific storage time are repeated again and again,

[23] In the simulation, the following times were taken: Filling of neutrons 200 s, cleaning of the neutron spectrum 200, cleaning of wrongly polarized neutrons 160 s, ramping up or down 100 s, respectively, neutron counting time 200 s and waiting in between runs 200 s.

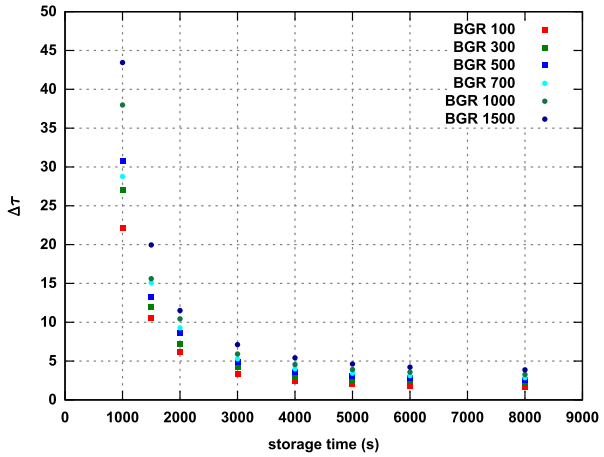

Figure 7.4.: The neutron lifetime extracted from a fit to the simulated proton count rate evolution (real protons + background) of a single run: its error is plotted versus the storage time the fit spans for various background rates.

assuming one specific background rate. τ_n is extracted from fits to the proton count rate solely. The experiment time is given in days and calculates from the number of runs needed to reach the precision goal times the total duration of one run (storage time plus fixed base time). The minimum measuring time is needed when using rather large storage times, the optimum not being very distinctive. The background rate strongly influences the time needed: for the optimum storage time of $\tau_{\mathrm{st}} = 6000\,\mathrm{s}$ a factor of 5.4 more time is needed for a background rate of 1500 s compared to 100 s (147 to 27 days).

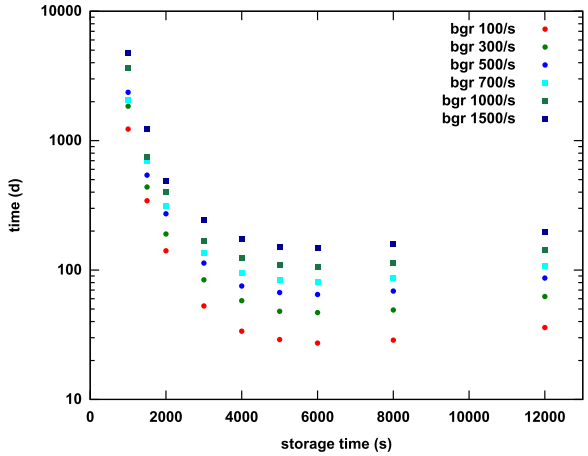

Figure 7.5.: Experiment time to reach $\Delta\tau < 0.1\,\mathrm{s}$ is plotted vs. the storage time for various background rates. Details are given in the text.

7.1.3. Possible detector solutions

Four candidates have been in closer contemplation:

- **Scintillator and photon detector** The detection of the decay protons with a scintillator followed by (large-area) avalanche photo-diodes (LAAPD) to collect the secondary light, has been extensively researched in the PENeLOPE group.[Tie09] Undoped Cesium iodide (CsI), has about the highest light yield at cryogenic temperatures compared to other standard scintillators. For protons it is 57 photons/keV, whereas e.g. it is only 0.8 photons/keV in plastic scintillators. [Tie09] In addition, it could be shown that the (LA)APDs not only operate down to $< 20\,\mathrm{K}$ but also benefit from a practically zero noise level at these temperatures. [Mül08] However, the sensitive area of the photo diodes is usually protected by a front layer, mostly epoxy. Thermal stress, when cooling down the APDs, leads to cracks in the epoxy and most likely to a damage of the APDs. Thus, the epoxy layer has either to be removed in acid, or custom-made window-free diodes have to be purchased.
  Further pros are the cost-effective and most efficient coverage of the detection plane with sensitive material.
  A serious downside is the poor signal generation of the assembly: CsI is hygroscopic and a water layer of 300 nm already reduces the sparse energy deposit in the scintillator by 50%. The light collection efficiency LC_E in the scintillator ($LC_E \approx 0.6$)[24] and the quantum efficiency of the APDs at the wavelength of the scintillation light ($Q_E \approx 0.45$) has to be considered, too. Thus, to maximize the light output, the protons should have energies of at least 40 keV. APDs with high intrinsic gain are mandatory to be able to detect few-photon events.
  Also the minimum ionizing decay electrons will deposit energy in the scintillator. A thin scintillation layer on a plastic light guide would effectively be electron blind; however, the light transport in this geometry is much less efficient ($LC_E < 0.3$) compared to a thick piece of pure CsI. Hence, in favor of a larger protons signal, a thick scintillator is preferred. Here, 700 keV electrons will produce $4 \cdot 10^4$ photons in the CsI; a few thousand photons are generated in a plastic scintillator. Thus, in both cases a signal clearly detectable is generated.

- **Avalanche photo diodes** The protons can also be detected directly by APDs, avoiding problems with inefficient light production, collection and detection. Amplifications of $10^4 - 10^5$ are possible; energy resolution gives a (limited) possibility to distinguish between electrons and protons. As already mentioned, noise is minimized at low-temperatures, resulting in an excellent signal-to-noise ratio. Typical sizes of large area APDs are only in the order of $1\,\mathrm{cm}^2$, so that more than 2000 pieces would be needed to cover the detector plane. As also the costs for the read out electronics scales with the number of channels, the complete PENeLOPE detector would make up a large part of the experiment budget: the full costs are expected to be up to 500 000 EURO. [Tie12]

- **Gaseous electron multiplier** A gas-filled multi-wire chamber can be used to detect the protons. [Sch11a] As with scintillators, large areas can be covered easily and cheap. The gas amplification of the secondary electrons provides a large signal. However, only few counter gases are suitable at cryogenic temperatures: Neon is a candidate as it has a condensation temperature of only 27 K and a high electron yield with 56 generated electrons per cm path length.[25] The spiral drift of the secondary electrons in the magnetic field is not expected

[24] Simulation results for a trapezoidal piece of pure CsI, 3 mm thick, read out from the side. [Tie09]
[25] Stopping power for protons with some tens of keV in Neon is a few MeV cm^2/g. [MBC05] The energy needed to create an ion-electron pair is 37 eV.

to be problematic for signal generation.
The protons can either be detected directly in the gas filled chamber or be directed onto a foil, where they generate secondary electrons, which are subsequently detected in the wire chamber. Protons of a few tens of keV, impinging onto a thin LiF coated polyimide foil, produce of the order of ten secondary electrons. [H$^+$06] These electrons could be accelerated before entering the counter, where they would deposit more energy than the primary proton.
Direct proton detection requires the entrance window of the chamber to be as thin as possible. At the same time, it must be stable enough to withstand the pressure difference between the chamber ($\approx$ 100mbar) and the high vacuum of the neutron storage volume. Using thin foils, gas diffusion through the foil is a limiting factor for its thickness.
An 10x10 cm^2 large, 100 nm thin polyimide foil, supported by a nickel mesh with a pitch of 0.8 mm could be produced by the PENeLOPE group. However, reliable production of stable, large foils withstanding cryogenic temperatures is challenging. Moreover, the gas diffusion through these thin films is most likely too high.
Proton and electron discrimination would be possible by two separated, successive detection volumes: In the first detection volume the protons are counted. This is transmissive for the fast electrons, which generate additionally a signal in the second detection volume. The protons or the low energetic electrons from proton conversion, however, can not reach this second stage.

- **Microchannel plates** Microchannel plates are widely used single-ion detectors. They will be discussed in detail in the following.

7.2. Microchannel plates - basics and performance

7.2.1. Detection principle

Microchannel plate detectors (MCP) are thin plates (thickness about 0.5 mm) usually made of highly resistive lead glass, penetrated by a regular array of tiny channels with a diameter of $\approx 10\,\mu$m and a spacing of about $12\,\mu$m (see figure 7.6). Between the front and the back surface of the plate a voltage of the order of 1000 V is applied, so that every channel turns into an individual continuous-dynode electron multiplier. Impinging photons or charged particles start a cascade of electrons that propagates through the channel, amplifying the original signal. To this end the channels are slightly tilted ($\approx 10°$) with respect to the surface and therewith the electric field lines, guaranteeing the primary particle as well as the secondary electrons to hit the channel walls. The electron cloud leaving the plate is in the simplest case collected by a (segmented) metal anode. To increase the gain, two (or more) plates can be stacked, so that the electrons exiting the first plate trigger an avalanche in the next plate (see figure 7.7). Gains of 10^7 to 10^8 are reached that way. Ion-backflow is suppressed by orientating the plates so that their channels are mirror-inverted - the so called chevron configuration. In figure 7.7, left side, the pulse height distributions of single and stacked MCPs are depicted. At least a two plate sandwich is needed to generate a peaked signal distribution and to allow for particle counting.
Typically, MCPs are circular with diameters between 18 and 50 mm. Rectangular or trapezoidal plates can be produced as well. The size is in principle limited only by manageability and stability of the thin, highly fragile plates.
The handling of microchannel plates requires certain cautiousness: They should be stored under clean-room conditions; for operation, high-vacuum ($< 10^{-5}$ mbar) is needed. MCPs are hygroscopic, but can be vacuum-baked at temperatures around 250° to remove adsorbed water.

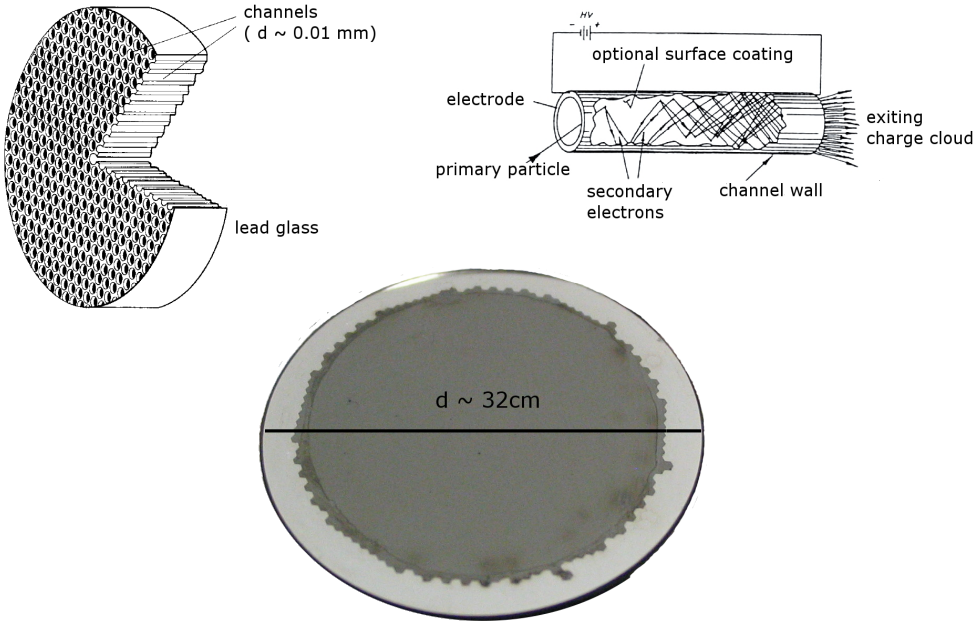

Figure 7.6.: Microchannel plate principle: in the upper left a cut-away sketch of a single plate is given. In the upper right, the signal generation is schematically depicted. The schematics are adapted from [Wiz79] and [Ham94]. A photo of a complete plate is given on the bottom.

A broad review about MCPs is given in [Wiz79] and a more technical survey in [Ham94].

7.2.2. Performance

Particle detection efficiencies The detection probability for particles is determined by the electron yield of the primary particles impinging onto the channel wall. In case of protons, the yield g increases with the energy, reaches a maximum of $g \approx 5$ at 70 keV and decreases again. At 20 keV it is $g \approx 2.7$.[Z+85, Fra02, Ste57] Once an electron is released, the strong electric field along the channel will generate a signal. The absolute detection efficiency is limited by the open area ratio (OAR), i.e. the fraction of the plates front surface covered by holes, as particles hitting inter-channel sections will not trigger an electron avalanche. The OAR is about 60%.[26] For singly charged ions, especially protons, [G+84, O+97, PS00] report efficiencies equal to the OAR above ion energies of $\approx 2.5 - 3$keV (see also figure 7.8). The detection efficiency for electrons depends heavily on the energy range (see figure 7.8): 0.6 to 0.8 for 10-100 keV electrons is stated by [B+86], whereas [Res80] gives an efficiency < 0.5 for energies of 8-28 keV with the tendency to decrease for higher energies in the examined range. The efficiency, shown in figure 7.8, increases slightly above 50 keV. This is explained by [B+86] with the primary electron having enough energy to traverse the inter-channel material (a few μm) and releasing secondary

[26] Electrons released by the primary particle impinging on the inter-channel web can be redirected into the channels by an additional electric field. This is generated by a mesh in front of the plate which is set on high negative voltage with respect to the entrance surface of the plate. The detection efficiency can therewith be increased above the OAR. [F+95]

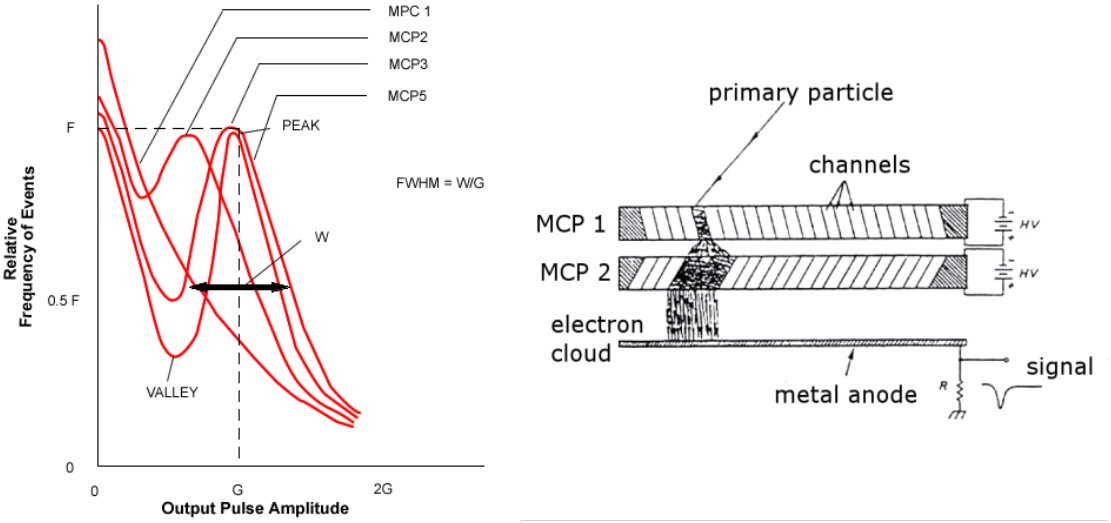

Figure 7.7.: Left: Schematic pulse height distribution for various MCP configurations. [Ltd11] Right: sketch of a chevron type MCP stack. [Wiz79]

electrons in more than one channel. The overall lower detection efficiency compared to that for protons is due to the small secondary electron yield of only < 0.5 electrons per incident particle for primary electrons with energies above 10 keV. [Her87] As the electrons energy loss by ionization decreases with increasing energy, the electron yield and thus the detection efficiency is expected to be low for electrons with energies of a few hundred keV.
The channel plates are practically blind for hard x-ray or gamma radiation. Table 7.1 summarizes detection efficiencies collected by [Sch74] for various particles and energy ranges.

particle	**energy/wavelength**	**detection efficiency**
electrons	4 - 100 keV	0.6-0.1
ions (H+,He+,A+)	2 - 50 keV	0.6-0.85
U.V. radiation	300 - 1100 Å	0.05-0.15
soft X-rays	2 - 50 Å	0.05-0.15
hard X-rays	0.12 - 0.2 Å	0.01

Table 7.1.: MCP detection efficiencies for various particles and energy ranges. [Sch74]

Energy resolution The energy resolution is determined by the (energy dependend) electron yield distribution, when the primary particle hits the channel wall. The supply voltage must be below the limit for saturation of the electron cascade: beyond this point, due to the resistivity of the plate and the limited strip current[27], the channel wall becomes unable to further supply electrons to the avalanche. [Sou71] The output signal is then independent from the number of electrons released by the primary particle initiating the cascade.
Below saturation, the signal height, i.e. the total charge in the avalanche pulse, depends on the

[27] The strip current is the current that flows along the channel walls when a voltage is applied to the plate.

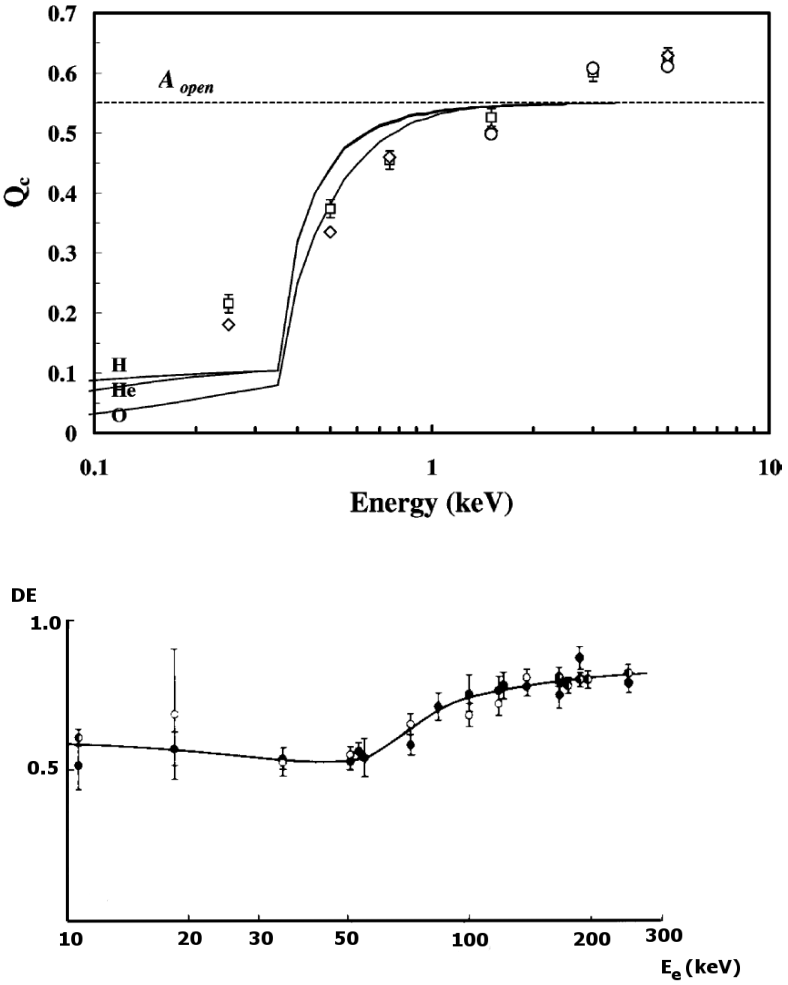

Figure 7.8.: Top: Measured absolute ion detection efficiencies for O^+ (circles), He^+ (diamonds) and H^+ (squares). Calculations are given by solid lines. The open area ratio is given by the dashed line. [Fra02] Bottom: Detection efficiency for electrons from [B+86]. Full and open circles are results determined with two different calibration methods.

position along the MCP channel at which the avalanche was initiated (the deeper the primary point of impact the lower the accelerating voltage and the shorter the remaining path) and the number of secondary electrons that initiated the avalanche. The resolution is smeared out by the statistical characteristics of the electron yield from the primary particle as well as in the avalanche process, which, both, follow approximately a Poisson distribution.
In figure 7.9 the energy resolution for positive ions is depicted. The electron yield for protons

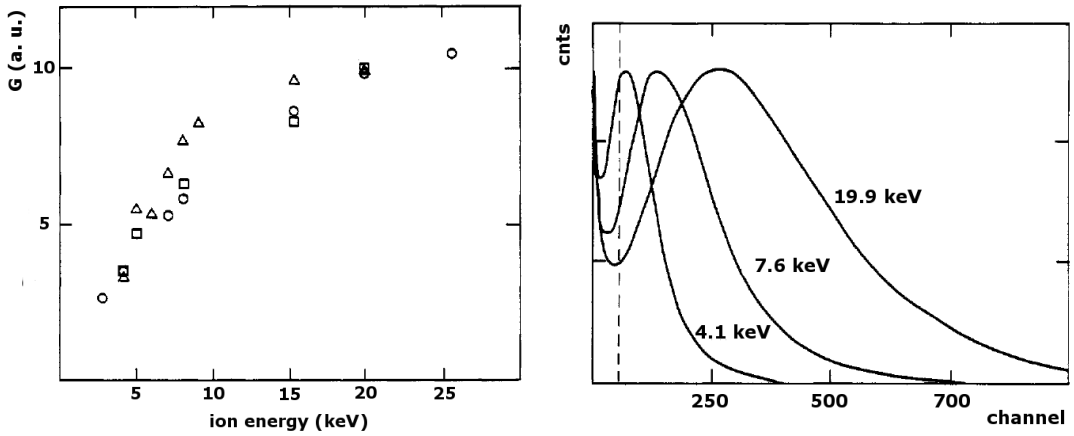

Figure 7.9.: Left: Average gain $\bar{G}$ as a function of ion energy for He^+ (triangles), Ne^+ (squares) and Ar^+ (circles). Right: Signal height distribution for Ar^+ with different energies. [H+85]

increases steeply up to 30 keV, thereafter reaching a plateau with a maximum of about five electrons/ion at around 70 keV and slowly going down again for higher energies. [Z+85, Fra02] The energy resolution of the MCPs will therefore most probably not suffice to distinguish between differences of a few keV at the level of 30-40 keV, as needed in PENeLOPE.

Particle discrimination To distinguish between electrons and protons is also only possible - if at all - when the MCP is operated below the saturation voltage. The large difference in the secondary electron yield of protons compared to electrons then leads to different pulse heights. Whereas the protons have a fixed energy given by the extraction and post-acceleration voltage, the electron energy spans a wide range from 0 to 780 keV. The secondary-electron yield is largely varying in this range as stated above. Electrons at the end of the range will hardly be detected, whereas very low-energetic electrons will produce a signal of the order of the proton signal. Therefore, there will only be limited possibility to distinguish electrons from protons.

Noise The typical dark count rate of microchannel plates at room temperature and good vacuum conditions is of the order of 0.3-1 cnts/s/cm^2. With a detector size in PENeLOPE of $\approx 2300\,\mathrm{cm}^2$, the noise sums up to about 700-2300 cnts/s. Possible intrinsic noise sources are

- Thermal emission of electrons from the channel walls. As lead glass has a relatively high work function[28], this noise contribution is already reduced to a very low level.
- Electric field emission from channel walls and local discharge at high electric peak fields. The latter can be minimized by a careful design of the detector. Also dust particles can

[28] The work function describes the minimum energy needed to release an electron from a solid.

trigger discharges, so that, like in every high voltage application, a dust-free and clean environment has to be guaranteed.

- Ionization of residual gas. Operating the detector at a vacuum better than 10^{-5} mbar is mandatory.
- Radioactive-isotope content of the lead glass.

Whereas the noise contribution from thermal emission of electrons in the channels, already low at room temperature, vanishes when going to cryogenic temperatures, the other sources are not affected by temperature. The noise from ionization of residual gas is minimized by a good vacuum: the outgassing of the plates is quite large due to their big internal surface, resulting in a long time ($\approx 1\,\mathrm{d}$) to reach a constant noise level. [F+87] The main part of the dark current is generated by the radioactive decay of the contents of the lead glass. [F+87] As the decays are randomly distributed along the channel, the pulse height distribution of these events follows an exponential decrease. Special low-noise glasses with a reduced content of radioactive isotopes are available, having about a factor of three lower dark counts. [JL97]

Rate capability and cryogenic temperatures The MCP produces a very fast signal with a typical full-width at half maximum (FWHM) of the order of 500 ps. However, the large ohmic resistivity of the plate material leads to limitations in count rate capabilities: the supply of electrons to the avalanche initiated by the primary particle is hindered. If the electrons are not supplied fast enough, the avalanche runs into saturation, the voltage over the plate will break down and thus the gain decreases. This effect becomes evident especially at high count rates above 1000 cnts/s. Due to the temperature dependence of the plate resistivity, the problem is aggravated at cryogenic temperatures: the resistance of the bulk material will increase exponentially with decreasing temperature as depicted in figure 7.10, left side. The measurements, performed with only small voltages in the order of 10-30 V applied to a single plate, suggest a resistance change of $T_{293\,\mathrm{K}}/T_{<20\,\mathrm{K}} \approx 1.0 \cdot 10^6$. In contrast, [S+92] and [R+07], report ratios of the order of only $2 - 5 \cdot 10^3$ using a Z-stack and chevron configuration with 900 V per plate, respectively. On the right hand side in figure 7.10, the count rate - gain dependency at various temperatures is depicted. At 41 K degradation starts at a count rate of $\approx 10^4$ cnts/s, at 18 K already at 10^3 cnts/s. In PENeLOPE, about $7 \cdot 10^5$ cnts/s are expected in total. Assuming a coverage of the detector plane with about 150 separate MCP chevron stacks (see also table 7.5), the rate for one of these is expected to be of the order of 5000 cnts/s at most. Thus, performance degradation at low temperatures is possible using MCPs in PENeLOPE. Most probably, however, the detector will have only $\approx 70\,\mathrm{K}$. Additionally, special low-resistance plates - so called ESR plates - exist, which have factor of 10-100 lower resistance at room temperatures. Also, [RF00] used one of these plates with only $R = 4.6\mathrm{M}\Omega$ for the measurements cited in figure 7.10.

Magnetic field A magnetic field can affect the detection efficiency of microchannel plates, although the effect is expected to be small at moderate field strengths. The secondary electrons in the avalanche process spiral around the field lines, while being accelerated by the electric field along the channel. At higher magnetic fields the path length between collisions of the electrons with the channel wall decreases, therewith the acceleration path and thus the impact energy of the electrons. This in turn leads to a reduced electron yield. The degradation, however, can be compensated by applying a higher electric field. [M+88] In figure 7.11, the MCP detection efficiency as a function of the magnetic field strength is depicted. At the detector position in PENeLOPE a field of $B \approx 0.6\,\mathrm{T}$ is present, oriented perpendicular to the detector plane. A decrease of the efficiency is therefore not expected.

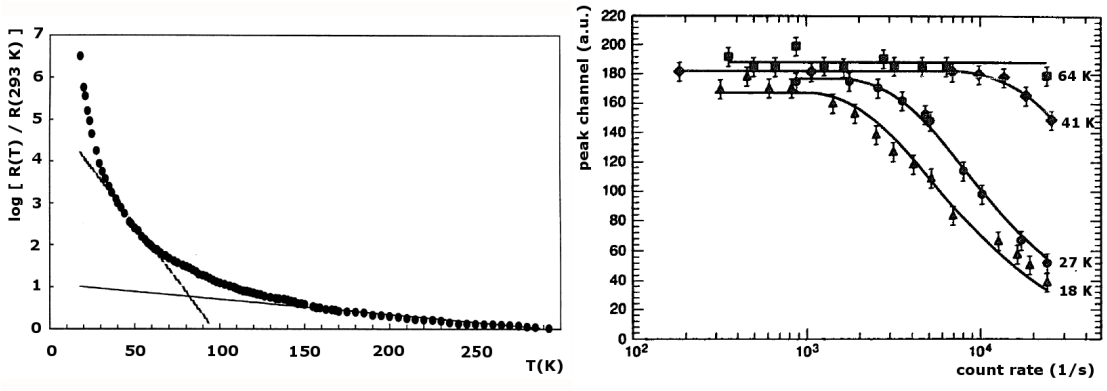

Figure 7.10.: Left: Resistivity vs. temperature in a semi-logarithmic scale. The solid lines represent partial exponential fits to the data. [RF00] Right: Gain (represented by the peak channel of the pulse height distribution) is given as a function of the count rate for temperatures of 64 K (squares), 41 K (diamonds), 27 K (circles) and 18 K (triangles). [S+92]

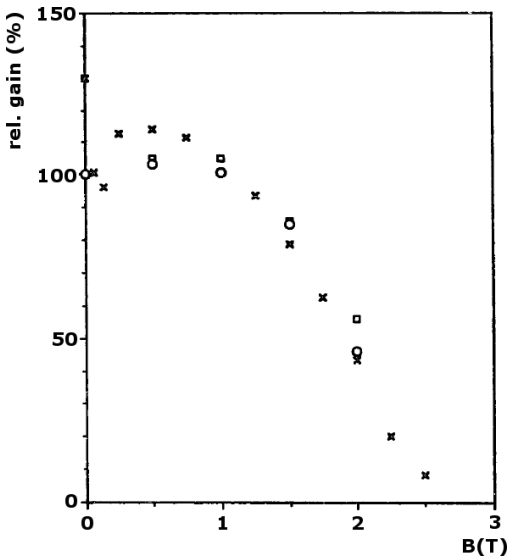

Figure 7.11.: Effect of the magnetic field on the detection efficiency of microchannel plates. The field is oriented perpendicular to the plate surface. Measurements have been performed at a temperature of 14 K and with $5.8 \cdot 10^4$ cnts/s (x), at 14 K and with $3.8 \cdot 10^4$ cnts/s (□) as well as at 25 K and $3.8 \cdot 10^4$ cnts/s (○). [S+92]

7.3. Microchannel plates for PENeLOPE

To explore the possible use of a microchannel plate detector in PENeLOPE, a two-fold approach has been taken: On the one hand the characteristics of a commercial chevron type detector from Hamamatsu has been explored. On the other hand, bare plates have been purchased for which the support structure was developed, thus having a more flexible prototype and gaining experience for the design of the complete PENeLOPE proton detector. Tests were performed with a radioactive α source and at the proton detector test facility PAFF [MH+07].

7.3.1. Hamamatsu detector

The specifications of the chevron-type microchannel plate detector, model F4655 from Hamamatsu, are summarized in table 7.2. The detector has a stainless steel support with insulating ceramic spacers. The charge signal is collected on a single, non-segmented copper anode. Signal and power cables are screwed to contact pins on the detector. A picture as well as a schematic top view is given in figure 7.12.

property	**value**
effective area diameter (mm)	14.5
open area ratio	60 %
distance of plates (mm)	0.1
distance of backplate to anode (mm)	1
bias angle of channels	12°
channel diameter (μm)	12
ratio of channel length to diameter L/D	60:1
max. supply voltage between MCP in and MCP out (kV)	2.5
max. voltage between MCP out and anode (kV)	0.5
gain	$5 \cdot 10^7$
resistance (MΩ)	70.6
dark counts (cnts/s/cm^2)	0.38

Table 7.2.: Specifications of the Hamamatsu MCP detector F4655. [Ham09]

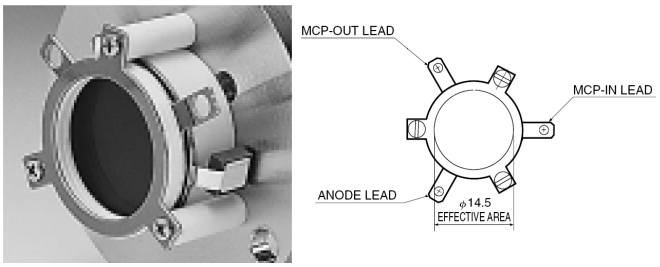

Figure 7.12.: Hamamatsu F4655 MCP detector.

7.3.2. Bare channel plates

Resistance matched pairs of channel plates for chevron configuration have been purchased from Tectra and Photonis, respectively. The plates are, with a total diameter of 32 mm, larger than the plates of the Hamamatsu detector F4655 but have similar characteristics (see table 7.3).

property	**Photonis**	**Tectra**
Effective area diameter (mm)	25	26
Open-area ratio	66 %	60 %
Bias angle of channels	12°	
Channel diameter (μm)	10	
Ratio of channel length to diameter L/D	40:1	
Gain single plates individually at 1000 V	$2.4 \cdot 10^7$ -	- 9167, 9500
Resistance (MΩ)	110	107
Dark counts (cnts/s/cm^2) Dark current [29] (A/cm^2)	0.3 -	- $0.3 \cdot 10^{-12}$

Table 7.3.: Specifications of the bare microchannel plates for PENeLOPE detector tests.

7.3.3. Support for bare plates

The support of the bare plates was designed following standard chevron detector geometries (see figure 7.13). Design demands were on the one hand being able to set the detector front on

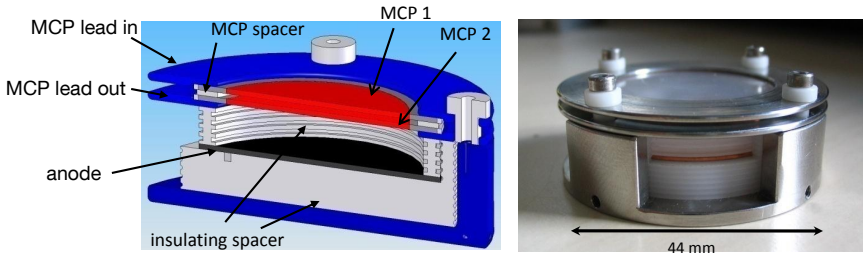

Figure 7.13.: Self made MCP detector, version I. In the picture, the MCPs have been replaced by glass plates.

high negative voltage while having the read out part, including the anode, on ground potential. Therefore, the flexibility to vary the distance between the back plate and the anode had to be assured. Secondly, the detector needs to be cooled down to cryogenic temperatures: the complete housing is made of stainless steel having a direct thermally conductive contact between the back

[29] The dark current can not be transferred easily into dark counts. For this, the gain has to be known, which is dependent on the voltage applied. The dark count events will not only occur at the front side of the MCP, so that not the complete voltage, thus not the full gain, will take effect and a mean gain has to be assumed. Additionally, trigger settings of the acquisiton electronics have to be accounted for. Guessing a gain of 10^7 the dark current of $0.3\,\mathrm{A/cm^2} = 0.3/1.9 \cdot 10^7\,\mathrm{e/s/cm^2}$ corresponds to a dark count rate of $0.16\,\mathrm{cnts/s/cm^2}$. However, this estimation is purely speculative.

of the housing and the MCP lead-out, therewith the MCPs. Thus, the plates can be cooled, when the detector assembly is mounted to a cold head. Supply voltage is fed to the lead-in and lead-out plates which have electrical contact to the channel plates. A copper spacer ring, 0.6 mm thick, provides contact between the MCPs themselves. Using the ohmic resistance of the plates, a voltage divider is created and the front side of the second MCP is at the same potential as the back of the first MCP. The copper anode remains on ground. As the housing is on the same potential as the MCP lead-out, insulating spacers are needed around the anode plate. Its distance to the second MCP can be varied, by adjusting the thickness of the insulating spacer rings. For the prototype support, the insulators are made of Delrin, i.e. polyoxymethylene, called POM, a thermoplastic with large resistance, but, compared to ceramics, poor vacuum properties and a disfavorable thermal expansion coefficient. To have the flexibility to also adjust the distance between the channel plates, a redesign of the support was carried out, as depicted in figure 7.14. This enables the option to introduce two additional contacts between the channel plates, electrically separated from each other; thus, a voltage difference between the back of the first MCP and the front of the second MCP can be applied. This can lead to a narrower pulse height distribution; for details see section 7.3.10. At the same time, a further downside of the

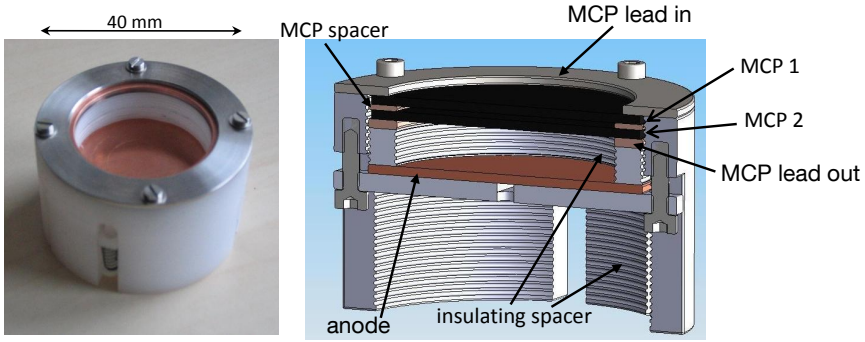

Figure 7.14.: Self made MCP detector, version II.

first detector version is eliminated: the screws which keep the stack of channel plates as well as lead-in and lead-out plates together are on the same potential as the lead-out (cf. figure 7.13). However, they protrude the lead-in, which has a different electrical potential; hence, the front surface of the detector does not have a homogeneous potential distribution, which might possibly distort the electrical field at the entrance of the channels. In the redesign, all parts facing the incoming particles are at the same electrical potential. However, the possibility to mount the detector to the cold head was omitted in favor of a lighter support, easier handling and a better connection of voltage supply and signal cables.
Regarding the high voltage application, special care has to be taken in the design of the support. All metal parts were electro-polished to smoothen sharp edges and avoid electric field peaks at high voltages. Discharges on the plates locally destroy the channel structure, as can be exemplarily seen in figure 7.15. The detector is still operational but inactive in this damaged region.

High voltage supply Using glass plates instead of the channel plates, high voltage capabilities of the detector support (version I) were explored. While the lead-out was kept at constant

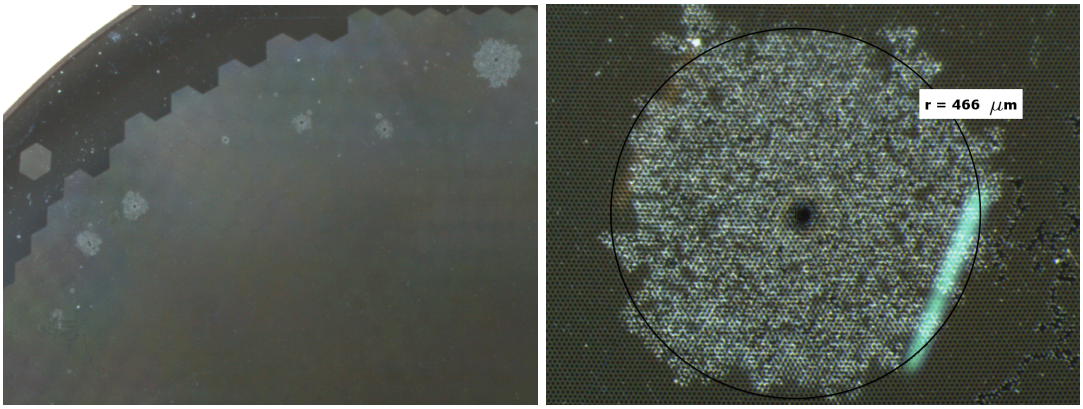

Figure 7.15.: Destruction of channel structure by discharges. Left, a section of the plates showing several of the discharge holes: They are located close to the rim, where the metal anodes are positioned. Right, a close up of a destroyed area: The black circle with a radius of 466 μm has been added as a scale. The large, faint blue stripe is a light reflection.

voltage ($U_{\text{lout}} = 400V$), the lead-in could be tuned up to 3.3 kV, $\Delta U = 2.9\,\text{kV}$, before sparkovers occured between the MCP spacer and one of the lead anodes. The Hamamatsu detector allows for $\Delta U = 2.5\,\text{kV}$. However, for the MCP operation only $\Delta U = 2.4\,\text{kV}$ are needed - the gain being already in saturation.
Keeping the voltage between the plates fixed at $\Delta U = 2.4\,\text{kV}$ and the anode at ground potential, up to $U_{\text{lin}} = 6.4\,\text{kV}$ could be applied to the detector front. Discharges occurred between the anode and the side structure which is at the same potential as the lead-out ($U_{\text{lout}} = 4\,\text{kV}$). Protecting these side supports with insulating Kapton foil, the voltage could be further increased to $U_{\text{lout}} = 6.3\,\text{kV}$. Thereafter, sparkovers between the anode and the ground plate were initiated. The Hamamatsu detector is specified for $\Delta U = 0.5\,\text{kV}$ between the anode and the lead-out.
Furthermore, applying high voltage to the detector assembled with the channel plates, revealed that stabilization resistances between the lead-in as well as lead-out and ground, respectively, are needed (see figure 7.17, left side). Otherwise, due to the ohmic resistance of the plates, the potential of the lead-out is pulled up while increasing the voltage at the lead-in. The stabilization resistances should be low compared to the plate resistance, but as large as possible to minimize the input bias current; $R \approx 8\text{M}\Omega$ was chosen.

7.3.4. Plate resistance

Applying a voltage across the detector and measuring the bias current allows to determine the total effective ohmic resistance R of the plate configuration. In the left part of figure 7.16 the measured characteristic curve of the Hamamatsu chevron detector is depicted. A linear fit to the data points gives

$$\text{slope}\, m = 0.01148 \pm 3 \cdot 10^{-5},$$

$$\text{abscissa}\, b = -0.07 \pm 0.09$$

and thus a resistance of $R = \frac{1}{a} \approx 90\text{M}\Omega$. The resistance is specified with 70.6MΩ. Despite the mismatch of 28%, the characteristic curve is notably non-linear. Measuring the current at a fixed

voltage over a longer time period (cf. figure 7.16 right part) reveals an increase of the current, thus a decrease of the plate resistance with time (9% in 40 min). This effect has been observed

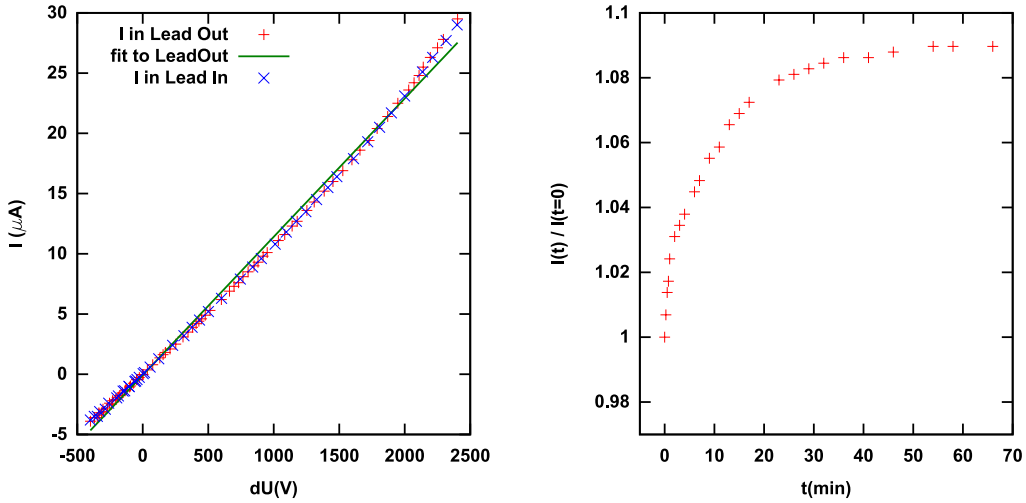

Figure 7.16.: Left: Characteristic curve of the Hamamatsu chevron detector. The bias current has been measured in the power line lead-in as well as in lead-out. Right: Time-evolution of the MCP current at a fixed bias voltage of 2100 V.

before ([P+87, S+85]) and is attributed to the change of temperature of the channel plates due to ohmic heating. Changes in the plate's resistance can affect the bias voltage and therewith the MCP gain (see also section 7.3.9). This also highlights the need of a stable thermal environment for a detector in PENeLOPE. Dedicated investigations will have to be performed to estimate the influence of the effect.

7.3.5. Signal readout and data acquisition

Signal decoupling For a reflection- and oscillation-free readout of the signal a resistance-matched coupling of the signal cable to the anode is necessary. A standard RG58 co-axial cable with a characteristic impedance of 50 Ω is used. Matching can be achieved with special anode geometries. [WG94] However, due to the complexity and space consumption this is hardly an option for the large PENeLOPE detector comprising hundreds of detector channels. Another possibility is the matching with a specially designed read-out electronics. [S+01] This has to be developed for the PENeLOPE detector. Indeed, perfect impedance matching is only mandatory if the fast characteristics of the microchannel plate signal (FWHM $\approx$ 0.5 ns) is utilized to analyze timing information. For the prototype tests small reflections are allowed, as their effects can be suppressed by the electronics, which shall only count the detected particles. It is desisted from the effort of a dedicated electronics development at this early stage. The signal is read out with the cable directly connected to the anode of the detector as sketched in figure 7.17. The signal of the Hamamatsu detector, when irradiated with α particles from an ^{241}Am source, is given in figure 7.18. The detector is powered with $U_{\text{lead-out}} = 400\,\text{V}$, $U_{\text{lead-in}} = 2100\,\text{V}$. The large oscillations are suppressed, when the shielding of the high voltage leads is connected with the shielding of the signal line and grounded. The installation of a resistor between signal line and ground gives only a minor improvement.

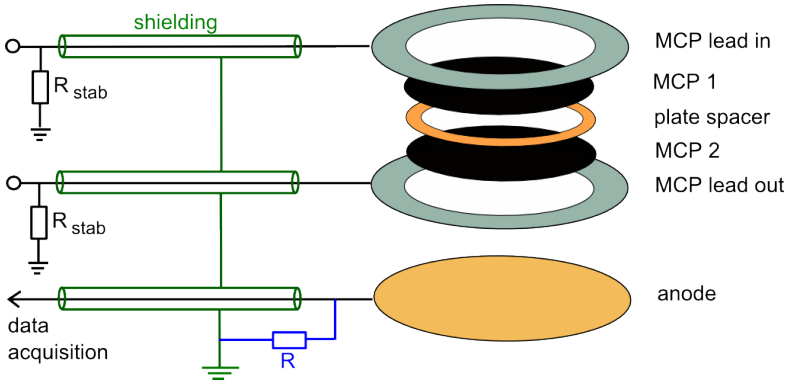

Figure 7.17.: MCP signal read out: The signal cable is directly connected to the anode, the shielding of all the cables are connected and grounded. Optionally, a resistance can be introduced between signal line and ground.

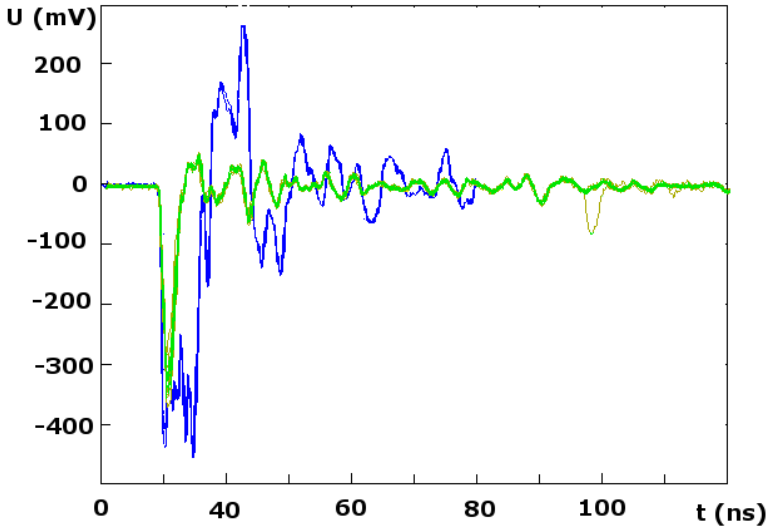

Figure 7.18.: MCP raw signal of α particles generated in the Hamamatsu detector. The signal is given, when the cable is directly connected to the anode without any other arrangements (blue) and with the shieldings connected to ground (green).

Data acquisition Due to the large gain of the MCP chevron detector, the signal does not need to be amplified for further analysis. It can be fed directly into a charge-to-digital-converter (QDC) to measure the pulse height distribution. In figure 7.19 the simple data acquisition system based on CAMAC[30] electronics using the NIM[31] standard is sketched: the signal from the MCP anode is divided by a passive splitter into two parts. One is fed into a discriminator to generate a window for the QDC, which integrates the second part of the signal in this gate. The discriminator has a minimum threshold of 30mV; a fast amplifier can be used for the part of the signal that generates the integrating window for the QDC in order to effectively decrease the threshold.

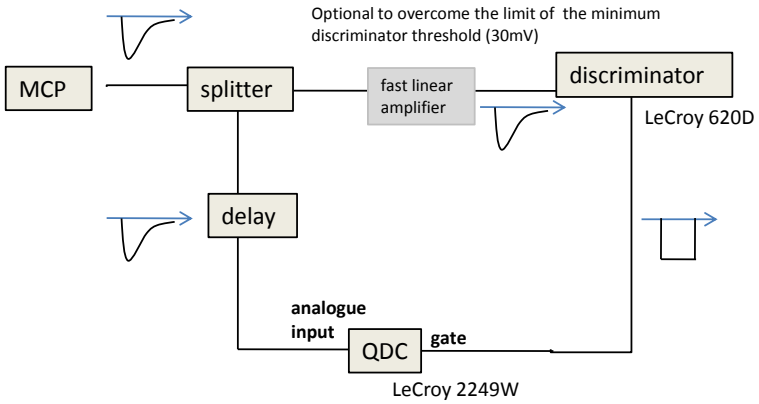

Figure 7.19.: CAMAC based data acquisition system.

7.3.6. α particle detection

An ^{241}Am source was used to test the detector, delivering α-particles with an energy of 5.4 MeV. In figure 7.20 the pulse height distribution measured with the Hamamatsu detector is depicted for different voltages applied to the MCPs.[32] For a better evaluation of the spectrum, an exponential function was fitted to the background combined with a Gaussian distribution for the peak:

$$f(x) = \exp(a + bx) + c \cdot \exp(-0.5((x - d)^2)/e).$$

E.g. the parameters of the fit to the spectrum measured with the highest supply voltage are:

$$a = 10.31 \pm 0.06,\ b = -0.041 \pm 0.0006,$$
$$c = 286.71 \pm 3.3,\ d = 168.4 \pm 0.34 \text{ and}$$
$$e = 20.79 \pm 0.24 \text{ with red.}\chi^2 = 3.59.$$

Plotting the fit results versus the applied voltages (see figure 7.21) shows an increase of the noise and a broadening of the signal peak as well as a shift of the peak position to higher channels with

[30] Computer Automated Measurement And Control - an international standard of modularized electronics.
[31] The nuclear instrumentation manufacturer (NIM)-standard defines a negative logic level (-700mV with 50 Ohm) in digital circuits.
[32] The trigger level has been set to 40mV; the integrating window of the QDC was 40ns wide.

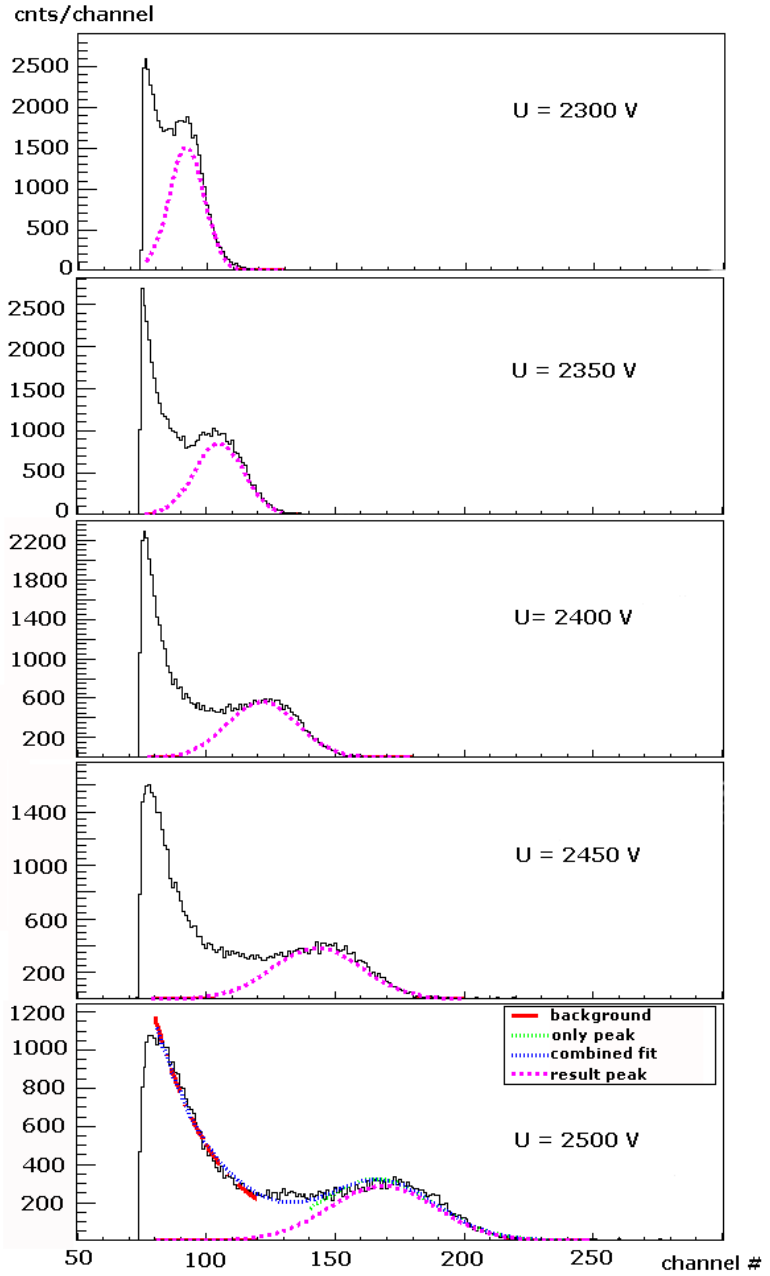

Figure 7.20.: Pulse height spectrum measured with the Hamamatsu detector using a ^{241}Am α source. The voltage at the output of the second MCP was $U_{\text{lead-out}} = 400V$; at the front of the first MCP $U_{\text{lead-out}} = 2300V - 2500V$ were applied. In pink is given the Gaussian part of a combined fit to the complete spectrum consisting of an exponential for the background noise and a Gaussian distribution for the signal. For the spectrum with $U_{\text{lead-out}} = 2500V$, the separate fits for the background (red) and the Gaussian to the signal peak (green) as well as the combined fit (blue) are also given.

increasing voltage. The shift of the peak position with the applied voltage directly correlates to the gain-voltage dependance; it is about 0.382 ± 0.028 per volt. In literature one can find values between 0.3 [Wiz79] and 1 per V [Ham94].
Extracting the signal rate from the integral of the Gaussian part of the fit, which represents the signal peak, gives a count rate of $98 \pm 7\,\mathrm{s}^{-1}$. The expected α rate $\dot{S}$ can roughly be estimated from the sources activity $\dot{N}_{\mathrm{source}} = 3\,\mathrm{kBq}$, the part of the irradiated area - a half sphere due to the geometry of the source - covered by the detector $A_{\mathrm{det}}/A_{\mathrm{half\ space}}$, the open-area ratio of the MCPs (OAR=0.6) and an assumed efficiency of 0.8. The source is positioned at a distance of 2 cm from the detector:

$$\dot{S} = \dot{N}_{\mathrm{source}} \cdot A_{\mathrm{det}}/A_{\mathrm{half\ space}} \cdot 0.6 \cdot 0.8 = 180\,\mathrm{s}^{-1}.$$

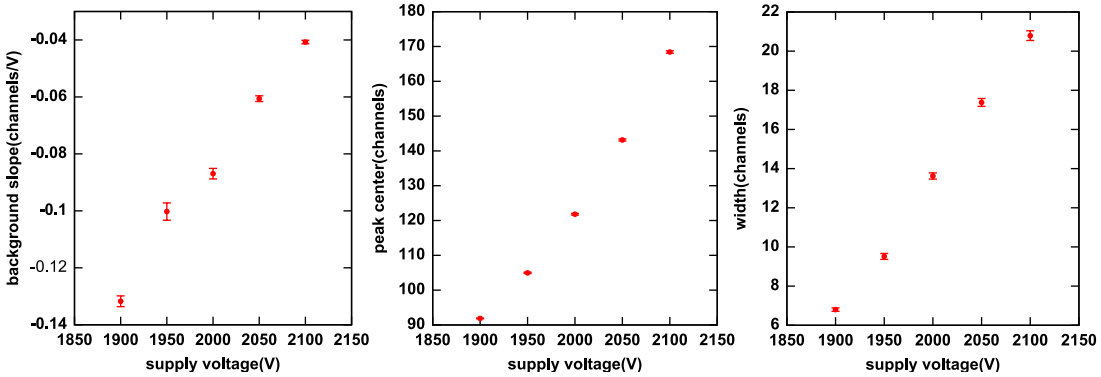

Figure 7.21.: Characteristics of the α signal of the Hamamatsu detector as a function of the voltage applied across the channel plates: background slope (left), peak position (middle) and peak width (right) are determined by the fits in figure 7.20.

The mismatch by a factor of two is probably due to the fact that the efficiency of 0.8 was just assumed. Moreover, there is a discrepancy between the fit function and the real distribution.
Alike, the self-made support with MCPs from Tectra has been tested (see figure 7.22). As in the case of the measurements with the Hamamatsu detector, the signal rate can be extracted from the fit analysis as well as estimated from the activity, the geometrical arrangement and the detector properties. The calculated count rate is about 450 cnts/s, the measured approximately 377 ± 16 cnts/s. The shift of the peak position is 0.675 ± 0.014 channels per volt, thus higher than with the Hamamatsu detector.
From the width of the fitted Gaussian the pulse height resolution PHR can be derived. The PHR is defined as the full width at half maximum (FWHM) divided by the peak position A. In [Ham94] values of PHR=120% are stated as being typical for chevron-type microchannel detectors, without specifying the operation parameters of the detector nor the primary particle. Also [H+85] and [W+77] give a PHR of 150%, moreover showing that this can be improved to 60% by applying an inter-plate voltage of up to 700 V (cf. section 7.3.10). As primary particles UV photons were used. In the presented measurements with the α particles, the PHR ranges between 52% and 94% for the Hamamatsu detector and between 102 and 135% in case of the Tectra plates. However, the peak-to-valley ratio[33] is in both cases very poor (at best 1.4 for the

[33] I.e. the ratio of the counts at the signal peak to the counts in the valley between peak and background. This is a measure for the signal-to-noise ratio.

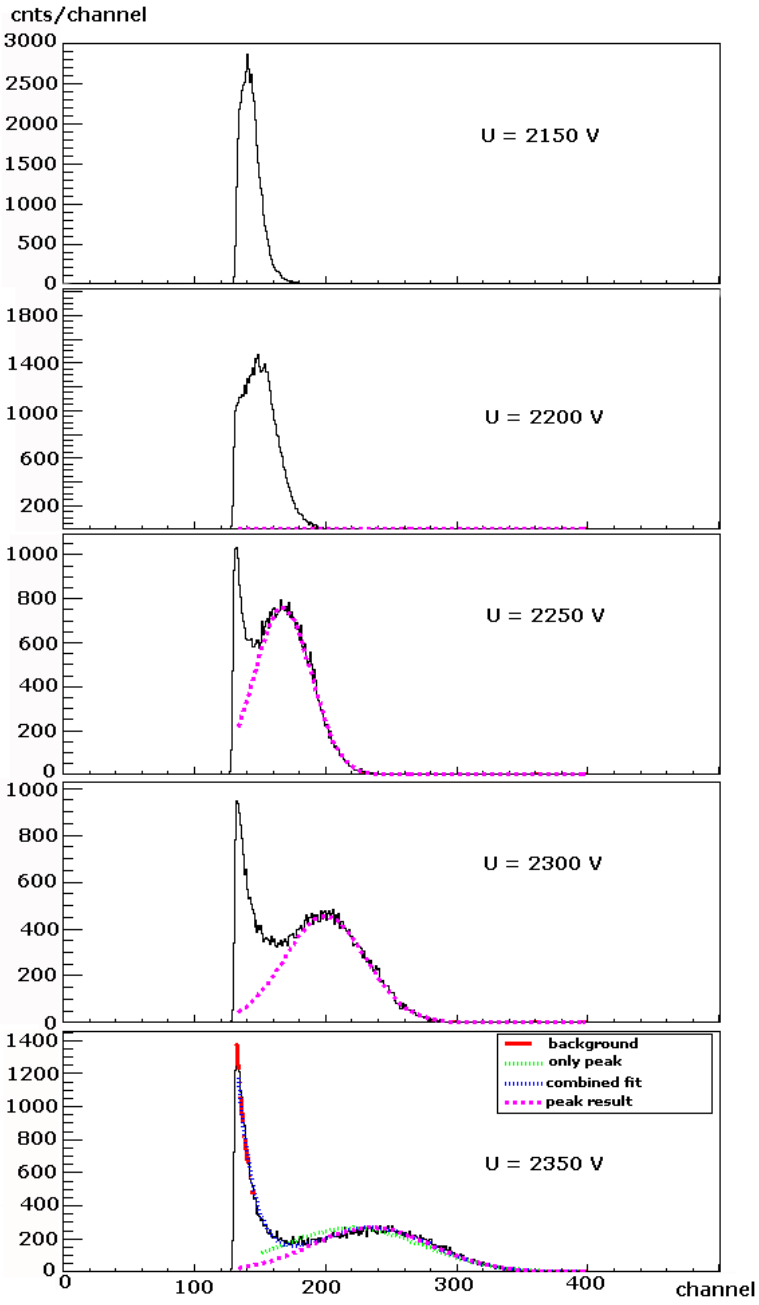

Figure 7.22.: Pulse height spectrum measured with the Tectra plates using an ^{241}Am α-source. The voltage at the output of the second MCP was $U_{\text{lead-out}} = 400V$; at the front of the first MCP $U_{\text{lead-out}} = 2150V - 2350V$ were applied. Besides for the first two spectra, where a fit was not successful, the Gaussian part of a combined fit to the complete spectrum is given in pink. It consists of an exponential decay for the background at low channels and a Gaussian distribution for the signal. For the last spectrum, with $U_{\text{lead-out}} = 2350V$, the separate fits for the background and the signal peak (green) as well as the combined fit (blue) are also given.

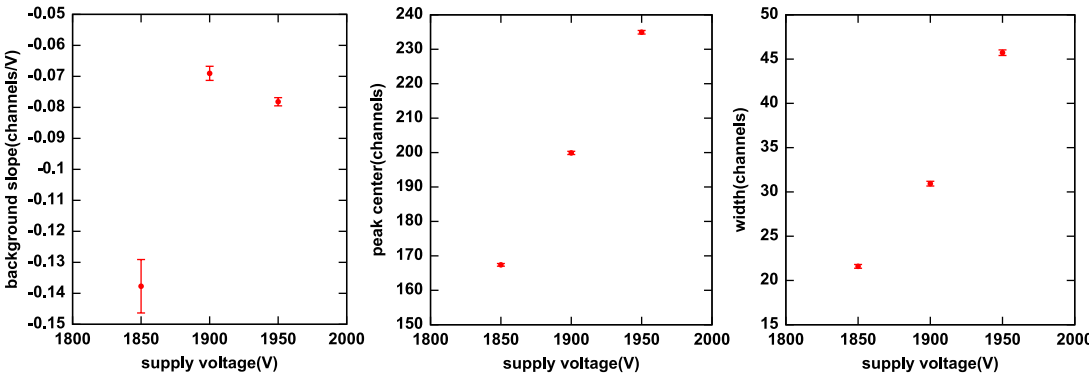

Figure 7.23.: Characteristics of the α signal of the Tectra detector as a function of the voltage applied across the channel plates: background slope (left), peak position (middle) and peak width (right) are determined by the fits as depicted in figure 7.22.

Hamamatsu detector, 1.7 for the Tectra plates) not allowing for a sufficiently good separation of the background and the signal.

7.3.7. Proton detection

The response of the MCP detectors to proton bombardment was tested at the proton source PAFF (proton accelerator for femto-ampere flux). PAFF provides protons in the energy range of 1-45 keV with low intensities. [MH+07] The protons are created in a plasma ion source and extracted from the plasma by an electrical potential of up to 5 kV. The source is situated in a field cage and can be put on high voltage (up to 40 keV). The total energy of the ions extracted from the source part is the sum of the extraction voltage and the field cage potential. After the source section, the ions are guided through a bending magnet to produce a clean proton beam: the magnetic field directs only particles with a specific velocity to mass ratio into the next accelerator section, which is tilted by a defined angle with respect to the up-stream section. The intensity of the proton beam can be influenced by the extraction current adjusted at the plasma source as well as by (de-)focussing the beam onto the detector by means of a simple electrostatic Einzel lense system.
Measurements with the MCP detector (self-made support equipped with the Tectra MCPs) have been performed using protons in the energy range from 10 to 30 keV. A typical pulse height spectrum is given in figure 7.24.
Supply voltages were $U_{\text{lead-in}} = 1950V$ at the entrance of the front MCP and $U_{\text{lead-out}} = 200V$ at exit of the back plate, resulting in a rather low voltage across the plates. No inter-plate voltage was applied. Similar to the measurements with the α particles, the peak was analyzed

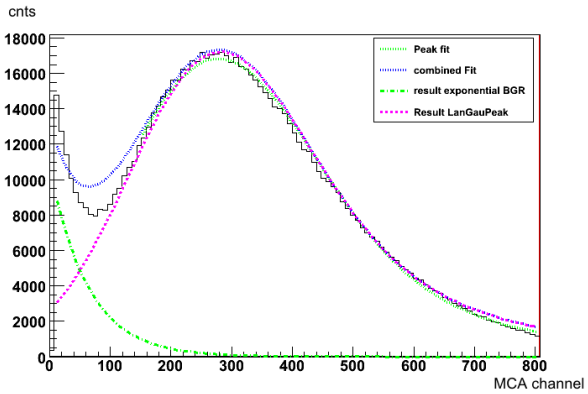

Figure 7.24.: Pulse height spectrum of 20-keV protons from PAFF detected with the MCP detector. An inter-plate voltage of 1750V had been applied.

by fitting an exponential to the background and a convolution of a Landau and a Gaussian to the peak.[34] Starting parameters for the fit of the convoluted function were taken from a gauss fit to the peak region only. Finally, the combination of an exponential background and the Landau-Gauss convolution was fitted to the complete pulse height distribution. The peak position of the spectrum was extracted from the parameter for the center of the Landau-Gauss part.
In figure 7.25, the peak position is plotted versus the proton energy. Two independent series of

[34] In fact, the Poisson statistics combined with a Gaussian should be used. The Landau distribution describes the fluctuations in the energy loss of a charged particle passing through a thin layer of matter. For practical reasons, the Landau-Gauss has been used: the fit routine is provided by ROOT (http://root.cern.ch), the software package used for the analysis. Whereas a Gaussian alone, as used in section 7.3.6, describes the total spectrum better, this distribution seems to give slightly better results for the peak position.

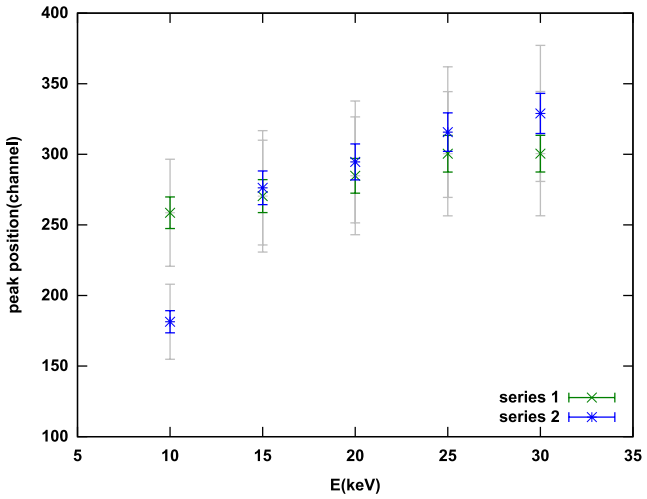

Figure 7.25.: Peak position vs. proton energy. Two individual series of measurements are given in blue and green. The error bars reflect the influence of accelerator parameters, the colored ones without, the grey ones with the effect of beam misalignment. See the text for more details.

measurement were performed. For proton energies of 10 and 30 keV, the operating parameters of the accelerator - i.e. magnetic field of the bending magnet, extraction current, ratio of extraction and field cage voltages - have been varied to estimate the influence of a non-stable proton beam. The possible systematic effects are accounted for by the error bars. Uncontrolled fluctuations of the accelerator settings over the range, in which they have been varied for these studies on systematic effects, are unlikely. However, the control and monitor mechanisms of the accelerator are only poor so that a fluctuation of a parameter setting of the order of 20% can not be excluded. Table 7.4 summarizes the variations of the parameters and their impact on the peak position. The largest contribution is due to a variation of the magnetic field in the separating magnet, thus the position of the proton beam at the detector. The resolution of neither the magnet supply current monitor nor of a hall sensor placed in the magnetic field sufficed to resolve the small changes of the magnetic field needed to clearly influence the number of particles hitting the detector. The count rate of a beam monitor installed at PAFF has thus been taken as a measure for the beam position. Thus, in figure 7.25, different error bars are given, once incorporating the beam alignment effect, once not. Within these large uncertainties, the two series of measurements agree except at 10 keV. However, these studies on systematic effects cannot disentangle the accelerator specific uncertainties from an instable detector operation itself. Measuring six times without changing any parameters, resulted in a fluctuation of the peak position by 2.6%. This is of the order of the error introduced by varying the source current or the ratio of the extraction and field cage voltages.
Varying the voltage applied across the channel plates results in a shift of the peak position by 1.8 channels per volt, approximately 0.6%. A drift of the voltage during the measurements of more than a few volts can be excluded.
The measurements show a trend of the peak position to higher channel numbers with increasing proton energy. The increase is about 14% between 10 and 30 keV. Figure 7.9 suggests a gain increase by approximately 25% in this energy range.

parameter	**value**	**effect on peak pos.**
source current (μA)	60,100,150,200	3%
U_{extr}(kV)/U_{total}(kV)	0.1:10, 0.2:10, 0.3:10, 0.5:10	1.7%
magn. field of sep. magnet (cnt. rate of beam monitor (s^{-1}))	50-80, 200-500, 600-800, 800-1000	14%
long term measurement	-	2.6%
fit error	-	0.3%

Table 7.4.: Variation of parameters in the measurements at PAFF and their effect on the peak position. In addition, the fluctuation over six repeated measurements with fixed parameters and the order of magnitude for the error of the fit itself are given.

As can be seen from the pulse height spectrum shown in figure 7.24, the signal peak is rather broad and not well separated from the background like in the measurements with the α particles. The peak-to-valley ratio is 2 to 2.5 compared to ≈ 1.7 measured with the α particles; The pulse height resolution PHR is in average of the order of 180%, with the tendency to decrease slightly for higher proton energies. This is larger than in the measurements with the α particles (130%), which may be attributed to the energy spread of the proton beam. However, one has to be cautious comparing the two measurements as slightly different setups for the data acquisition were used differing e.g. in the cable lengths and the width of the integrating window of the QDC. Still, the poor signal-to-noise ratio in the measurements performed at PAFF questions the use of a chevron detector in this configuration for the PENeLOPE experiment as the protons cannot be distinguished from the background with the necessary precision. See also the following section.

7.3.8. Noise

Figure 7.26 shows a measurement with the Tectra plates without any source. The voltage across the plates was set to 1900 V.[35] The rate fluctuates up to 10 cnts/s, being in average 3.25 ± 1.69. Of course, the measured rate depends heavily on the choice of the trigger threshold - here set

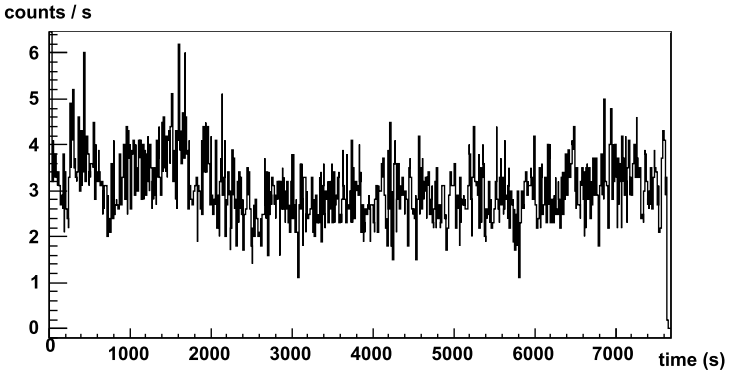

Figure 7.26.: Background rate measured with the Tectra plates over $\approx$ 2h.

[35] 2300 V at the input and 400 V at the output lead.

to 30mV - should, however, not be significantly larger than the dark count rate specified for the plates. According to the specifications, the dark current of the plates is about $I_{\mathrm{dark}} = 0.3\,\mathrm{A/cm^2}$. With the effective surface of the plates $A_{\mathrm{MCP}} = 6.9\,\mathrm{cm^2}$ and an assumed gain of 10^7, the total dark count rate is estimated:

$$\dot{N}_{\mathrm{dark}} = I_{\mathrm{dark}} \cdot \frac{A_{\mathrm{MCP}}}{10^7 \cdot e} = 2.3\,\mathrm{cnts/s}.$$

This roughly fits the observed noise rate, however, a rather low gain of $1 \cdot 10^7$ has been assumed. A higher gain transfers to a lower dark count rate derived from the specified dark current.
To exclude the noise generated by the electronics itself, a random trigger was added in the measurements. It results in the peak at low channel numbers in figure 7.27; thus, the noise from the electronics does not contribute significantly to the dark counts. The increased dark

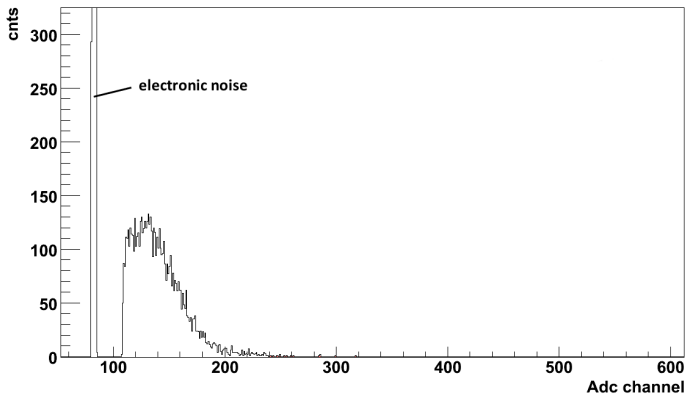

Figure 7.27.: Pulse height distribution recorded without any source. The peak at low channels is the noise contribution from the electronics measured by a random trigger.

count rate is most likely due to dust particles on the surface of the MCPs, which may provoke micro-discharges. With brand-new Photonis plates a dark count rate of $\approx 1.1 \pm 0.7\,\mathrm{cnts/s}$ was measured; from the specifications 1.5 cnts/s are expected. In both cases, the big error reflects the rather large fluctuation of the count rate (see also next section).
A low background rate is very important to separate the proton signal from the noise. Scaled up to the size of the proton detector in PENeLOPE ($\approx 2300\,\mathrm{cm^2}$), the total noise rate would be 476 and 1406 cnts/s, for the measured rates of 1.1 and 3.25 cnts/s, respectively. To estimate, how the background rate influences the signal-to-noise ratio, the possibly measured sum spectrum in PENeLOPE has been simulated, following the characteristics of the spectra presented: Starting with $6 \cdot 10^7$ stored neutrons, assuming a collection efficiency of 0.6 and a detection efficiency of 0.4, the number of protons generating a signal in the complete detector sums up in a storage phase of 5000 s to $\approx 6.76 \cdot 10^6$. A histogram resembling the proton peak has been randomly filled with these counts. Additionally, to simulate the background, a histogram following an exponential decay has been randomly filled with the number of counts generated in the storage phase assuming a background rate constant in time. The noise level is varied between 100 and 2500 counts per second. The combined histogram has been fitted and the peak-to-valley ratio extracted. Results are given in figure 7.28: The signal-to-noise ratio improves faster than linear with lower noise rate. Usually, the threshold to distinguish between noise and proton counts is

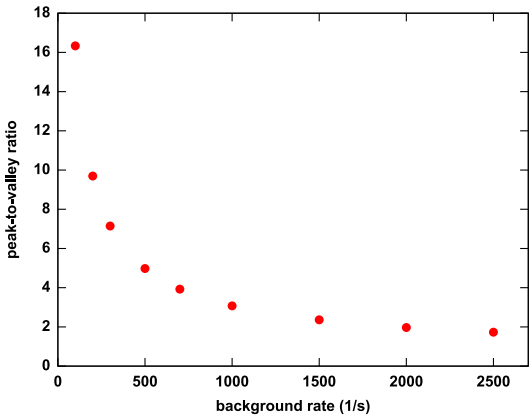

Figure 7.28.: Influence of time-constant background rate on the peak-to-valley ratio of a simulated proton spectrum in PENeLOPE. For details see text.

set at the valley between the exponential background and the gauss-like signal. Still, a certain amount of events is misinterpreted due to the overlapping distributions (c.f. figure 7.29, left side): background is counted as protons and at the same time valid proton hits are disregarded as noise. The amount of misidentified events as a function of the peak-to-valley ratio is plotted on the ride side of figure 7.29. At the noise rate of 500 counts per second, corresponding to a peak-to-valley ratio of five, still seven percent of the valid proton events are misidentified. The number quickly increases, when going to worse signal-to-noise ratios, thus larger background. In view of the envisaged precision in the lifetime measurement of 10^{-4}, this large amount of

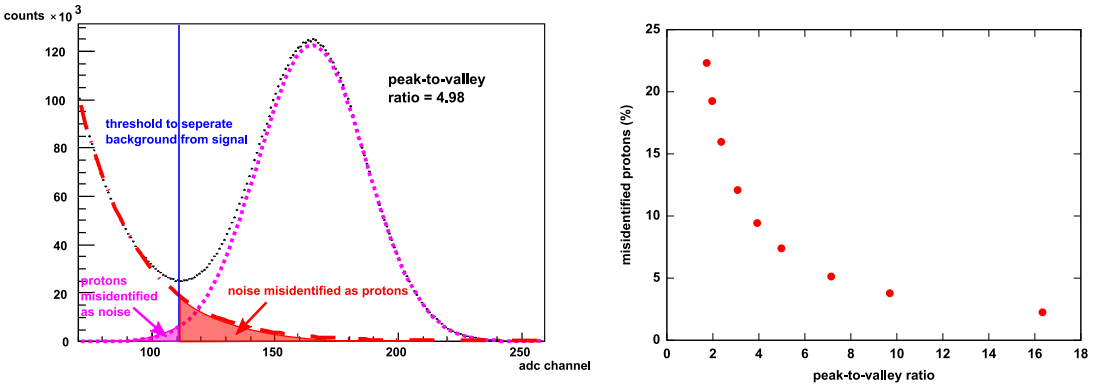

Figure 7.29.: Left: Exemplary simulated proton spectrum for a background rate of 500 cnts/s. Right: Percentage of misidentified protons as a function of the peak-to-valley ratio. For details see text.

misinterpreted events is most likely much too high.
However, time-constant background can be handled much better than any time varying effects.

7.3.9. Time stability

On the time scale of the neutron lifetime, no changes of the signal and noise characteristics are allowed for. These would distort the proton count rate evolution during a storage phase and a false neutron lifetime would be extracted. In figure 7.30, an example of such a drift is given, measured with the Tectra MCPs and the α source. The count rate as well as the peak position, extracted from a fit to the spectra, is plotted versus the time. Both numbers increase by 10% within the first 1500 s. The effect, meaning a drift of the gain of the plates, is of the same order and time characteristics as the change of the resistance reported in section 7.3.4, and can bemost likely contributed to it. Looking more closely to the noise rate in figure 7.26, section 7.3.8, also

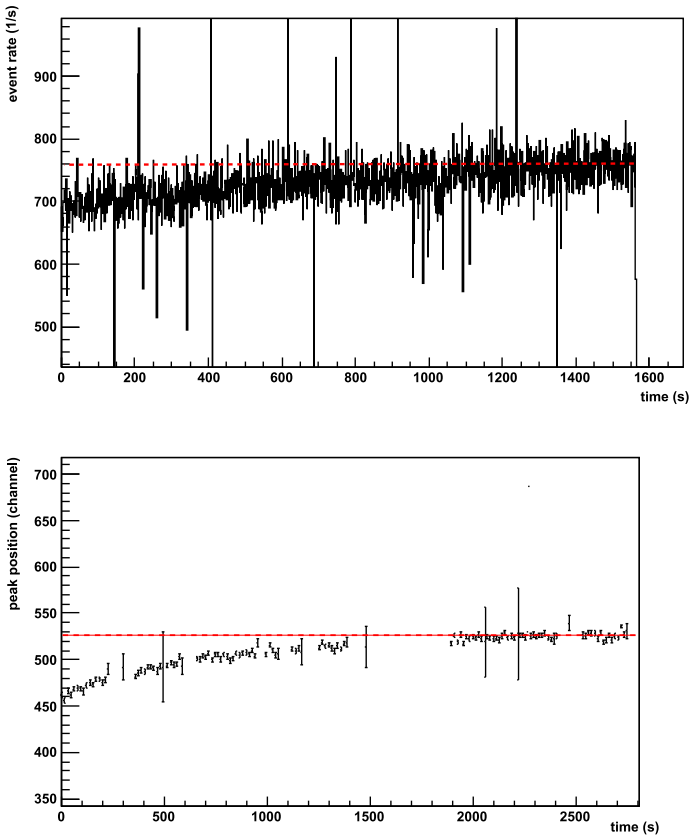

Figure 7.30.: Top: Count rate evolution measured with Tectra MCPs and the α source. Bottom: position of the signal peak versus measuring time. The red dashed lines have been added to guide the eye.

here significant drifts over critical time spans can be found (see figure 7.31): Between 650 s and 1700 s, the count rate increases from 2.6 to 4.2, thus within 1050 s by a factor 1.6; Afterwards, it decreases within 750 s by 0.65. This time, the effect is not caused by the resistance drift just discussed, as it has been waited for the warm-up phase after initially powering the plates. Still, thermal drifts cannot be excluded as the temperature has not been monitored during the measurements. Other reasons can be thought of: e.g. stability of vacuum pressure, voltage

supply or trigger threshold have only been monitored with limited accuracy. More dedicated

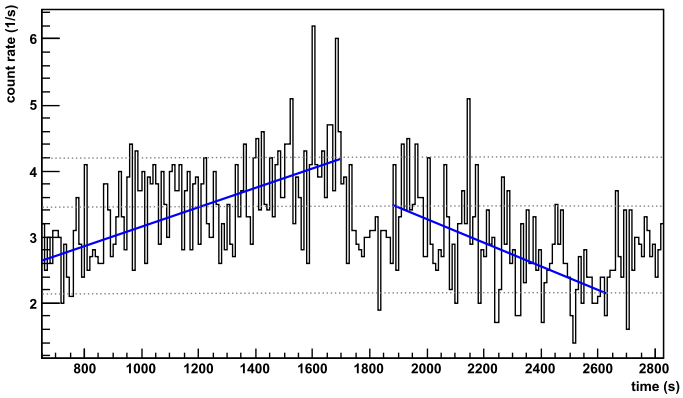

Figure 7.31.: Close-up of the noise rate from figure 7.26. The blue lines mark the trend of the mean count rate in two selected time spans.

measurements with an enhanced monitor system are needed to clarify the rate fluctuations.

7.3.10. Possibilities for signal improvement

For proton detection in PENeLOPE, the separation of the signal from the background needs to be improved, especially the signal-to-noise ratio. One possibility is to aim for a narrower signal peak:
The channel plate acts like a charged capacitor with the capacitance C. When a primary particle triggers an electron avalanche, charge is transferred from one capacitor side to the other. The voltage supply is most likely not able to recharge the capacitor fast enough. Thus, the charge transfer leads to a voltage drop across the capacitor according to $\Delta U = \Delta Q/C$, which results in a reduced gain. With a typical plate capacitance of the order of $\leq 1\,\mathrm{pF}$ and a charge of a about 15 pC, the voltage drop amounts to $\approx 60\mathrm{V}$. The voltage can be stabilized by introducing a capacitor parallel to the plates. Already with 100 pF the voltage drop decreases to $\Delta U \approx 0.15V$. Hamamatsu suggests to introduce a capacitor between the lead-out i.e. the backside of the second MCP and the read out anode, thus stabilizing $U_{\text{lead-out}}$. The resulting spectrum is depicted in figure 7.32; no significant improvement is visible.
Another possibility for a wide signal peak distribution is connected with the inter-plate characteristics of the chevron stack: The charge cloud exiting the back of the first MCP will spread before entering the second plate and thus may trigger several channels in the second plate. The spread and therewith the number of newly triggered channels depends on the drift distance, i.e. the inter-plate distance, and the electrical field. Collimating the charge cloud to a few channels, by a small inter-plate distance[36] or introducing a voltage difference between the MCPs, should lead to a narrower peak. However, the overall gain is expected to decrease, as the amplification in the channels runs into saturation.
The effect of this inter-plate voltage has been studied using the MCPs from Photonis in the support shown in figure 7.14 and the α source. In order to contact the back of the first and the

[36] In the Hamamatsu detector this is already realized. The spacer between the plates is only 0.1 mm thick.

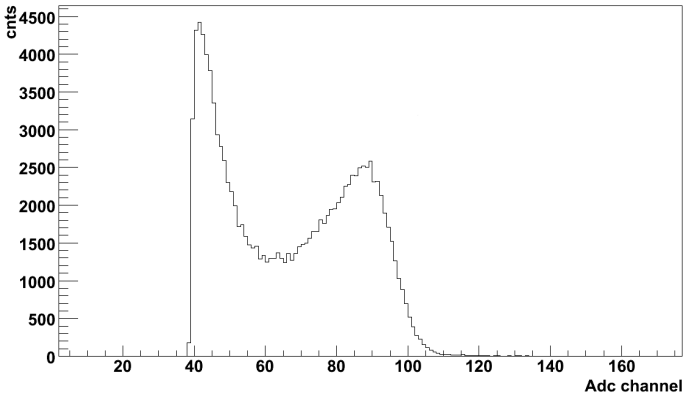

Figure 7.32.: Pulse height spectrum measured with the Hamamatsu detector from a ^{241}Am source. Between the output of the second MCP and the anode a capacitance of 1 nF has been added.

front of the second MCP individually, two more metal anodes as well as an insulating spacer had to be introduced replacing the copper spacer, therewith increasing the inter-plate distance from 0.6 mm to 3.5 mm (cf. section 7.3.3).
Keeping the voltage at the exit of the second plate fixed at 200 V and that across each plate at 950 V, the inter-plate voltage was increased from 0 to 100 V in steps of 10V. A capacitance of 1 nF was added parallel to each of the plates. In figure 7.33, the peak to valley ratio (as defined in section 7.3.6) as well as the PHR are depicted versus the inter-plate voltage. Both first improve with the inter-plate voltage and than remain constant. Probably, in the beginning the larger inter-plate distance is compensated. However, the separation of the signal from the background is still poor. Exemplary, in figure 7.34 the pulse height distribution is given for an inter-plate voltage of 80 V.

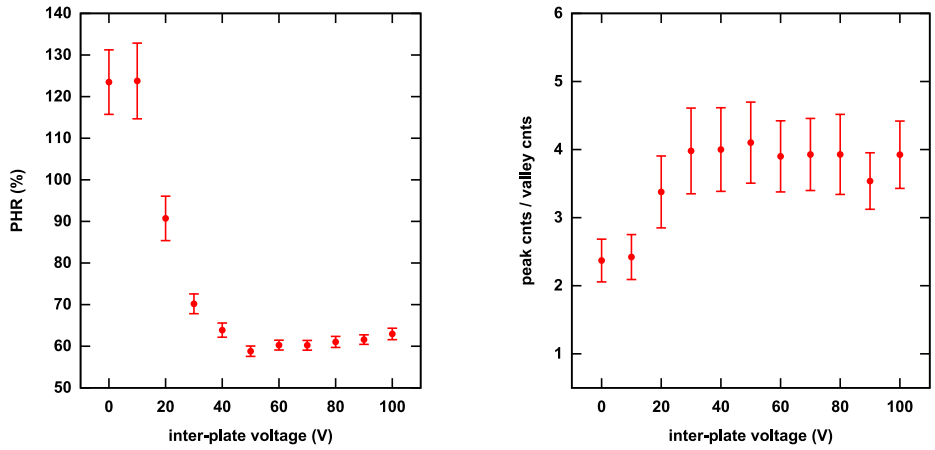

Figure 7.33.: MCP signal resolution with a voltage applied between the two MCPs. Left the PHR and on the right the peak-to-valley ratio is plotted versus the inter-plate voltage.

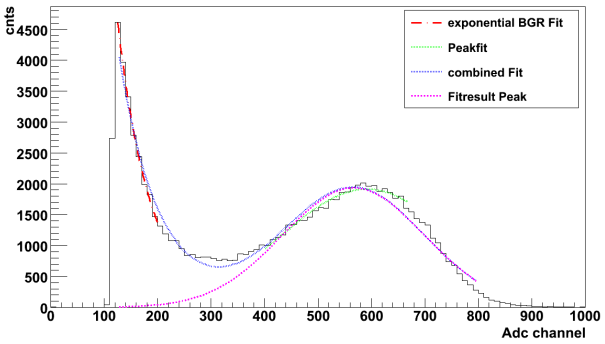

Figure 7.34.: Pulse height distribution of the Photonis MCP irradiated with ^{241}Am particles and at an inter-plate voltage of 80V.

7.3.11. Large scale PENeLOPE detector

To cover the detection area in PENeLOPE ($\approx 2300\,\mathrm{cm}^2$) with microchannel plates results in a trade off for the size and geometry of the plates between good areal coverage, number of channels and price. Using standard circular microchannel plates gives the most unfavorable fraction of insensitive area: plates with a diameter of $\approx 40\,\mathrm{mm}$ cover effectively only 30%. Rectangular or even custom-made trapezoidal shapes are advantageous and up to $\lesssim 60\%$ sensitive area could be achieved. For reasons of handiness the whole detector should be divided in three or four segments restricting the flexibility in arranging the plates. Exemplary configurations are depicted in figure 7.35 and quantified in table 7.5.

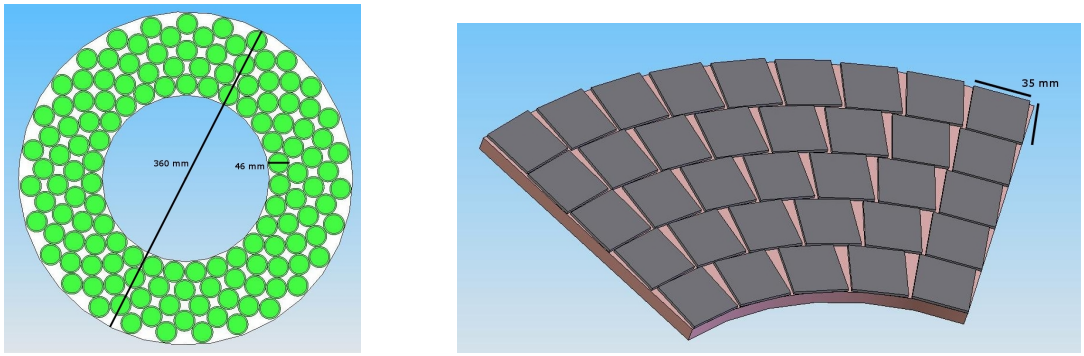

Figure 7.35.: Coverage of PENeLOPE detector plane with MCPs. Left: using round plates with a diameter of 46 mm ignoring requirements on subdivision. In the right part, a 60° piece is covered with quadratic plates with a side length of 35 mm.

shape	**size (mm)**	**number**	**effective coverage**[37]	**price (k€)**[38]
round	46ø	135	0.33	153
round	65ø	60	0.27	-
quadratic	35	222	0.53	205
quadratic	44	138	0.52	200
trapezoidal	44 x 56 x 43	130	0.55	218

Table 7.5.: Overview of various MCP configurations for the PENeLOPE detector plane.

As the gain of the channel plates strongly depends on the applied voltage, a separate supply voltage must be provided for each chevron pair. Alternatively, plates with similar characteristics, especially gain and resistance, can be combined in sections, which are powered with the same voltage. The same holds for the use of APDs. Instead, the gas multiplication detector can be supplied in total with only a few voltages.

[37] The effective coverage includes the factor for the open are ratio.
[38] Price estimates are based on quotations recieved end of 2009.

7.3.12. Résumé: a PENeLOPE MCP detector?

Many examples in literature prove that proton detection with MCPs is in principle possible. Their use in PENeLOPE, however, is in view of the presented studies questionable: Poor area coverage, a relatively high dark count rate and a bad signal-noise separation are heavy downsides for using MCPs in PENeLOPE. Most likely, a thorough revision of the circuit for the supply voltages and the readout can improve the signal. The installation of capacitors parallel to the plates,e.g., should be investigated further. So far, the use of an inter-plate voltage turned out to be beneficial. Also a capacitively coupled readout of the signal should be tested. It is a standard concept in detector physics and the initial idea to set the channel-plate stack in total to a high electrical potential and introduce a large distance between the back of the second plate and the anode, which can then stay at ground potential, turned out to be disfavorable. The anode, collecting the charge, should be placed closer to the second channel plate ($d \leq 1$ mm); Another anode for signal read-out could be added next to it, electrically isolated by a thin Kapton foil. The signal is transfered by capacitive coupling. This way, the charge-collecting anode would be at higher potential whereas the read-out anode could still be at ground potential without the need of large distances.
Still, including all these improvements, the detector will most probably not suffice the demands. For the precision measurement of the neutron lifetime at the level of 10^{-4}, a very good signal-to-noise ratio is necessary; The presented spectra have only a peak-to-valley ratio of 2.5 at most. Energy resolution and the possibility of particle discrimination will be limited. Performance studies, in particular on the response to electrons, still have to be done.
Also operation at cryogenic temperatures and at large magnetic fields needs to be investigated. From literature no difficulties are expected, if the detector is coupled to the radiation shield at 78 K; especially not, when low-resistance plates are used. A stable temperature of the plates has to be assured to avoid gain drifts. Besides the principal detection features, price and handiness have to be considered, too. To cover the detector area with chevron detectors, only reaching a effective area coverage of less than 0.6, the channel plates alone would cost about 200 000 €. This is still approximately a factor of three smaller than the costs when using APDs.
The channel plate detectors must be stored and handled under clean room conditions. Regarding the size of the complete setup and the placement in an experimental hall at a reactor or accelerator, this is only possible with certain limitations when e.g. using a mobile clean-room tent. In the design of the support special care has to be taken to avoid mechanical stresses introduced when going to low temperatures. Of course, the same holds also for other detector concepts, but the MCPs are especially fragile.
Considering all this a proton detector in PENeLOPE based on MCPs is disfavoured.

8. Summary and Outlook

PENeLOPE is a new neutron storage experiment, which aims to determine the neutron lifetime τ_n with a relative precision of 10^{-4}, an order of magnitude more precise than the current value of 880.1 $\pm$1.1s published by the DPG. [B$^+$12] Therewith, it will help to shed light onto the puzzling situation of the neutron lifetime measurements: the two most precise experimental projects undertaken so far, from Serebrov et al. [S$^+$05] and Arzumanov et al. [A$^+$00], come to contradicting conclusions about the lifetime and differ by $7\,\sigma$.
Whereas both these experiments were based on the storage of ultra-cold neutrons in material bottles, PENeLOPE will use a different experimental technique and keep the neutrons in a magneto-gravitational trap, created by a multi-coil stack of superconducting magnets.
Besides the standard method of counting the surviving neutrons, the lifetime will be extracted from time-resolved counting of the products from neutron decay, mainly the protons. Thus, the two key parts of the experiment are the magnet and the decay particle detector; on both, studies have been performed in this thesis.

The complexity of the magnet system demands for prototyping to confirm the coil design before final construction can start. Several requirements make the magnet a non-standard and custom-made development: The multi-pole configuration needed for magnetic neutron trapping leads to forces as large as 1.15 MN which have to be taken by the support structure. After filling the neutrons into the trap container, the time span of the material storage phase until the magnetic confinement takes over has to be kept at a minimum to avoid losses from wall collisions. Hence, the magnet has to be ramped up as fast as possible from zero to nominal current. This has to be accounted for in the thermal design of the coil and its support. Thus, stable operation at nominal current and ramping speed of the magnet have to be proven. Moreover, complex superconducting magnets always have to be trained, before they can be operated.
In this thesis

- A complete test facility with a liquid helium bath cryostat has been built up. The cryostat was upgraded in a second phase to be able to train all coils of PENeLOPE, individually or in packages, in the future.
- A first prototype from the company Scientific Magnetics was trained. It failed its specifications and reached only 70% of the nominal current. Thermal stresses, introduced when cooling down the magnet, lead to cracks in the epoxy resin of the coil package and therewith mechanical instabilities on powering the magnet. The outcome of the faulty design of the support structure initiated a change of the industry partner to Babcock Noell, a major step forward in the development of the whole experiment.
- The new design approach by Babcock Noell was confirmed to be working successfully with a second prototype coil: with 350 A it exceeded its design value by 20%; It could be ramped with 8.5 A/s, a factor of three more than required. Cycle and longterm tests succeeded as well.
- The performance of peripheral components was studied: A quench heater successfully initiated quenches when releasing an energy of 69 J in a short burst. However, using the

quench heater as a constant heat source to test the safety margin in the thermal design of the magnet, needs much more power than expected and demands for a sophisticated model of the heat transportation in the magnet. The cryogenic protection diodes showed an unexpected high forward voltage. This initiated further studies on the characteristics of the diodes in large magnetic fields after this thesis.

Currently, a stack of three outer coils is under construction and will be tested in 2013. By this, it will be checked, whether the design can cope with the large repelling forces in a multi-coil configuration. Additionally, as the magnet test facility incorporates all the equipment also needed in PENeLOPE, it is used to develop the experiments slow control system meanwhile.

In the final experiment, it will be mandatory to check if the actual field configuration fits the field design, examining especially the trap potential near the walls of the storage container or critical low-field regions. Hence, a magnetic field mapper was installed at the first test facility. The setup consists of a linear translation stage for all three dimensions and a wobble stick that transfers the movement over a single vacuum feed-through, featuring the advantage that the actuators are placed outside the cryostat. Algorithms to analyze the measured data were developed:

- The magnetic field is reconstructed from the projections measured by three hall sensors in a skew coordinate system.
- Systematic effects, like displacement and tilt of the sensors, were simulated with the help of a field map calculated by a FEMM program. To this end, interpolation methods for regular and irregular field grids were adopted.
- To test the performance of the system, the field map of the first prototype coil pair has been scanned. The magnets position was determined with a precision of 0.3 mm by localizing the field minimum in its center. In the process, different minimum finding algorithms were benchmarked.

Difficulties to adapt the system to the geometry of PENeLOPE, suggest a change of the actuator concept of the mapping device in the PENeLOPE setup. The presented measurements uncovered mechanical downsides enhanced by the level arm and thus help to improve the setup.

The second part of the thesis deals with the decay particle detector of PENeLOPE. It will be positioned on top of the storage volume and needs to operate in the harsh environment of a liquid-helium cryostat, i.e. at cryogenic temperatures around 70 K, vacuum pressure of 10^{-8} mbar and large magnetic field of 0.6 T. To extract the neutron lifetime with the envisaged precision from the proton count rate evolution, stringent requirements are set on the time stability and quality of the detector signal.
As a possible candidate, microchannel plates in chevron configuration have been studied. From literature it is known, that they can be used in the environment of PENeLOPE, that they can detect single protons with energies down to a few keV with efficiencies up to 0.85 and at the same time have low efficiencies for electrons, X-rays or γ-radiation. A detector has been build with bare channel plates, developing an own plate support, and its characteristics compared to a complete detector from Hamamatsu. Tests with α particles and protons in the energy range from 10-30 keV were performed. Mainly, the following two features have been identified in the measurements:

- The spectra have a peak-to-valley ratio of 1.7 - 2.5. This implies that $\approx 20\%$ of the proton events are misinterpreted.

- Drifts of more than 10% over time spans in the order of the neutron lifetime have been observed. While a change of the resistance of the MCPs due to ohmic heating could be identified as one reason, more dedicated studies are necessary to clarify the nature of such drifts. Time-stability of the detector signal is one the most important criteria for the PENeLOPE detector.

To this adds the poor effective area coverage typical of microchannel plates, which is at most only 60%. Thus, the use of MCPs in PENeLOPE is questionable, and in the future, it will be focused on the development of a detector based on APDs. Protons have already been measured at cryogenic temperatures with an excellent signal to noise ratio (see figure 8.1). Currently, a

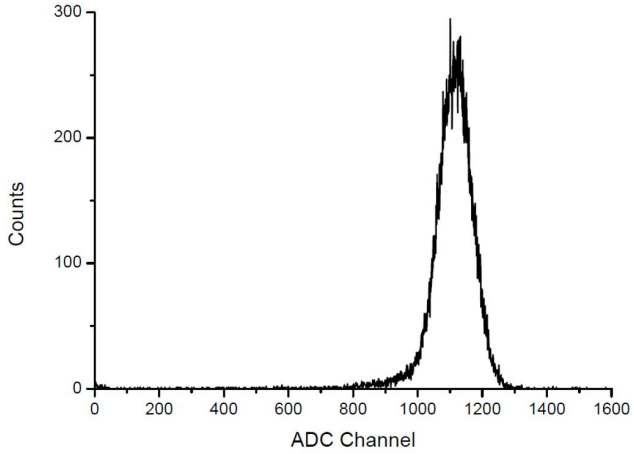

Figure 8.1.: Pulse height distribution of 30-keV protons from PAFF measured with a $10x10\,\mathrm{mm}^2$ avalanching photodiode cooled to 77 K. [Tie12]

prototype with nine APDs including read-out electronics is under development. Funding for two 45° segments with 264 APDs is applied for.

A. Prototype magnet from Scientific Magnetics

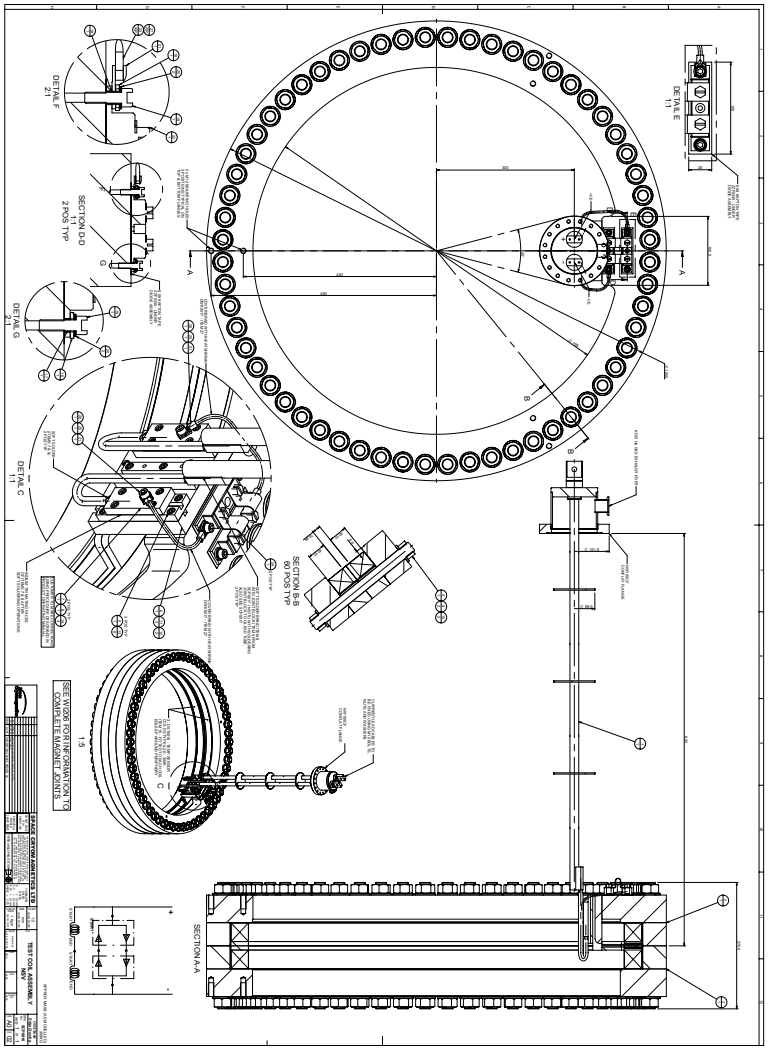

Figure A.1.: Technical drawing of the prototype coil. [Sci08]

Inductance The inductance of the magnet consists of the self-inductances L^s of the single coils and their mutual inductances M and can be calculated from the dimensions of the coils A.1. As the coils are identical, their self- as well as the mutual inductances are the same, respectively, and the total inductance is given by [Gro04]:

$$L = 2L^s - 2M$$

The self-inductance L^s of a circular coil with rectangular cross section can be calculated from the radius r, its thickness b and the number of windings N:

$$L^s = 0.019739 \left(\tfrac{2a}{b}\right) N^2 K' = 7.26\,\mathrm{H}$$

Here, K' is a tabulated geometric parameter depending on the radius, the thickness and the radial width [Gro04].
The mutual inductance is

$$M = N^2 M_0 = N^2 f r = 4.54\,\mathrm{H}$$

Again, f is a tabulated value for circular coils with rectangular cross section taken from [Gro04]. Thus, the total inductance of the magnet is about $L = 5.44\,\mathrm{H}$.

windings N of single coil	1958
inner radius of single coil	407 mm
radial width of single coil	38 mm
height of single coil	40.4 mm
axial distance of coils	15.9 mm

Table A.1.: Dimensions of the coils.

B. Helium exhaust

To secure the CoTEx cryostat against critical overpressure and possible damage in case of a quench or sudden loss of insulation vacuum, exhaust lines for the Helium gas are installed (cf. section 4.2 and 4.2.1). They are realized via bellows which have a diameter of 66 mm and withstand 2.5 bar absolute pressure thus 1.5 bar against atmosphere. As a last resort safety valves, opening at 1 bar overpressure, release the helium into the experimental hall. They are placed at the end of one of the exhaust lines.
To estimate the maximum outflow capacity, the limit of choked flow is considered, where the mass flow through the exhaust reaches a maximum. This mass flow must exceed what is expected in case of a quench or the sudden loss of insulation vacuum. The following calculations are based on [BE08]. A pressure tank at $p_t = 2$ bar is considered which has an outlet with a diameter of 66 mm and a length of 354mm (cf. figure B.1). The exit of the outlet is at atmospheric pressure.

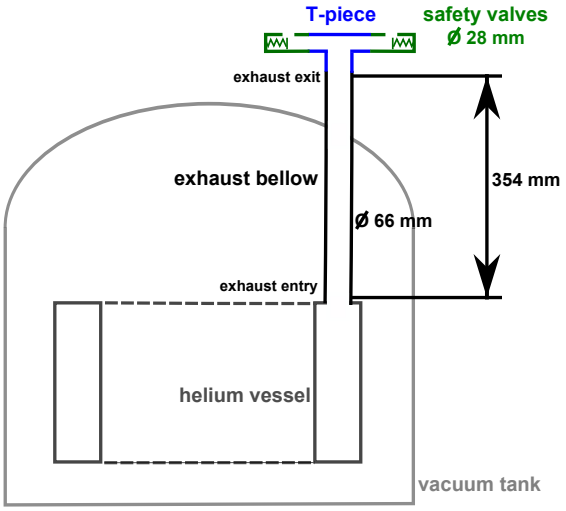

Figure B.1.: Sketch of the helium exhaust line of CoTEx opening to the experimental hall.

Helium gas temperature is assumed to be 10 K.[39]
The maximum outflow velocity is reached at the critical pressure ratio:

$$\left(\frac{p_o}{p_t}\right)_{crit} = \left(\frac{2}{\kappa+1}\right)^{\frac{\kappa}{\kappa-1}} = 0.487,$$

where κ is the adiabatic exponent. Up to that critical point, the pressure in the outflow p_o can be set to the ambient pressure p_{at}, beyond that, there is due to turbulences a backing-up in the outflow. The adiabatic exponent κ is given for an ideal gas as

[39] This temperature is measured in the exhaust of the current leads when it is opened and cooled by the gas which evaporated from the liquid helium.

$$\kappa = \frac{f+2}{f},$$

with f being the number of degrees of freedom. In case of monoatomic helium it is $f = 3$, which does not change at low temperatures as there are no degrees of freedom which can freeze out. For

$$\frac{\mathrm{p_o}}{\mathrm{p_t}} = \frac{\mathrm{p_{at}}}{\mathrm{p_t}} > (\frac{\mathrm{p_o}}{\mathrm{p_t}})_{\mathrm{crit}}$$

the flow is subcritical. For

$$\frac{\mathrm{p_{at}}}{\mathrm{p_t}} < \frac{\mathrm{p_o}}{\mathrm{p_t}} = (\frac{\mathrm{p_o}}{\mathrm{p_t}})_{\mathrm{crit}}$$

it is supercritical.
With $\mathrm{p_t} = 2\,\mathrm{bar}$, the pressure ratio is 0.5 and therefore the helium flow is sub-critical. However, already at a pressure of 2.1bar it gets supercritical. The mass flow is given by (cf. also [Ve92]):

$$\dot{m} \quad = \quad \mu \cdot A_{\mathrm{o}} \cdot \psi_{\mathrm{max}} \sqrt{2 p_t \rho_t}.$$

The outflow function ψ is maximal in the critical case and given by:

$$\psi_{\mathrm{max}} = (\tfrac{2}{\kappa+1})^{\frac{1}{\kappa-1}} \sqrt{\tfrac{\kappa}{\kappa+1}}.$$

This mass flow is reduced by the flow resistance μ determined by outlet geometry.

Outflow resistance For more complex outflow geometries μ is calculated from the sum over all the parts of the exhaust. Contributions of longer tube sections are accounted for via their drag numbers λ_i, their lengths l_i and the diameters d_i, whereas single objects such as angles or reductions are included via their resistance coefficients ζ_i:

$$\mu = \sqrt{\frac{1}{1+\sum_i \lambda_i \frac{l_i}{d_i} + \sum_i \zeta_i}}$$

.
The flow resistance ζ depends strongly on the exact geometry of the specific piece, and there are only empirically determined values in literature. For the CoTEx cryostat the exhaust consists mainly of the bellow ($l = 354\,\mathrm{mm}$, $d = 66\,\mathrm{mm}$) and a T-piece followed by safety valves which introduce another sharp angle and a decrease of the cross section (cf. figure B.1):

$$\zeta = \zeta_{\text{exhaust entry}} + \zeta_{\text{T-piece}} + \zeta_{\text{valve}} + \zeta_{\text{exhaust exit}}.$$

Using the literature values [BE08]

$$\begin{aligned}
\zeta_{\text{exhaust entry}} &= 0.4, \\
\zeta_{\text{T-piece}} &= 1.3, \\
\zeta_{\text{valves}} &= 1.65, \\
\zeta_{\text{exhaust exit}} &= \frac{(2n+1)^3 \cdot (n+1)^3}{4n^4(2n+3)(n+3)} \text{ with } n = \frac{1}{\sqrt{\lambda}}
\end{aligned}$$

and $\lambda = 0.11$ according to the specifications of the bellow used for the exhaust, one can estimate $\mu \approx 0.46$.

Mass flow The mass flow is finally given by:

$$\begin{aligned}\dot{m} &= \mu \cdot A_{\mathrm{o}} \cdot \psi_{\max} \sqrt{2 p_t \rho_t} \\ &= 1.21\,\mathrm{kg/s} \\ &\equiv 229\,\mathrm{l/s} \text{ gas at } 10\mathrm{K}.\end{aligned}$$

So far, only the idealistic isentropic case has been considered which is adiabatic-reversible and assumes no heat exchange of the medium with its surrounding as well as a constant entropy. The more realistic polytropic calculation takes into account the change of entropy and the heating of the gas due to friction. Instead of the adiabatic exponent κ, the polytropic coefficient $n = 1.1$ is used, calculated from

$$\frac{n-1}{n} = \frac{\ln[1-\eta_{\mathrm{exp}} \cdot (1-\frac{T_{\mathrm{o}}}{T_{\mathrm{t}}})]}{\ln[(\frac{T_{\mathrm{o}}}{T_{\mathrm{t}}})^{\frac{\kappa}{\kappa-1}}]}.$$

The temperature at the outlet[40] T_0 can be calculated from:

$$T_{\mathrm{o}} = T_{\mathrm{t}} \cdot \tfrac{2}{n+1} = 9,3\,\mathrm{K}.$$

and $\eta_{\mathrm{exp}} = \mu^2$ for long pipes.
In the polytropic case the critical pressure ratio is given by:

$$\left(\frac{\mathrm{p_o}}{\mathrm{p_t}}\right)_{\mathrm{critical}} = (\tfrac{2}{n+1})^{\frac{n}{n-1}} = 0.58.$$

With the outflow function

$$\psi_{\mathrm{max,p}} = (\tfrac{2}{n+1})^{\frac{1}{n-1}} \sqrt{\tfrac{\kappa}{\kappa-1} \cdot \tfrac{n-1}{n+1}}$$

the mass flow follows:

$$\begin{aligned}\dot{m}_{\max} &= \mu \cdot A_{\mathrm{a}} \cdot \psi_{\mathrm{p,max}} \sqrt{2 p_t \rho_t} \\ &= 0.58\,\mathrm{kg/s} \\ &\equiv 110.7\,\mathrm{l/s} \text{ gas at } 10\ \mathrm{K} \\ &\equiv 6.9\,\mathrm{l/s} \text{ liquid helium}.\end{aligned}$$

Expected critical mass flow This maximum mass flow must not be exceeded by any incident evaporating large amounts of helium. A classical worst-case scenario is the breakdown of the insulation vacuum. This results in a heat input to the liquid helium of $0.6\mathrm{w/_{cm^2}}$ ([LZ78], [XLW10]). If the CoTEx helium vessel is completely filled, the surface area of the liquid helium volume is $27739\,\mathrm{cm}^2$. Using the evaporation enthalpy of $20.41\,\mathrm{kJ/kg}$ the total heat input of $1664\,\mathrm{W}$ gives a boil-off rate of

$$\begin{aligned}\dot{m}_{\mathrm{vac.loss}} &\equiv 188\,\mathrm{l/s} \text{ gas at } 10\ \mathrm{K} \\ &\equiv 7.5\,\mathrm{l/s} \text{ liquid He}.\end{aligned}$$

This is about a factor 1.7 more than the capacity of a single exhaust line. However, in the setup there is a second exhaust of the same dimensions connected over a long pipe ($> 6\,\mathrm{m}$) to the

[40] In addition to the frictional heating, the gas cools when expanding from the pressure tank to the outside. Thus, the exit temperature is smaller than the assumed gas temperature of 10K in the tank.

receiver balloon of the liquefier.
The boil-off rate in case of a quench is very hard to estimate. In the CoTEx setup the only way to estimate this value is from the drop of the helium level over the time. However, the level is not logged constantly to minimize heat input into the cryostat when powering the sensor. Moreover, the sensor does not reach to the bottom of the tank, thus an amount of 60 l of liquid helium is not monitored. Only roughly it can be estimated that a quench (at a current $I = 172\,\mathrm{A}$) evaporated at least 33 l within 66 s giving a boil-off rate of only

$$\begin{aligned} \dot{m}^{\mathrm{min}}_{\mathrm{quench}} &= 0.5\mathrm{l/s\ liquid\ He} \\ &\equiv 12.5\,\mathrm{l/s\ gas\ at\ 10\ K.} \end{aligned}$$

These rough estimations suggest that the exhaust lines are dimensioned sufficiently large. Additionally, more exhaust lines than the ones considered here exist in the CotEx setup (cf. section 4.2 and 4.2.1).

C. Calculation of the scan positions

To measure the magnetic field map in the CoTEx cryostat, one has to calculate the positions the XYZ-stage has to move to, so that the Hall probes are positioned correctly at the desired grid points. For the following explanations see also figure C.1. The measuring positions are

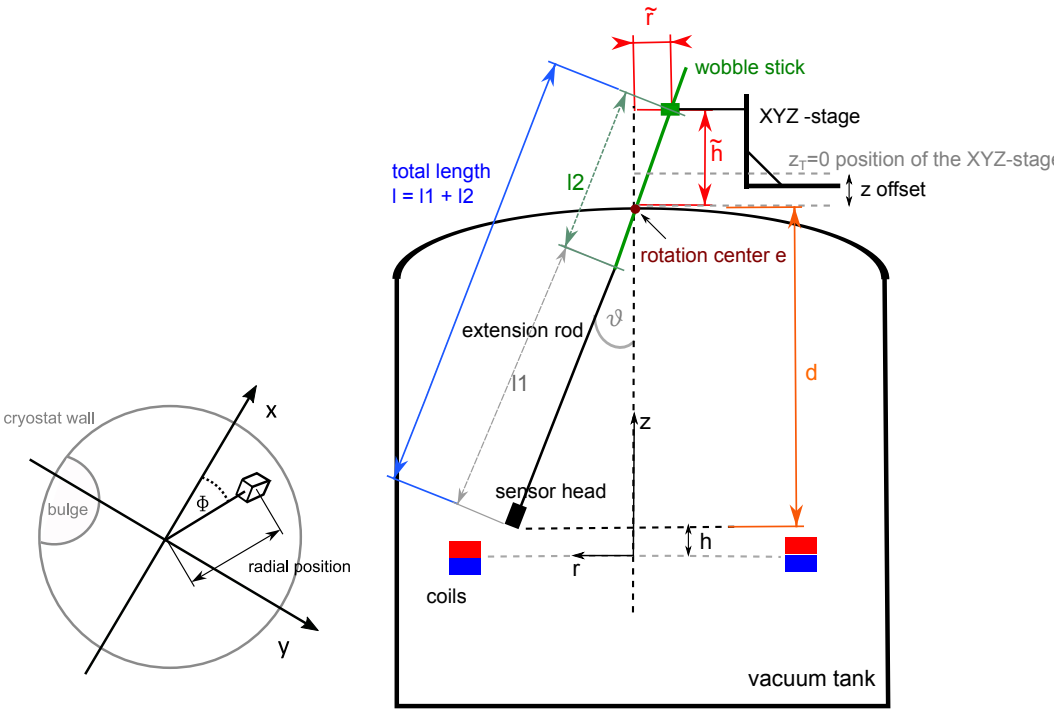

Figure C.1.: Sketch of the geometrical parameters important for the scan path calculations. Left: top view, right: side view.

defined by the azimuth ϕ, the radial distance r from the center of rotation and the height h. The plane defining $h = 0$ coincides with the assumed coil middle plane. This dictates also the length of the extension rod as well as the wobble stick rod and the central z-position of the linear XYZ-stage. The middle of the possible z-range of the stage has been chosen as starting point to have a maximum possible travel in both up- and downward direction for the scans. For the same reason the translation stage is installed at the top of the tank such that the central position (in which the wobble stick is not tilted, $\vartheta = 0$) is approximately in the middle of the ranges of the translation stage in x- and y-directions, respectively.
In the calculations, the fact that the distance of the measuring position to the rotation center is not a fixed length has to be accounted for. E.g. going radially outwards at a fixed height to larger radii, one has to compensate for the larger distance from the measuring position to the rotation center by moving with the XYZ-stage and thus with the wobble stick rod further down.

The parameter that stays fixed, is the total distance l from the sensor head at the end of the extension rod to the point where the XYZ-stage is connected to the wobble stick: $l = l_1 + l_2$. First, the tilt angle ϑ is calculated from the radial position r and the z-distance d from the measuring point to the rotation center of the wobble stick:

$$\vartheta_{\text{measPos}} = \arctan(r/d).$$

The distance d is given by the height h and the distance of the reference plane to the rotation center e, which is a fixed constant:

$$d = e - h.$$

With $\vartheta_{\text{measPos}}$, the corresponding radial position $\widetilde{r}$ and the height $\widetilde{h}$ of this point on the other side of the rotation center at the top of the tank is derived:

$$\widetilde{h} = \cos(\vartheta_{\text{measPos}}) \cdot l - e,$$
$$\widetilde{r} = \tan(\vartheta_{\text{measPos}}) \cdot \widetilde{h}.$$

This gives the $\widetilde{x}$-, $\widetilde{y}$- and $\widetilde{z}$-positions on top of the tank with respect to the central position, the rotation center. With the help of the x- and y-coordinates of the translation stage when placed in the central position (x_{c},y_{c}), these values are finally translated into absolute x_{T}-, y_{T}- and z_{T}-coordinates of the translation stage. Here, it has to be accounted for the fact that the absolute $z_{\text{T}} = 0$ position of the XYZ-stage has an additional offset z_{offset} in height to the rotation center. The final result is:

$$x_{\text{T}} = cos(\phi) \cdot \widetilde{r} + x_{\text{c}},$$
$$y_{\text{T}} = sin(\phi) \cdot \widetilde{r} + y_{\text{c}},$$
$$z_{\text{T}} = \widetilde{h} - z_{\text{offset}}.$$

Sensor offsets The algorithm, as described above, takes the central point at the bottom side of the sensor head as reference. However, due to their physical dimensions, the hall sensors themselves are obviously not mounted all in this single spot. Thus, there is an offset in x- , y - and z -direction for every sensor with respect to this reference point. However, for the correct calculation of the magnetic field the components have to be measured at exactly the same position. Therefore, the algorithm allows to move every sensor individually one after the other to the same absolute position. The coordinates the XYZ-stage has to move to, are calculated as follows: Once the coordinates of the central reference position have been determined, the tilt of the sensor head in this position can be determined. To calculate the real sensor positions, the reference frame is rotated by this tilt angles, and the offsets of the individual sensors are applied as translations in the tilted frame. Rotating back yields the coordinates to position every sensor at the same absolute measuring point. The same rotation transformation is used to calculate the magnetic field components in the laboratory frame from the ones measured in the rotated reference frame of the sensor head. For more information on the rotation transformation, see section 5.4.

Uncertainties In the formulas to calculate the positions several geometrical constants of the setup occur which have to be measured. Any uncertainty of these values will effect the real sensor positions which then differ from the supposed ones. These constants are listed in table C.1 together with their errors.

Item	**value (mm)**	**uncertainty (mm)**
length l_1 (extension rod + sensor head)	1000.5	0.7
length of the wobble stick l_2	394.5	0.2
offset of z=0 position of the XYZ-stage	66	1
offsets of sensor positions w.r.t. reference point	$2-5$	0.1

Table C.1.: Geometrical constants and uncertainties of the setup.

D. Hall sensor specification

Exemplary, in figure D.1 the specifications of one of the cryogenic hall probes is given, especially the measuring error depending on the strength of the magnetic field. Overall, it is well below 1% decreasing at higher magnetic fields to less than 0.5%.

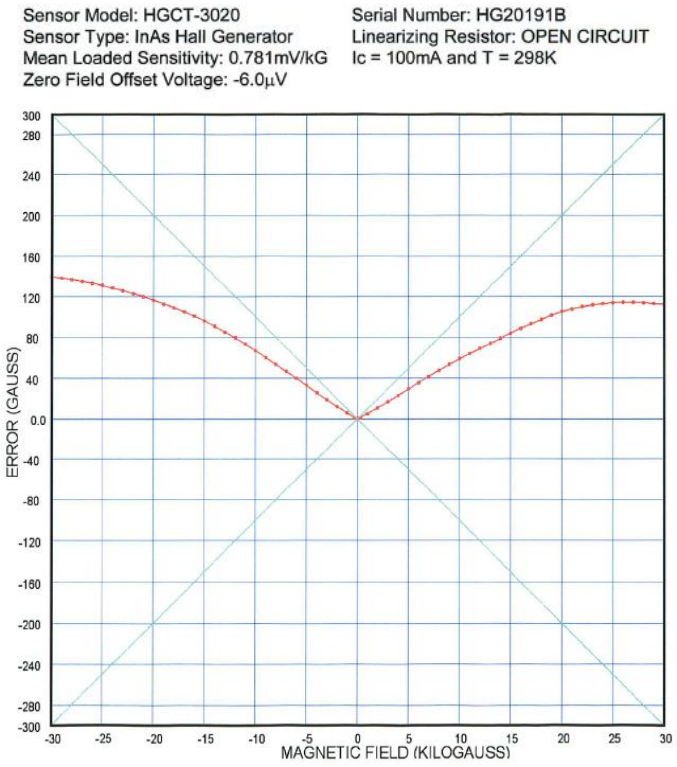

Figure D.1.: Hall sensor specifications.

E. Prototype magnet from Babcock Noell

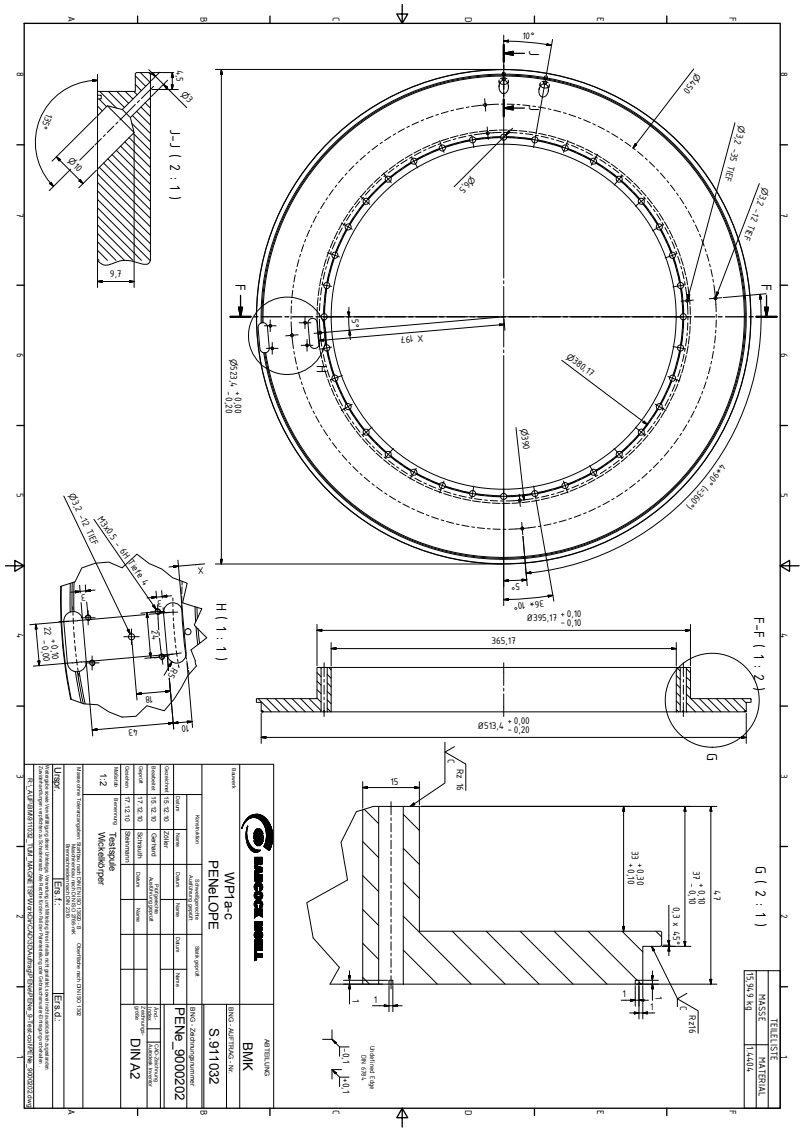

Figure E.1.: Technical drawing of the bottom-coil prototype. [Ste11a]

F. Critical current density of NbTi

The critical current density J_c of NbTi can be parametrized as a function of temperature T and magnetic flux density B as described by the fit formula from [Bot99]. In contrast to more accurate linear approximations this parametrization holds true over a wide range in temperature and flux density. With the critical current density of NbTi at 4.2 K and 5 T, $J_{ref} = 2122\,\mathrm{A/mm^2}$, the maximum upper critical field (at T=0) $B_{c0} = 14.5\,\mathrm{T}$, and the maximum critical temperature (at B=0) $T_{c0} = 9.2\,\mathrm{K}$, the current density is

$$\frac{J_c(B,T)}{J_{ref}} = \frac{C_0}{B}\left(\frac{B}{B_0}\right)^{\alpha}\left(1-\frac{B}{B_0}\right)^{\beta}\left[1-\left(\frac{T}{T_{c0}}\right)^{1.7}\right]^{\gamma},$$

whereas

$$B_0 = B_{c0}\left[1-\left(\frac{T}{T_{c0}}\right)^{1.7}\right].$$

The fit parameters for the NbTi-copper wire are $C_0 = 28\,\mathrm{T}$, $\alpha = 0.6$, $\beta = 1$ and $\gamma = 2$; these values are obtained from the wire manufacturer Supercon. [Ste11b] The effective cross section w_s of the superconductor used in the PENeLOPE magnet calculates from $w_s = 2/3(d/2)^2 \cdot \pi \cdot \mathrm{mm^2}$, using the wire diameter $d = 0.9\,\mathrm{mm}$ and the factor 2/3 for the copper to NbTi ratio. The critical current I_c results via $I_c(B,T) = J_c(B,T) \cdot J_{ref} \cdot w_s$.

List of Figures

List of Tables

Bibliography

[A+00] Arzumanov, S. et al.: Neutron lifetime measured by monitored storing of ultra-cold neutrons. In: *Nucl. Inst. and Meth. A* 440 (2000), Nr. 3, S. 511 – 516

[A+12] Arzumanov, S. et al.: Analysis and correction of the measurement of the neutron lifetime. In: *JETP Letters* 95 (2012), S. 224–228

[Abe08] Abele, H.: The neutron. Its properties and basic interactions. In: *Prog. Part. Nucl. Phys.* 60 (2008), Nr. 1, S. 1 – 81

[B+86] Babenkov, M.I. et al.: Chevron of Microchannel Plates as Position-sensitive Detector for β-Spectrometers. In: *Nucl. Inst. and Meth. A* 252 (1986), S. 83–86

[B+12] Beringer, J. et al.: Review of Particle Physics. In: *J. Phys. G: Nucl. Part. Phys* D86 (2012)

[BE08] Bohl, W. ; Elmendorf, W.: *Technische Strömungslehre*. 14. Vogel Fachbuch, 2008

[Bot99] Bottura, L.: A Practical Fit for the Critical Surface of NbTi. In: *LHC Project Report 358 pesented at 16th International Conference on Magnetic Technology*, 1999

[BP05] Barabanov, A. L. ; Protasov, K. V.: Comment on the article "UCN anomalous losses and the UCN capture cross section on material defects" by A. Serebrov et al. In: *Physics Letters A* 346 (2005), S. 378–380

[BS11] Boffo, C. ; Steinmann, J.: Final Report PENelOPE WP1a / Babcock Noell. 2011. – interner technischer Bericht

[DS11] Dubbers, D. ; Schmidt, M. G.: *The neutron and its role in cosmology and particle physics*. 2011. – arXiv:1105.3694v1 [hep-ph]

[F+87] Fraser, G.W. et al.: Dark Noise In Microchannel Plate X-ray detectors. In: *Nucl. Inst. and Meth. A* 254 (1987), S. 447

[F+95] Funsten, H.O. et al.: Effect of local electric fields on microchannel plate detection of incident 20 keV protons. In: *Rev. Sci. Instrum.* 67 (1995), S. 145

[Fra02] Fraser, G.W.: The ion detection efficiency of microchannel plates (MCPs). In: *International Journal of Mass Spectrometry* 215 (2002), S. 13–30

[G+84] Gao, R. S. et al.: Absolute and angular efficiencies of a microchannel-plate position-sensitive detector. In: *Rev. Sci. Instrum.* 55 (1984), S. 11

[Gol91] Golub, R.: *Ultra-cold Neutrons*. Adam Hilger, 1991

[GP75] Golub, R. ; Pendlebury, J.M.: Super-thermal sources of ultra-cold neutrons. In: *Physics Letters A* 53(2) (1975), S. 133–135

[Gro04] Grover, F.W.: *Inductance Calculations*. Dover Phoenix Editions, 2004

[H+85] Hellsing, M. et al.: Performance of a microchannel plate ion detector in the energy range 3-25 keV. In: *J. Phys. E: Sci. Instrum.* 18 (1985), S. 920–925

[H+06] Hoedl, S. A. et al.: An electron transparent proton detector for neutron decay studies. In: *Journal of Applied Physics* 99 (2006), S. 084904

[Ham94] Hamamatsu. *Technical Information: MCP Assembly.* 1994

[Ham09] Hamamatsu. *MCP and MCP assembly product cataloge.* 2009

[Her87] Herrmann, K.H.: Measurement of the detection quantum efficiency of microchannel plates for medium energy electrons. In: *J. Phys. E: Sci. Instrum.* 20 (1987)

[HT05] Hardy, J. C. ; Towner, I. S.: New limit on fundamental weak-interaction parameters from superallowed beta decay. In: *Phys. Rev. Lett.* 94 (2005), S. 092502

[HT09] Hardy, J. C. ; Towner, I. S.: Superallowed 0+ to 0+ nuclear beta decays: A new survey with precision tests of the conserved vector current hypothesis and the standard model. In: *Phys. Rev. C* 79 (2009), S. 055502

[I+09] Iocco, F. et al.: *Primordial Nucleosynthesis: from precision cosmology to fundamental physics.* 2009. – arXiv:0809.0631v2 [astro-ph]

[IST10] I. S. Towner, J.C. H.: The evaluation of Vud and its impact on the unitarity of the Cabibbo-Kobayashi-Maskawa quark-mixing matrix. In: *Rep. Progr. Phys* 73 (2010), Nr. 4

[JL97] J.E. Lees, J.F. P.: A large area MCP detector for X-ray imaging. In: *Nucl. Inst. and Methods A* 384 (1997), S. 410

[JZ85] J.F. Ziegler, U. L.: *SRIM, The Stopping and Range of Ions in Solids.* Pergamon Press, 1985

[L+10a] Larson, D. et al.: *Seven-Year Wilkinson Microwave Anisotropy Probe (WMAP1) Observations: Power Spectra and WMAP-Derived Parameters.* 2010. – arXiv:1001.4635v2 [astro-ph.CO]

[L+10b] Liu, J. et al.: Determination of the Axial-Vector Weak Coupling Constant with Ultracold Neutrons. In: *Phys. Rev. Lett.* 105 (2010), S. 181803

[Ltd11] Ltd., Photek. *Technical Information.* http://www.photek.com/. 2011

[LZ78] Lehmann, W. ; Zahn, G.: Safety aspects for LHe cryostats and LHe transport containers. In: *Adv. Cryogenic Eng.* 23 (1978), S. 569–79

[M+88] Morenzoni, E. et al.: Microchannel plates in high magnetic fields. In: *Nucl. Inst. and Meth. A* 263 (1988), S. 397–400

[M+00] Marquardt, E.D. et al.: Cryogenic Material Properties Database. In: *11th International Cryocooler Conference*, 2000

[MBC05] M.J. Berger, M.A. Z. ; Chang, J. *PSTAR: Stopping-Power and Range Tables for Protons.* NIST Standard Reference Database 124. 2005

[MH+07] Müller, A.R. ; Hartmann, F.J. et al.: PAFF, a low-energy, low-flux proton accelerator for detector tests. In: *Nucl. Inst. and Meth. A* 582 (2007), S. 395–400

[Mil08] Milward, S.: Performance review: NSV Test Coils / Scienific Magnetics. 2008. – interner technischer Bericht

[Mil09] Milward, S. *private communication.* 2009

[Mül08] Müller, A.R.: *Characterization of solid deuterium as a source material for ultracold neutrons (UCN) and development of a detector concept for the detection of protons from the neutron decay*, TU München, Dissertation, 2008

[MP+09] Materne, S. ; Picker, R. et al.: PENeLOPE - on the way towards a new neutron lifetime experiment with magnetic storage of ultra-cold neutrons and proton extraction. In: *Nucl. Inst. and Meth. A* 611 (2009), S. 176 – 180

[N+05] Nico, J.S. et al.: Measurement of the neutron lifetime by counting trapped protons in a cold neutron beam. In: *Phys. Rev. C* 71 (2005), May, S. 055502

[N+10] Nakamura, K. et al.: Review of Particle Physics. In: *J. Phys. G: Nucl. Part. Phys* 37 (2010), S. 075021

[NB99] Narayan ; Bhattacharya: Degradation and training in superconducting magnet: revisited. In: *Physica A: Statistical Mechanics and its Applications* 270 (1999), Nr. 1-2, S. 226 – 236

[Nie11] Nielsen, C. *private communication.* 2011

[O+97] Oberheide, J. et al.: New results on the absolute ion detection efficiencies of a microchannel plate. In: *Meas. Sci. Technol.* 8 (1997), S. 351–354

[P+87] Pearson, J.F. et al.: Variation of microchannel plate resistance. In: *Nucl. Instr. and Meth. A* 258 (1987), S. 270–274

[Pau09] Paul, S.: The puzzle of neutron lifetime. In: *Nucl. Inst. and Meth. A* 611 (2009), Nr. 2-3, S. 157 – 166

[Pic08] Picker, R.: *PENeLOPE and AbEx - On the Way Towards a New Precise Neutron Lifetime Measurement*, TU München, Dissertation, 2008

[Pre07] Press, W.H.: *Numerical Recipes.* third. Cambridge University Press, 2007

[PS00] Peko, B.L. ; Stephen, T.M.: Absolute detection effciencies of low energy H, H^-, H^+, H_2^+ and H_3^+ incident on a multichannel plate detector. In: *Nucl. Inst. and Meth. B* 171 (2000), S. 597–604

[R+07] Rosén, S. et al.: Operating a triple stack microchannel plate-phosphor assembly for single particle counting in the 12-300 K temperature range. In: *Rev. of Sc. Instr.* 78 (2007), S. 113301

[Res80] van Resandt, R.W.W.: Absolute quantum efficiencies of micro-channelplates for 8-28 keV electrons. In: *J. Phys. E: Sci. Instrum.* 13 (1980), S. 1162

[RF00] Roth, P. ; Fraser, G.W.: Microchannel plate resistance at cryogenic temperatures. In: *Nucl. Instr. and Meth. A* 439 (2000), S. 134–137

[RGM05] Rajput-Ghoshal, R. ; Milward, S.: Neutron Storage Vessel Feasibility Study / Space Cryomagnetics. 2005. – interner technischer Bericht

[S+85] Siegmund, O. et al.: Investigation of Large Format Microchannel Plate Z Configurations. In: *IEEE Trans. on Nucl. Sc.* NS-32 (1985), S. 443

[S+92] Schecker et al.: The performance of a microchannel plate at cryogenic temperatures and in high magnetic fields, and the detection efficiency for low energy positive hydrogen ions. In: *Nucl. Inst. and Meth. A* 320 (1992), S. 556–561

[S+01] Schwartze, P. et al.: A simple and fast transimpedance amplifier for microchannel plate detectors. In: *Rev. of Sc. Instr.* 72 (2001), Nr. 7, S. 3125

[S+04] Serebrov, A. et al.: UCN anomalous losses and the UCN capture cross section on material defects. In: *Phys. Lett. A* 335 (2004), S. 327–336

[S+05] Serebrov, A. et al.: Measurement of the neutron lifetime using a gravitational trap and a low-temperature Fomblin coating. In: *Phys. Lett. B* 605 (2005), Nr. 1-2, S. 72 – 78

[Sch74] Schagen, P.: . Bd. 1. Academic Press, 1974

[Sch11a] Schäfer, T.: Ein Gaszähler zur Protonen/Elektronen-Detektion für das Neutronen-Lebensdauerexperiment PENeLOPE. In: *Frühjahrstagung der Deutschen Physikalisch Gesellschaft, Fachverband Physik der Hadronen und Kerne, HK 7.7*, 2011

[Sch11b] Schreyer, W.: *Monte Carlo-simulations for the neutron lifetime experiment PENeLOPE*, TU München, Diplomarbeit, 2011

[Sch12] Schreyer, W. *private communication.* 2012

[Sci08] Scientific Magnetics: *NSV Test Coils User Manual.* 2008

[Sea92] Sears, Varley F.: Neutron scattering lengths and cross sections. In: *Neutron News* 3 (1992), Nr. 3, S. 26–37

[Sen11] Senft, A.: *CoTex 2.0 - A new Coil Test Experiment*, TU München, Diplomarbeit, 2011

[Sou71] Soul, P.B.: Operational Properties of Channel-Plate Electron Multipliers. In: *Nucl. Inst. and Meth.* 97 (1971), S. 555–565

[Ste57] Sternglass, E.J.: Theory of Secondary Electron Emission by High-Speed Ions. In: *Phys. Rev.* 108 (1957)

[Ste07] Steigmann, Gary: Primordial Nucleosynthesis in the Precision Cosmology Era. In: *Annu. Rev. Nucl. Part. Sci.* 57 (2007), S. 463–91

[Ste11a] Steinmann, J.: *PENeLOPE WP 1b: Testcoil - System description and handling instructions.* Babcock Noell Group, 2011

[Ste11b] Steinmann, J. *private communication.* 2011

[Tie09] Tietze, C.: *Entwicklung eines Detektors zum Nachweis der Protonen aus dem Betazerfall des Neutrons*, TU München, Diplomarbeit, 2009

[Tie12] Tietze, C.: *phd thesis in progress*, TU München, Dissertation, 2012

[Ve92] DER TECHNISCHEN ÜBERWACHUNGS VEREINE E.V., Verband (Hrsg.): *AD Merckblatt A1: Sicherheitseinrichtungen gegen Drucküberschreitung - Berstsicherungen.* Beuth Verlag, 1992

[W+77] WIZA, J.L. et al.: Improved microchannel plate performance with a resistive anode encoder. In: *Rev. Sci. Instr.* 48 (1977), S. 1217

[WG94] WURZ, Peter ; GUBLER, Lukas: Impedance-matching anode for fast timing signals. In: *Rev. Sci. Instrum.* 65 (1994), S. 871

[Wil83] WILSON, M. N.: *Superconducting Magnets.* Oxford Science Publications, 1983

[Wiz79] WIZA, J. L.: Microchannel plate detectors. In: *Nucl. Inst. and Meth. A* 162 (1979), Nr. 1 - 3, S. 587 – 601

[XLW10] XIE, G.F. ; LI, X.D. ; WANG, R.S.: Study on the heat transfer of high-vacuum-multilayer-insulation tank after sudden, catastrophic loss of insulating vacuum. In: *Cryogenics* 50 (2010), Nr. 10, S. 682 – 687

[Z+85] ZIEGLER, J.F. et al.: *The Stopping and Ranges of Ions in Solids, Vol. 1.* Pergamon, 1985

Acknowledgement

Many people have contributed to the realization of this thesis and I am very grateful to all of them:
First of all I like to thank the excellence cluster 'Origin and Structure of the Universe' and especially Stephan Paul for giving me the opportunity to study in the research group E18, providing not only a fruitful and inspiring atmosphere, but also the infrastructure and financial support needed for the experiments.
I owe an enormous dept to Rüdiger Picker and also Joachim Hartman. They both helped me throughout my time at E18 whenever I needed their advice and finally contributed by proof reading of my thesis.
I am much obliged to the 'UCN hut', namely Rainer Stoepler and Andreas Frei, for sharing their technical experience with me. Special thanks go to Thomas Deuschle and Herbert Ruhland from the UCN workshop: without their frequent, fast and uncomplicated help the experiment CoTEx would not have come to life! In this context, I also must not forget to name the central workshop of the Physik-Department and the Maier-Leibnitz-Laboratorium.
Many thanks of course to all my other colleagues, especially the PENeLOPE members, among them Axel Müller, Bea Franke, Christian Tietze, Andreas Senft and Wolfgang Schreyer, for their support in daily problems and the nice atmosphere at work.
I have to thank also all the student assistants, especially Jan Overbeck and Johannes Weiss, for helping me by taking over part of the time consuming laboratory work.
My appreciation goes to Karin Frank for keeping organisational chaos at E18 in order.
Last but not least, I am deeply grateful to my mom and Harald, for bringing me up and still supporting me selflessly anytime.